Title

X-ray spectroscopy of buried layer foils irradiated with an ultra high intensity short pulse laser

Author

Chen, Sophia Nan

Publication Date

2009

UNIVERSITY OF CALIFORNIA, SAN DIEGO

X-ray Spectroscopy of Buried Layer Foils Irradiated with an Ultra High Intensity Short Pulse Laser

A Dissertation submitted in partial satisfaction of the
Requirements for the degree Doctor of Philosophy

in

Engineering Sciences
(Engineering Physics)

by

Sophia Nan Chen

Committee in charge:

Professor Farhat Beg, Chair
Professor Farrokh Najmabadi
Professor Kevin Quest
Professor Clifford Surko
Professor George Tynan

2009

The dissertation of Sophia Nan Chen is approved, and it is acceptable in quality and form for publication on microfilm:

Chair

University of California, San Diego
2009

This dissertation is dedicated to my Grandfathers and to my Father.

TABLE OF CONTENTS

LIST OF FIGURES

ACKNOWLEDGMENTS

First and foremost I must thank my advisor, Professor Farhat Beg for his support and allowing me the freedom to pursue my own path.

I would like to thank my two technical advisors Gianluca Gregori and Pravesh Patel. Both have encouraged me to freely explore the field of short pulse laser physics with the necessary guidance and extraordinary patience. These two scientists have been truly an inspiration; it has been an honour to participate in their science endeavors.

I would like to thank Hyun-Kung Chung for keeping me on track and setting the mark on humility and integrity in the sciences.

I would like to thank the members on my doctoral committee: Kevin Quest, Farrokh Najmabadi, George Tynan, and Clifford Surko. Thank you for the encouraging words and helpful suggestions; I am most grateful for all the support these ten years at the university.

To Rich Stephens for walks in England and getting us all to think outside the box once in a while. More importantly, thank you for your patience and support.

Thank you to Simon Bott, Mingsheng Wei, Hiroshi Sawada, and John Pasley for the mandatory coffees through the day and uplifting chats that cuts the daily grind. Their advice, enthusiasm, and patience has been a light for us graduate students.

To my fellow grad students and friends Tammy Ma, Teresa Bartal, and Cliff Chen. It'll be nice to watch you all play Musical Offices rather than to be a participant. It has been a pleasure to work with them in the laboratory and at the office.

I would like to thank Fida Khattak, Brian Maddox, Stephanie Hansen, Kramer Akli, Daniel Hey, Scott Wilks, and Andreas Kemp for your encouraging words. And to Sebastian Le Pape - I can always count on a smile form during experiment and after a long day at in the lab.

To the staff at Vulcan Laser Facility and Jupiter Facility, especially Margaret Notley, Jim Bonlie, Dwight Price, and Roger Van Maren; without them, the experiments would not have been possible.

I would like to thank my friends, Stephanie Culler, Seema Patel, and Yvonne Lee for their unwavering support. Special thanks to Ashok Swaminathan for somehow convincing me that doing a doctorate is a good idea. His advice has been indispensable; I can only hope that I will be able to dutifully pass it on.

And lastly, to my Mom and my Brother Michael Chen. Your support have been nothing less than a blessing.

Portions of Chapter 4, is a reprint of the material as it appears in: S. N. Chen, G. Gregori, P. K. Patel, H. K. Chung, R. G. Evans, R. R. Freeman, E. G. Saiz, S. H. Glenzer, S. B. Hansen, F. Y. Khattak, J. A. King, A. J. Mackinnon, M. M. Notley, J. R. Pasley, D. Riley, R. B. Stephens, R. L. Weber, S. C. Wilks and F. N. Beg, "Creation of hot dense matter in short-pulse laser-plasma interaction with tamped titanium foils", Physics of Plasmas **14**, 6 (2007). The dissertation author was the primary investigator and author of this paper.

Portions of Chapter 5, is a reprint of the material that has been submitted for publication: S. N. Chen, P. K. Patel, H. -K. Chung, A. J. Kemp, S. Le Pape, B. R. Maddox, S. C. Wilks, R. B. Stephens, F. N. Beg, "X-ray Spectroscopy of Buried Layer Foils Irradiated at 10^{20} W/cm^2", (Physics of Plasmas 2009, accepted) The dissertation author was the primary investigator and author of this paper.

VITA

Education

2009 Doctor of Philosophy, Mechanical Engineering, Engineering Sciences (Engineering Physics), University of California, San Diego

2007 Candidate in Philosophy, Mechanical Engineering, Engineering Sciences (Engineering Physics), University of California, San Diego

2005 Master in Engineering, Electrical Engineering, University of California, San Diego

2002 Bachelor of Science, Electrical and Computer Engineering, University of California, San Diego

Refereed Publications

S. N. Chen, P. K. Patel, H. -K. Chung, A. J. Kemp, S. Le Pape, B. R. Maddox, S. C. Wilks, R. B. Stephens, F. N. Beg, "X-ray Spectroscopy of Buried Layer Foils Irradiated with Laser Intensity of 10^{20} W/cm^2," (Physics of Plasmas 2009, accepted)

B. R. Maddox, H. -S. Park, B. A. Remington, N. Izumi, **S. Chen**, C. Chen, G. Kimminau, Z. A. Ali, M. J. Haugh, Q. Ma, “The Fuji FLA7000 Image Plate System as a Time-Integrated Quantitative X-ray Detector,” (being prepared for publication 2009)

S. Le Pape, A. Macphee, D. Hey, P. Patel, A. Mackinnon, M. Key, J. Pasley, M. Wei, **S. Chen**, T. Ma, F. Beg, N. Alexander, R. Stephens, D. Offerman, A. Link, L. Van-Woerkom, and R. Freeman, Review of Scientific Instruments **79**, 106104 (2008).

K. U. Akli, S. B. Hansen, A. J. Kemp, R. R. Freeman, F. N. Beg, D. C. Clark, **S. N. Chen**, D. Hey, S. P. Hatchett, K. Highbarger, E. Giraldez, J. S. Green, G. Gregori, K. L. Lancaster, T. Ma, A. J. MacKinnon, P. Norreys, N. Patel, J. Pasley, C. Shearer, R. B. Stephens, C. Stoeckl, M. Storm, W. Theobald, L. D. Van Woerkom, R. Weber and M. H. Key, "Laser heating of solid matter by light-pressure-driven shocks at ultrarelativistic intensities", Physical Review Letters **100**, 4 (2008).

M. Nakatsutsumi, J. R. Davies, R. Kodama, J. S. Green, K. L. Lancaster, K. U. Akli, F. N. Beg, **S. N. Chen**, D. Clark, R. R. Freeman, C. D. Gregory, H. Habara, R. Heathcote, D. S. Hey, K. Highbarger, P. Jaanimagi, M. H. Key, K. Krushelnick, T. Ma, A. MacPhee, A. J. MacKinnon, H. Nakamura, R. B. Stephens, M. Storm, M. Tampo, W. Theobald, L. Van Woerkom, R. L. Weber, M. S. Wei, N. C. Woolsey and P. A.

Norreys, "Space and time resolved measurements of the heating of solids to ten million kelvin by a petawatt laser", New Journal of Physics **10**, 13 (2008).

J. Pasley, M. Wei, E. Shipton, **S. Chen**, T. Ma, F. N. Beg, N. Alexander, R. Stephens, A. G. MacPhee, D. Hey, S. Le Pape, P. Patel, A. Mackinnon, M. Key, D. Offermann, A. Link, E. Chowdhtlry, L. Van Woerkom and R. R. Freeman, "Nail-like targets for laser-plasma interaction experiments", IEEE Transactions on Plasma Science **36** ,1128 (2008).

S. N. Chen, G. Gregori, P. K. Patel, H. K. Chung, R. G. Evans, R. R. Freeman, E. G. Saiz, S. H. Glenzer, S. B. Hansen, F. Y. Khattak, J. A. King, A. J. Mackinnon, M. M. Notley, J. R. Pasley, D. Riley, R. B. Stephens, R. L. Weber, S. C. Wilks and F. N. Beg, "Creation of hot dense matter in short-pulse laser-plasma interaction with tamped titanium foils", Physics of Plasmas **14**, 6 (2007).

J. S. Green, K. L. Lancaster, K. U. Akli, C. D. Gregory, F. N. Beg, **S. N. Chen**, D. Clark, R. R. Freeman, S. Hawkes, C. Hernandez-Gomez, H. Habara, R. Heathcote, D. S. Hey, K. Highbarger, M. H. Key, R. Kodama, K. Krushelnick, I. Musgrave, H. Nakamura, M. Nakatsutsumi, N. Patel, R. Stephens, M. Storm, M. Tampo, W. Theobald, L. Van Woerkom, R. L. Weber, M. S. Wei, N. C. Woolsey and P. A. Norreys, "Surface heating of wire plasmas using laser-irradiated cone geometries", Nature Physics **3**, 853 (2007).

J. Pasley, M. Wei, E. Shipton, **S. Chen**, T. Ma, F. N. Beg, N. Alexander, R. Stephens, A. G. MacPhee, D. Hey, S. Le Pape, P. Patel, A. Mackinnon, M. Key, D. Offermann, A. Link, E. Chowdhury, L. Van-Woerkom and R. R. Freeman, "Experimental observations of transport of picosecond laser generated electrons in a nail-like target", Physics of Plasmas **14**, 4 (2007).

ABSTRACT OF THE DISSERTATION

X-ray Spectroscopy of Buried Layer Foils Irradiated with an Ultra High Intensity Short Pulse Laser

by

Sophia Nan Chen

Doctor of Philosophy in Engineering Sciences (Engineering Physics)

University of California, San Diego 2009

Professor Farhat Beg, Chair

Relativistic short pulse laser matter interactions are of great interest in the area of high energy density physics which includes the fields of astrophysics, inertial confinement fusion (ICF), and fast ignition (FI). Such interactions can result in the creation of hot dense matter at keV temperatures near solid density which is crucial for the studying radiation transport, understanding particle transport processes, and benchmarking of computer models in this plasma regime. The plasma by short pulse lasers, with intensity greater than 10^{19} W/cm^2 and picosecond pulses, exists for only several tens of picoseconds, has a nonuniform temperature and density, and has a non-Maxwellian electron distribution thus making characterization a challenge. This work presents for the first time a systematic study of the temperature gradient inside of micron thick solid targets using K-shell spectroscopic techniques and demonstrates the importance of energetic electrons, temporal evolution of the plasma and opacity in the analysis of high intensity short pulse laser plasmas.

Tamped titanium foils were with a short-pulse laser with intensity greater than 10^{19} W/cm^2. Target parameters such as size, tamper material, and tamper thickness were varied to optimize heating and uniformity of the titanium plasma. Comparison of measured titanium K-shell spectra, from a 250 x 250 x 5 μm^3 titanium foil tamped with aluminum, with a collisional radiative model indicated that the front ~0.2 μm reached a peak temperature of $T_{e,peak}$= 1300 eV at solid density. The remaining bulk material had temperature $T_{e,bulk}$ = 100 eV. This experimental result is consistent with previous observations and the use of a tamper greatly enhances the density uniformity of the plasma. Further reduction of the lateral and longitudinal target dimensions was needed to refine the analysis and prompted a second experiment. Five targets, with dimensions of 100 x 100 x 0.4 μm^3, had a copper foil were buried at different depths (i.e. 0-1.5 μm) and irradiated with a short pulse laser with intensities greater than 10^{20} W/cm^2. The measured K-shell spectra again indicated a temperature gradient in the longitudinal direction inside the target. Analysis using a hydrodynamic code and a collisional radiative atomic code showed that the hot electron population, time dependent plasma conditions, and opacity significantly alters the calculated K-shell line ratios thus producing up to a factor of two error in plasma temperature.

Chapter 1

Introduction

1.1 Introduction

High intensity short pulse lasers have given new life to the field of laser produced plasmas with intensities that traditional lasers could not achieve previously. Worldwide, laser facilities are currently capable of delivering light pulses with peak power of ~10^{15} W and are continuing to build lasers of even higher powers. By irradiating a solid target with a high intensity short pulse laser, it is possible to create electron beams with relativistic energies [1], produce x-rays [2], accelerate protons and ions to MeV energies [3-6], create electric fields in excess of 10^{12} V/m and magnetic fields of Giga-Gauss [7-8], and induce nuclear reactions [9-11]. These developments have spawned a host of promising applications such as proton radiography [12], high resolution x-ray sources [2], and high energy density plasmas studies [13]. In particular the short pulse laser is the pivotal component in Fast

Ignition [14], a variation on Inertial Confinement Fusion [15], which serves as the basis of the study discussed in this thesis.

1.2 Inertial Confinement Fusion

Inertial Confinement Fusion (ICF) is one approach to achieve laboratory scale fusion [15]. Interest has grown considerably since a fusion based power plant promises a clean energy source with zero greenhouse gases and minimal nuclear waste. Nuclear fusion is the process by which two nuclei overcome their mutual Coulomb repulsion and combine to form products that are considerably more energetic than the two original particles.

ICF is based upon thermonuclear fusion which uses the thermal energy of the particles to overcome their Coulomb barriers. In particular, it is the fusion reaction between deuterium and tritium nuclei that is of great interest, because of the large energy release, 17.6 MeV per reaction, and large nuclear fusion cross-section. This reaction is described by,

$$\mathrm{D} + \mathrm{T} \rightarrow \alpha\ [3.5\ \mathrm{MeV}] + \mathrm{n}\ [14.1\ \mathrm{MeV}] \tag{1.1}$$

which produces an alpha particle (${}^{4}He_{2}$) and an energetic neutron. For this thermonuclear reaction to take place, several conditions need to be satisfied. First, the fuel must be heated to at least 5 keV in temperature for ignition and secondly, a burn wave can be sustained only if the self heating by the alpha particles is larger than radiation losses and hydrodynamic cooling. Furthermore, the *Lawson criteria* places minimum requirements for of plasma temperature, density and confinement time to achieve the energy gain from fusion reactions. For D-T fusion, the product of confinement time τ_c, temperature T_e, and density n_e, $n_e T_e \tau_c \geq 10^{21}$ keV s/m^3 must be satisfied [16].

The most explored approach of ICF is *central hot spot ignition (CHS)* [15] with key processes shown in Fig 1.1. Highest fusion reaction rates occurs at a temperature above 10 keV. Therefore, to satisfy the Lawson criteria, this method employs high fuel density and small confinement time. This scheme uses a spherical plastic capsule filled with fuel, mixture of solid (cryogenic) deuterium and tritium with a gas core, is spherically imploded using laser light or thermal x-rays. The ablation of the plastic shell drives the sphere inward while the exhaust outward. The fuel is reduced to 1/30 of its initial diameter and density of the fuel reaches 1000 times the original density in approximately five nanoseconds. Shocks created by the ablation pressure drives converge in the center which increases the gas temperature to the ignition temperature and fusion ignites spontaneously. Alpha particle from the fusion reactions will stop in a 10 keV D-T plasma with an areal density ρR = 0.3 g/cm^2, which gives the required density of the gas core for ignition to sustain self heating. The energy generated in the center can then heat the surrounding fuel thereby generating a self propagating burn wave. For a 30% burn fraction, the fuel must be imploded to have a ρR = 3 g/cm^2.

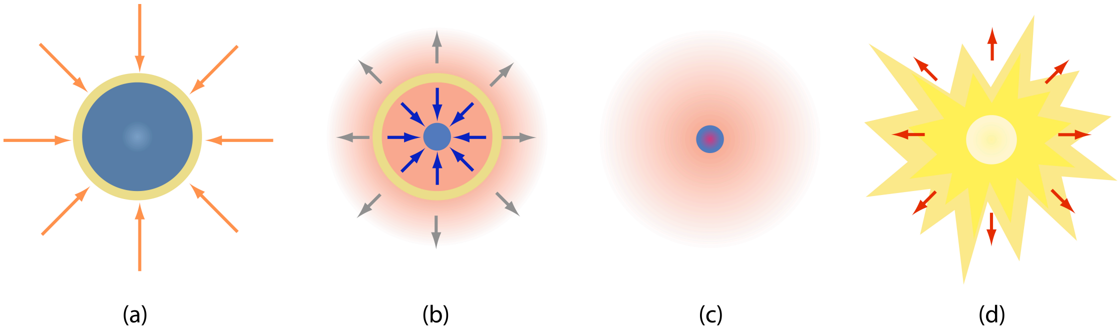

Figure 1.1: **(a)** A spherical plastic capsule filled with solid fuel and gas fill center is uniformly illuminated by high power lasers or x-ray energy. **(b)** The shell is ablated and the energy deposited drives the exhaust outward while driving the fuel inward to bring the fuel to the required densities. In **(c)**, the shocks created during the implosion process converge in the gas core and stagnation occurs when the internal pressure prevents further inward motion of the fuel. **(d)** The gas is heated to fusion conditions by shock heating, fusion reactions are initiated and sustained by reabsorption of the alpha particles that heat the solid fuel.

There are, however, technology limitations and inherent hydrodynamic problems that prevent the realization of CHS ignition. Non-uniform laser illumination during the ablation phase will cause non-symmetrical implosion and complicates the creation of the central hot spot. Growth of perturbations due to Rayleigh - Taylor instabilities occur on both the outer and inner surfaces of an imploding shell. At the outer surface, lower density plasma accelerates the higher density fuel and in the inner surface, the lower density hot plasma core decelerates the incoming cool DT fuel in the stagnation phase. The instabilities in turn mix the layers of the fuel, thus cooling the center and heating the solid fuel, preventing ignition and energy gain.

1.3 Fast Ignition

Alternative schemes, such as separating the fuel assembly and ignition phase, have been discussed since the 1960's [17-18]. The idea proposed was to use an external energy source to ignite the assembled fuel, but only recently has an apparatus that can deliver the required energy become available. *Fast Ignition*, as proposed by Tabak *et. al.* in 1994 [19], uses a short pulse laser, separate from the implosion lasers, to produce high energy electrons that can heat the fuel to ignition conditions. In this scheme, energy of about 3 kJ must be delivered to the fuel in 7.5 ps; therefore, with laser spot size of 20 μm, the intensity of the ignition laser pulse is be at least 10^{20} W/cm^2.

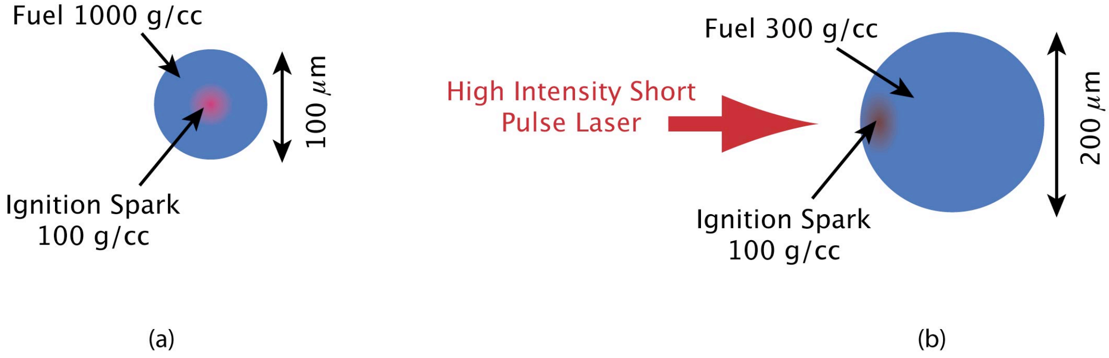

Figure 1.2: Fuel densities of the assembled fuel required for **(a)** CHS ignition and **(b)** Fast Ignition.

In comparison to CHS, as shown in Fig 1.2, drivers implode a fuel capsule to 300 g/cc of uniform density, rather than 1000 g/cc. This reduction in final fuel density subsequently reduces the energy needed for the implosion process. Also, symmetry requirements of the implosion are subsequently relaxed since the hot spot does not need to be formed.

The Fast Ignition concept has evolved significantly over the past 10 years and the variation currently under intense study is what is known as *Cone-Guided Fast Ignition* [19]. This concept uses a cone to protect the path of the short pulse laser to the compressed fuel, as shown in Fig 1.3, from the hundreds of microns of underdense plasma create by the implosion process. Also, the cone brings the location where hot electrons are created much closer to the compressed fuel. It should be noted that experiments and hydrodynamic simulations of the fuel implosion with a cone does not degrade the final fuel assembly [14]. However, studies of the effect of cone material mixing with the fuel are still needed.

Within Cone Guided Fast Ignition, there are two methods of delivering the laser energy to the assembled fuel, one that uses electrons and the other uses protons. Laser energy is transfered to electrons with a 30-40% [5] conversion efficiency through several collisionless absorption mechanisms. These electrons, termed *hot electrons*, have energy that scale proportionally to the $(I\lambda^2)^{0.3\text{-}0.5}$, where I is laser intensity and λ is laser wavelength [1, 20]. Therefore, a laser with an intensity of 10^{20} W/cm^2 can produce greater than 1 MeV hot electrons which have a stopping power that matches the ρR of the compressed fuel [19, 22]. Current ignition laser requirements mandates a 100 kJ laser, assuming 25% conversion into hot electrons, with pulse length of 20 ps [23].

In 1999, an integrated experiment was carried out at the Gekko XII laser facility in Osaka, Japan [24]. Nine long pulse beams, with 1.2 kJ of energy each, were used to implode a CD shell. At the time of stagnation, a short pulse laser with 500 J of energy and a pulse length of 600 fs was fired into the gold cone. The experiment showed the increase of the neutron yielded by a factor of 100 compared with the implosion without the short pulse injection.

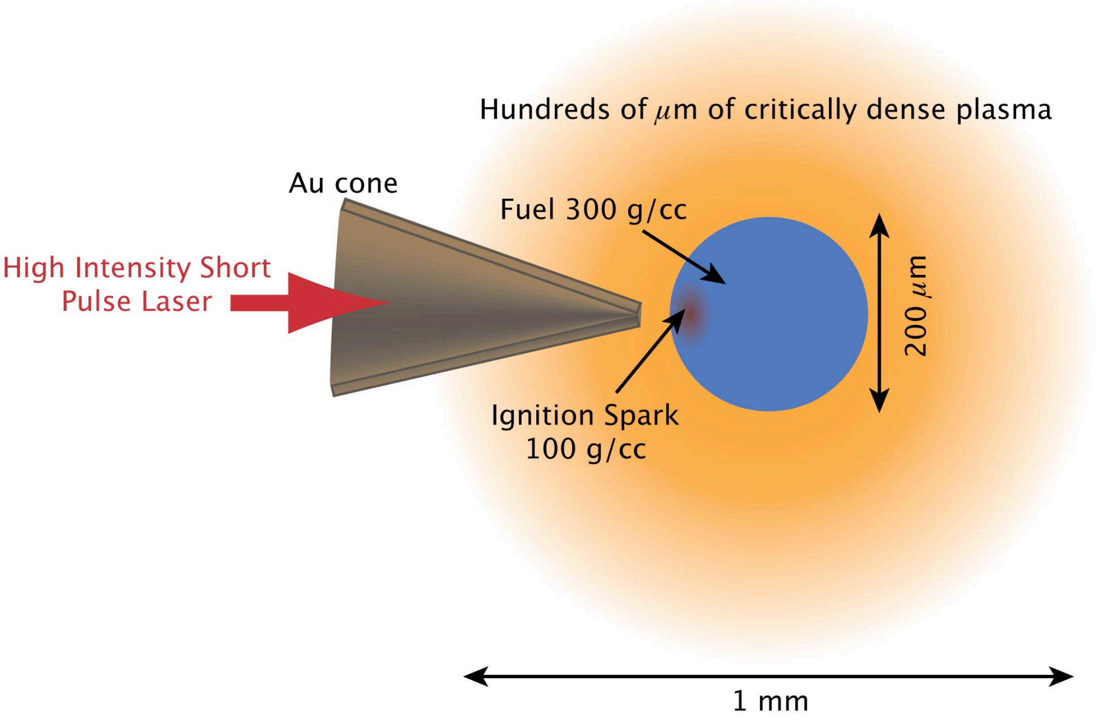

Figure 1.3: Concept diagram of Cone Guided Fast Ignition. A cone sustains a path for the short pulse laser through the critically dense plasma created by the implosion process.

Proton Fast Ignition uses protons rather than electrons to heat the assembled fuel capsule. Protons, originating from a thin layer of hydrocarbon contaminants on the back surface of solid targets, are accelerated off the back of solid targets by an electrostatic sheath created by escaping hot electrons [25]. Hybrid-PIC simulations predict a 50% conversion efficiency from hot electrons to protons [26]. The most energetic protons arriving first at the cold fuel should have energy of 15 MeV to have the adequate stopping power. Lower-energy protons arriving later should have a lower energy of 3 MeV to compliment a rising fuel temperature. All protons must arrive within the 20 ps of inertial confinement time of the assembled fuel and the source to hot spot distance should be less than 1 mm to take full advantage of the useful spread of energies. Additionally, the proton beam can be shaped depending on the geometry of the source. Patel *et. al.* [27] had demonstrated focusing of the proton beam by irradiating a hemisphere on the outside surface with a short pulse laser. This hemisphere can be placed inside the cone to protect the inner focusing wall of the hemisphere from coronal plasma from the fuel assembly process.

1.4 Short pulse laser produced plasmas

Fast Ignition guides much of the current research of short pulse laser plasmas. In particular, the focus has been on absorption physics [28] and characterizing the particle beam [29] that is used to ignite the pre-compressed fuel. Since the hot electrons are created on the front surface of the solid cone tip or metallic hemisphere, for proton fast ignition, understanding the electron transport and interaction with the background material is of great importance. Furthermore, the mechanisms of the heating process in the target, the amount of heated material, and the extent of the temperature gradients of the created plasma have not been thoroughly investigated.

Studying plasma created by high intensity short pulse laser also has interesting implications on other fields. Generation of hot dense matter at keV temperatures near solid density in the laboratory is necessary for the understanding of radiative and transport processes ICF research [13] and enabling laboratory astrophysics experiments [30]. While the success of ICF requires the solution of a complex interaction of laser coupling, equation-of-state, and particle with radiation transport problems, the possibility of experimentally recreating conditions found in ignition experiments in a simplified and open geometry is important. Creation of hot dense plasmas with conditions similar to the interiors of white dwarfs, neutron stars and in other astrophysical environments can be created in the laboratory using a high intensity short pulse laser [31]. Also, the benchmarking of theoretical models, that has been limited to comparisons with numerical simulations, can now be verified in a controlled laboratory environment.

Temperatures between 200–2000 eV in solid targets have been reported in a variety of experiments [32-42]. However, the plasma created from the solid target using a high intensity short pulse laser is highly non-uniform in temperature and density, [42-44] and contains two electron populations, a thermal and an energetic population, which makes characterizing the plasma a challenge. The non-uniformity arises from several factors. The pre-pulse that can ablate the front surface prior to the arrival of the main pulse and the ensuing hydrodynamic motion will deform the target prior to the main pulse. The front of the target can reach temperatures > 2 keV and material several microns deeper stand an order of magnitude cooler [42, 44]. It has been observed from spatially resolved K-alpha images that the interaction region with the laser is finite and smaller than the target lateral size, [44-46] which allows for temperature gradients in the transverse direction. Target thickness also plays a role in the amount of heating experienced by the target due to *refluxing* hot electrons [47]. The hot electrons that leave the target create a sheath field on the front and back surfaces such that subsequent hot electrons leaving the target are turned back by the field. The amount of recirculation of trapped hot electrons continues before thermalizing so long as the sheath field is maintained and the target thickness is less than the mean free path of an electron when hydrodynamically expanding [48].

Plasma temperature and density have been inferred by comparing synthesized spectra from a model to the measured spectra. Measurements of density and temperature of hot dense plasmas have been often inferred from spectroscopic techniques, namely intensity ratios [32-44] and wavelength shifts [49] of Lyman and Balmer series lines. Treatment of hot electrons has not always been included in spectroscopic analysis [42, 50]. When hot electrons are considered, it is assumed to be a small perturbation on the ionization balance and taken to be around 1% of the background electron density [43-44]. There have been efforts to highlight how the hot electron distribution [51-53] can affect K-shell lines and ionization balance in atomic models. However, there has not been anything definitive on how to treat hot electrons in the modeling of experimental spectra. This lack of consistency in modeling stems from several reasons. First, hot electrons are still not well characterized experimentally; the temperature, number density, and lifetime of the hot electrons created in this interaction can only be estimated. Measurements exist for electrons that have escaped from the target (vacuum electrons) [54], but there is not a direct correlation with those trapped within the target itself [55]. The K-alpha yield gives an estimate to the number of hot electrons that have interacted with the target [2], but reveals no information about their energy spectrum. Second, heating mechanisms and hot electron distributions are still under investigation.

Spectral measurements thus far have been limited to temporally and spatially integrated spectra. Therefore, one can only hypothesize as to which point in time during the interaction that specific portions of the spectra are emitted. Time resolved measurements using lasers of similar intensity, but lower energy, show that K-alpha emission can last for tens of picoseconds after the laser pulse has ended [54], meaning that the lifetime of the hot electrons is much longer than the laser pulse length, and the temporal evolution of the temperature and density gradients within the plasma must also be carefully accounted for. Also, there is experimental evidence that plasma hydrodynamics effect can alter K-shell spectra [50] in short pulse plasmas.

Another important parameter in K-shell spectral analysis is the opacity. It is common to use a single-zone population kinetics code assuming that the emitting layer is uniform in temperature and density. For solid density plasma diagnostics, however, it is also important to understand how spatial inhomogeneity affects the modeling of optically thick lines using this type of code. There are two issues concerning optical depth. First, one needs to determine the size of the emitting plasma, a quantity that is normally determined by spectral analysis and not experimentally [42-44]. Second, emission from plasmas with large spatial temperature and density gradient require that the emitting region be treated with many zones and tackling the multiple zone problem using a single-zone population kinetics code creates inconsistency in the treatment of opacity.

With these challenges in mind, there are many possibilities to address these aforementioned issues. The goal of this investigation is to minimize undesired effects and isolate desired plasma conditions by carefully designing experiments and develop modeling techniques. This thesis presents two experiments conducted using buried layer foils and the used of x-ray spectroscopy to diagnose the created plasma. For the first time, a systematic study of the temperature gradient inside of micron thick solid targets, irradiated with a short pulse laser with intensity greater than 10^{19} W/cm^2, was performed. This investigation also includes a study, using a collisional radiative model, on the effects of hot electrons, temporal evolution, and opacity of the hot dense plasma on K-shell spectral calculation. The following chapters will also include background physics, the laser system used, and modeling techniques used in understanding short pulse laser produced plasmas.

1.5 Outline of the Thesis

Chapter 2 gives an overview of the physics of laser plasma interactions at relativistic laser intensities. The classical and relativistic motion of electrons in a laser field and laser plasma interactions are presented. Collisionless absorption mechanisms key to the generation of hot electrons, such as resonance absorption, vacuum heating, and J x B heating, are described. Then radiative transfer and collisional radiative models are described as it pertains to its use in modeling spectroscopic data.

Chapter 3 details the operation of high intensity short pulse lasers and x-ray diagnostics. Specifically, the technical details of the Vulcan Laser at the Rutherford Laboratory Appleton (UK) and the Titan Laser at Lawrence Livermore National Laboratory is presented. Lastly, the design of two x-ray spectrometers and a monochromatic imaging system used in the experiments is discussed.

Chapter 4 describes the first experiment in which a titanium plasma is created with a laser with intensity greater than 10^{19} W/cm^2 to test tamped targets as a variable platform to study temperature and density characteristics. The targets were titanium foils tamped with aluminum or CH plastic to keep the titanium layer at near the original density during the pre-pulse. The targets were kept thin to maximize refluxing for a more uniformly heated target. The spectroscopic data showed that there are longitudinal gradients and spatially resolved images showed that the hot electrons did not interact with the target uniformly. Bulk and peak temperature achieved in the titanium plasma was inferred from the measured titanium K-shell spectra through the atomic code SCRAM. Finally, a potential explanation of lower bulk and peak temperatures of the CH tamped target is presented.

Chapter 5 presents experimental results from a second experiment with improved target platform and modeling. The dimensions of the target were reduced to mitigate gradients, but still limited to time and spatially integrated spectroscopic measurements. Five targets were used where a thin layer of copper was buried inside a target at different locations. Using the collisional radiative code FLYCHK, the observed data was used to study three parameters: the effect of a second energetic electron population, opacity in non-LTE calculations, and temporal evolution of plasma conditions on K-shell spectra.

Chapter 6 summarizes this work and gives a perspective for future work.

1.6 Role of the Author

This section describes the role of the Author in the work presented in this thesis. The data in Chapter 4 was collected on an experiment at the Vulcan TAW designed by the Author, F. N. Beg, and G. Gregori. The Author was involved in the target area set-up, beam line construction, beam timing and diagnostic set-up. The collected data was analyzed by the Author. The h2d simulations presented in Chapter 4 were performed by J. R. Pasley. Spectral synthesis of titanium K-shell spectra was performed by S. B. Hansen. Post processing of the spectra was done by the Author. Section 4.6 was co-written with R. G. Evans. The data in Chapter 5 was collected on an experiment at the Titan Laser at LLNL designed by the author and P. K. Patel based on the results described in Chapter 4. The Author designed the HOPG spectrometer which was built by R. Van Maren. The diagnostic was set-up and data was collected by the Author. The code FLYCHK was integrated with HYADES by H. -K. Chung. Simulations and analysis were performed by the Author.

Chapter 2

Physics of Laser Absorption and Radiative Transfer

Short pulse lasers, with intensities in excess of 10^{18} W/cm^2, interacting with solids are unique in that laser plasma interaction is relativistic. In the interaction of a high intensity short pulse laser with a solid target, the foot of the main pulse or pre-pulses ablates the front surface thus creating a critically dense plasma plume on the front surface of the solid target. Through various collisionless absorption processes in the pre-plasma, the laser energy goes into accelerating electrons to MeV energies. The hot electrons enter into the solid and may deposit some of their energy into the thermal plasma through collisions with ions and other electrons. A small subset of collisions are with inner shell electrons which results in K-alpha photon production. The K-alpha emission induced by hot electrons is of interest since the wavelength of the emission lines are dependent on average ionization state.

The basis of this study hinges on the use of the hot electrons as a probe to determine the characteristics of a short pulse laser produced plasma. First, the motion of electrons in a laser field and the interaction between a laser and a plasma in both a classical and relativistic case is discussed. Then several collisionless laser absorption mechanisms that lead to the production of hot electrons is introduced. This will serve as the foundation in understanding the characteristics of the hot electron population. Then the atomic processes that determine the ionization state and level populations of a plasma will be examined. This will lead into a discussion on the expression for line emission and the radiation transfer equation. Finally, a particular treatment for optically thick lines through the use of an escape factor is presented.

2.1 Laser - electron interactions

Above laser intensities of 10^{16} W/cm^2, various physics phenomena depend on laser irradiance Iλ^2 [56]. This scaling effect, in part, is due to electron quiver momentum, p_o, approaching $m_e c$, where m_e is the electron rest mass and c is the speed of light. The parameter that is commonly used to describe this regime is the normalized vector potential defined as,

$$a_o = \frac{p_o}{m_e c} = \frac{eE_o}{\omega m_e c} = \sqrt{\frac{I\lambda_{\mu m}^2}{1.37 \times 10^{18}}} \tag{2.1}$$

where I is the laser intensity in W/cm^2, E_o is the electric field experienced by the electron, ω is the laser frequency, and $\lambda_{\mu\text{m}}$ is the laser wavelength in microns. The normalized vector potential defines the boundary of the relativistic regime (a_o >1) and classical regime ($a_o < 1$). With laser intensities at 10^{20} W/cm^2, $a_o = 9$, and clearly in the relativistic regime.

In the presence of electromagnetic fields $\boldsymbol{E}$ and $\boldsymbol{B}$, with wavelength ω, electrons will oscillate according to what is known as the *quiver motion* of the electrons. If $v \ll c$, the second term can be neglected from the equation of motion,

$$m_e \frac{d\mathbf{v}}{dt} = -e[\,\mathbf{E} + \frac{\mathbf{v}}{c} \times \mathbf{B}\,] \tag{2.2}$$

and the electron will have quiver velocity,

$$\mathbf{v}_{os} = \frac{e\mathbf{E}}{m_e \omega} \tag{2.3}$$

However, if $v \gg c$ the second term is not neglected and the free electron quivering along the direction of the laser field will not experience a restoring force to return to its original position.

2.1.1 The ponderomotive force

A laser has a spatial profile normal to the direction of propagation thus, not all electrons in the laser field will experience the same field strength. Electrons in high intensity regions are pushed away and the final energy of an electron in a laser field can be described by the laser *ponderomotive force*. Assuming that $\gamma \sim 1$ for the classical case. Starting with the electric field with frequency ω,

$$\boldsymbol{E} = \boldsymbol{E_o}(r_o)\, cos(\omega t), \tag{2.4}$$

where $\boldsymbol{E_o}$ is the amplitude of the electric field, $\boldsymbol{r_o}$ is the initial position of the electron. Considering first order terms in the equation of motion, Eq 2.2 becomes,

$$m_e \frac{d\mathbf{v}_1}{dt} = -e\mathbf{E_o}(\mathbf{r_o})\ cos(\omega t) \tag{2.5}$$

Integrating in time will yield velocity of the electron,

$$\mathbf{v}_1(\mathbf{r_o}) = -\frac{e}{m_e \omega}\mathbf{E_o}(\mathbf{r_o})\ sin(\omega t) \tag{2.6}$$

and integrating again will yield position of the electron,

$$\mathbf{r}_1(\mathbf{r_o}) = \frac{e}{m_e \omega^2}\mathbf{E_o}(\mathbf{r_o})\ cos(\omega t) \tag{2.7}$$

In second order, $\mathbf{E_o}(\mathbf{r_o})$ is expanded around the initial position of the electron to give,

$$\mathbf{E}(\mathbf{r}) = \mathbf{E_o}(\mathbf{r_o}) + (\mathbf{r}_1 \cdot \nabla)\mathbf{E}\ |_{\mathbf{r}=\mathbf{r_o}} + \dots \tag{2.8}$$

Taking the terms that quadratically depend on the electric field and the second order equation of motion, this gives,

$$m_e \frac{d\mathbf{v}_2}{dt} = -e\left[(\mathbf{r}_1 \cdot \nabla)\mathbf{E_o} + \mathbf{v}_1 \times \mathbf{B}_1\right] \tag{2.9}$$

Using Maxwell's equation, $\boldsymbol{B}_1 = 1/\omega[\nabla \times \boldsymbol{E}_o\ sin(\omega t)]$, and averaging over the oscillations of the laser field Eq 2.9 leads to the ponderomotive force,

$$\mathbf{F}_{pond} = m_e \left\langle \frac{d\mathbf{v}_2}{dt} \right\rangle = -\frac{e^2}{4m_e\omega^2}\nabla\mathbf{E_o}^2 \tag{2.10}$$

The ponderomotive force is proportional to both the electromagnetic wave frequency and the spatial gradient of the laser intensity. Since intensity is used commonly to describe a laser field, the ponderomotive force can be directly correlated to the laser intensity by,

$$I = \langle |\mathbf{S}| \rangle = \frac{1}{\mu_o} \langle |\mathbf{E} \times \mathbf{B}| \rangle = \frac{\varepsilon_o c}{2} E_o^2 \tag{2.11}$$

In the relativistic regime, the mass is modified by the relativistic factor $\gamma=(1+(p/m_e c)^2)^{-1/2}$ and the ponderomotive force becomes,

$$\mathbf{F}_{pond} = -\frac{e^2}{4\langle\gamma\rangle m_e \omega^2} \nabla \mathbf{E_o}^2 \tag{2.12}$$

which will be important in the derivation of the energy acquired by electrons through the relativistic ponderomotive potential.

2.1.2 Relativistic electron motion

As velocity of the electron approaches c, the $\mathbf{v} \times \mathbf{B}$ term in the equation of motion becomes important and the electron trajectories turn into a 'figure-8' shape [57]. Our interest lies in the final energy of electrons, so starting with the relativistic form of the equation of motion. For simplicity, the laser electromagnetic wave can be described by the vector potential, $\mathbf{A}(x,t)$, that is parallel to the y-direction and varies in space x and time t and has the form,

$$\mathbf{A} = \hat{y}\ \mathbf{A_o} sin(kx - \omega t) \tag{2.13}$$

In the absence of any electrostatic potential, the electric and magnetic fields can be written as,

$$\mathbf{E} = -\frac{\partial \mathbf{A}}{\partial t} \tag{2.14}$$

$$\mathbf{B} = \nabla \times \mathbf{A} \tag{2.15}$$

and taking the scalar values,

$$E_o = \hat{y}\ \omega A_o \tag{2.16}$$

$$B_o = \hat{z}\ kA_o \tag{2.17}$$

the normalized vector potential of Eq 2.1, the potential becomes

$$a_o = \frac{eE_o}{\omega m_e c} = \frac{eA_o}{m_e c} \tag{2.18}$$

In the relativistic regime, $a_o > 1$, and electric and magnetic fields can be written in terms of a_o so for simplicity,

$$E_o = \frac{a_o}{\lambda} \cdot\ 3.21 \times 10^{12}\ \frac{V}{m} \cdot \mu m \tag{2.19}$$

$$B_o = \frac{a_o}{\lambda} \cdot\ 1.07 \times 10^{4}\ T \cdot \mu m \tag{2.20}$$

For laser intensities of 10^{20} W/cm^2 and wavelength 1.054 μm, the electric field approaches 27.4 V/m · μm and the magnetic fields is approximately 9.1 T/μm. Also Eq 2.11 becomes

$$I = \frac{a_o^2}{\lambda^2} \cdot\ 1.37 \times 10^{18}\ \frac{W}{cm^2} \cdot \mu m^2 \tag{2.21}$$

to give the relation of Eq 2.1. Now, if considering the electrostatic potential and write Maxwell's equations as,

$$\mathbf{E} = -\nabla \Phi - \frac{\partial \mathbf{A}}{\partial t} \tag{2.22}$$

$$\mathbf{B} = \nabla \times \mathbf{A} \tag{2.23}$$

The relativistic equation of motion becomes [55],

$$\frac{\partial}{\partial t}(\mathbf{p}-e\mathbf{A})-\mathbf{v}\times\nabla\times(\mathbf{p}-e\mathbf{A})=\nabla(e\Phi-\gamma m_ec^2) \tag{2.24}$$

The trivial solution is $\mathbf{p}$ = e$\mathbf{A}$ and therefore $e\nabla\Phi = m_ec^2\nabla\gamma$ which depicts that the electrostatic force, $e\nabla\Phi$, balanced by another force $m_ec^2\nabla\gamma$. By definition of the relativistic factor γ,

$$\gamma=\sqrt{1+\left(\frac{p}{m_ec}\right)^2}=\sqrt{1+\left(\frac{e\mathbf{A}}{m_ec}\right)^2}=\sqrt{1+a_o^2} \tag{2.25}$$

then using $\nabla\gamma = (2\gamma)^{-1}\cdot\nabla(p/m_ec)^2$, then,

$$m_ec^2\nabla\gamma=\frac{m_ec^2}{2\gamma}\nabla a_o^2 \tag{2.26}$$

which is the relativistic ponderomotive force in Eq 2.12. Using the relativistic kinetic energy,

$$E_{kin}=m_ec^2(\gamma-1)=m_ec^2(\sqrt{1+a_o^2}-1) \tag{2.27}$$

For an electron, m_ec^2 = 0.511 MeV and re-writing in terms of laser intensity kinetic energy becomes,

$$E_{kin}=0.511\,MeV\left(\sqrt{1+\left(\frac{I\lambda^2}{1.37\times10^{18}\,W/cm^2\cdot\mu m^2}\right)^2}-1\right) \tag{2.28}$$

This gives an analytical estimate of energy of electrons accelerated by a relativistic ponderomotive potential from the laser field.

2.2 Laser - plasma interactions

The laser field, with wave number k and wavelength ω, can be represented by an electromagnetic wave as a function of space and time,

$$\boldsymbol{E} = \boldsymbol{E_o}\, e^{-i(kx - \omega t)} \tag{2.29}$$

$$\boldsymbol{B} = \boldsymbol{B_o}\, e^{-i(kx - \omega t)} \tag{2.30}$$

Using Maxwell's equations and equation of motion,

$$\nabla \times \mathbf{B} = \mu_o(\mathbf{J} + \varepsilon_o \frac{\partial \mathbf{E}}{\partial t}) \tag{2.31}$$

$$\nabla \times \mathbf{E} = -\frac{\partial \mathbf{B}}{\partial t} \tag{2.32}$$

$$m_e \frac{\partial \mathbf{v}}{\partial t} = -e(\mathbf{E} + \mathbf{v} \times \mathbf{B}) \tag{2.33}$$

where ε_o is permitivity, μ_o is permeability, linearization and using $\mathbf{J}=ne\mathbf{v}$, where n is the density of the plasma, gives the dispersion relation,

$$\omega^2 = c^2k^2 + \omega_{pe}^2 \tag{2.34}$$

for an electromagnetic wave propagating in a plasma where c is the speed of light. The plasma frequency ω_{pe},

$$\omega_{pe} = \sqrt{\frac{ne^2}{\varepsilon_o m_e}} \tag{2.35}$$

is a natural oscillation that free electrons in a plasma undergo induced by the stationary positive ion background. For laser frequency $\omega_L > \omega_{pe}$, refractive index $\eta=ck/\omega=(1-\omega_{pe}^2/\omega^2)^{1/2}$ is real and the wave can propagate. At the point where

$\omega_L = \omega_{pe}$, k approaches zero and the wave is reflected. The density of the plasma at this point is called the *critical density*,

$$n_c = \frac{\varepsilon_o m_e \omega_L^2}{e^2} = \frac{1.12\,x\,10^{21}}{\lambda_{\mu m}^2}(cm^{-3}) \tag{2.36}$$

and defines the boundary between underdense ($n<n_c$) and overdense ($n>n_c$). When $\omega < \omega_{pe}$, wave is evanescent and the electromagnetic wave decreases exponentially over a characteristic distance given by the skin depth $\delta = c/\omega_{pe}$.

For a lasers intensities greater then 10^{18} W/cm^2, as shown in Section 2.1.2, electrons in the laser field can be accelerated to relativistic energies. With the relativistic correction factor γ that modifies the electron mass, the dispersion relation, Eq 2.34 becomes,

$$\omega^2 = c^2k^2 + \frac{\omega_{pe}^2}{\gamma} \tag{2.37}$$

The effective critical density will increase by γ, thus the laser will penetrate further into a critically dense plasma.

2.3 Laser energy absorption mechanisms

Laser absorption will occur when the pre-pulse interacts with the solid and when the main pulse arrives at the target with very different absorption mechanisms because of the difference in intensity. The laser pre-pulse, typically nanoseconds in duration, is long enough for a substantial coronal plasma to form and create hydrodynamic motion of the target. The amount of pre-plasma is characterized by the density scale length L defined by $L = (\partial \ln(n)/\partial x)^{-1}$ where n is the electron density. For a freely expanding plasma, the scale length can be approximated by $L = c_s\tau$ where c_s is the speed of sound given by,

$$c_s = \sqrt{k_B \frac{ZT_e + T_i}{M_i}} \tag{2.38}$$

where T_e *and* T_i are the electron and ion temperature respectively, Z is the ionization state, M_i is the mass of ions, k_B is the Boltzman constant, and τ is the plasma formation time (typically taken as laser pulse duration). Absorption of the laser energy in the main pulse will occur in the pre-formed plasma. In the following sections it will be shown that this length scale along with $I\lambda^2$ parameters will dictate the dominant laser energy absorption mechanism.

2.3.1 Inverse Bremsstrahlung

At laser intensities below 10^{15} W/cm^2, the dominant absorption mechanism is collisional absorption by way of *Inverse Bremsstrahlung (IB).* Free electrons are accelerated by photons in the presence of the electric field of an ion. Electrons will then lose the energy through subsequent collisions with ions. The spatial damping rate which has dependence on electron temperature T_e and density n_e, and average ionization Z, can be estimated by [27],

$$\kappa_{ib} \propto \frac{Zn_e^2}{T_e^{3/2}(1 - n_e/n_{cr})^{1/2}} \tag{2.39}$$

This absorption mechanism works well in low temperature, high Z, and high density plasmas. Additionally, Ginzburg [28] showed that with a Maxwellian electron distribution, IB is most efficient in plasmas with long density gradients. However, at high laser intensities, I > 10^{15} W/cm^2 , several effects render collisional absorption ineffective. First, with high intensity lasers, the electron distribution is non-Maxwellian and Langdon [58] has shown that the distribution can be modified by a laser field and decrease absorption efficiency. Second, since collisional damping is dependent on the electron-ion collision frequency [59],

$$\nu_{ei} = \frac{4(2\pi)^{1/2}}{3}\frac{n_e Z e^4}{m^2 \mathrm{v}_{te}^3} ln\, \Lambda \tag{2.39}$$

As temperature rises, collisional damping is reduced. Third, the collision frequency is further modified since the electron quiver velocity $v_{os} = eE_o/m_e\omega$, the velocity that an electron can acquire in the presence of an electromagnetic wave, is comparable to the thermal velocity $v_{th} = (2E_o/m_e)^{1/2}$, this reduces the collision frequency as shown in the following [60].

$$\nu_{eff} \simeq \nu_{ei}\frac{\mathrm{v}_{th}^3}{(\mathrm{v}_{os}^2 + \mathrm{v}_{th}^2)^{3/2}} \tag{2.40}$$

Therefore, for laser intensities greater than 10^{15} W/cm^2, collisionless absorption that can couple laser energy into the plasma will be considered.

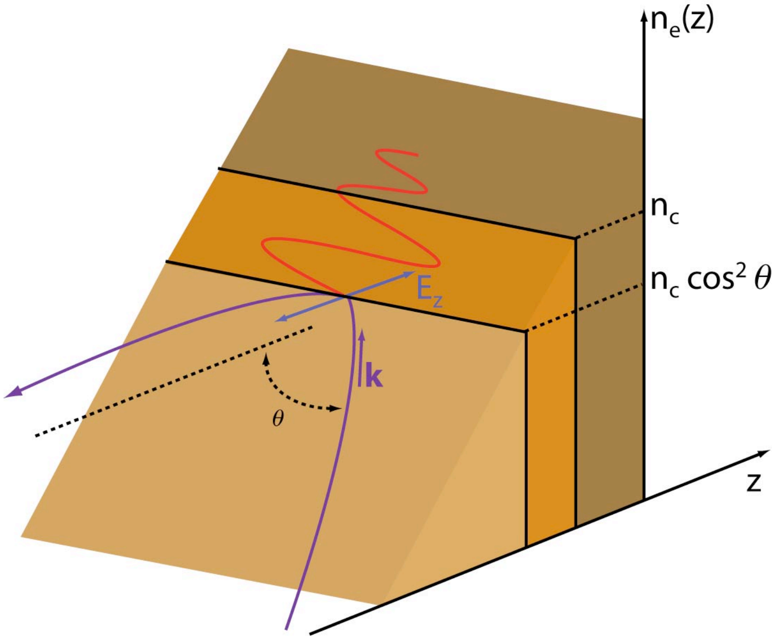

Figure 2.1: A p-polarized wave incident is on plasma with a density gradient with angle θ. The wave is reflected at $n = n_c \cos^2\theta$, but the z-component of the E-field is able to tunnel to n_c and drive a plasma wave into the overdense plasma.

2.3.2 Resonance Absorption

Laser light impinging on a plasma with increasing density will pass through the underdense plasma, but is reflected as it reaches the critical density surface. However, light that is obliquely incident to the critical surface, the point of reflection is at density $n_e(\theta) = n_c \cos^2\theta$ with θ being the angle of incidence as shown in Fig 2.1. Furthermore, for p-polarized light, the E_z component of the electromagnetic wave can tunnel through the reflection point to the critical surface and drives a plasma wave with frequency $\omega_{pe} = \omega_L$. This resonantly excited wave grows over a number of laser periods and is eventually damped either by collisions at low laser intensities or by wave breaking at high intensities inside the overdense plasma.

The effectiveness of the laser driving a resonance wave in the overdense plasma is dependent on plasma length scale, L at the critical surface and laser incidence angle. Fraction of absorption can be approximated by [27],

$$f \approx \frac{\phi^2(\tau)}{2} \tag{2.41}$$

where $\phi \approx 2.3\tau e^{-2\tau^3/3}$ and $\tau = (\omega_o L/c)^{1/3} \sin\theta$. At near normal incidence, i.e. $\theta \rightarrow 0$, the E_z component of the electromagnetic wave is reduced which sets a lower limit on the incidence angle. For a large angle of incidence, f becomes very small, hence reducing fraction absorbed. A large angle of incidence pushes the surface of reflection into lower density and the wave must tunnel a longer distance to reach the critical surface. Peak absorption can be found using this relation, $kL^{1/3} \sin\theta = 0.5^{1/3}$ [62].

Simulations have shown that electrons that receive the energy through the dampening process have temperature T_h and is observed to scale like [63-64],

$$T_h(keV) \sim 10(T_e I_{15} \lambda_{\mu m}^2)^{1/3} \tag{2.42}$$

where T_e is the background plasma electron temperature with units of keV, I_{15} is the laser intensity in units of 10^{15} W/cm^2, and $\lambda_{\mu m}$ is the laser wavelength in μm. Hot electrons, produced via resonance absorption, following such scaling have also been observed in experiments with laser intensities up to 10^{19} W/cm^2 [65-66].

2.3.3 Brunel Heating

As intensity increases, a laser with intensity of 10^{19} W/cm^2 will exert a pressure, $p_L = 2I/c$ where I is laser intensity and c is the speed of light, of approximately 6 Gbar, and will cause plasma gradient to steepen. With a short plasma scale length, when the amplitude is greater than the density scale length, there will be no more resonance and another absorption mechanism becomes dominant. In process known as *Brunel heating* [67], electrons are directly heated by the p-polarized component of the laser field. The abrupt change in the plasma/vacuum interface will expose electrons directly to the laser field. Electrons which are pulled into the vacuum by the laser field will be pushed back into the overdense plasma when the oscillating field changes the direction. There is no restoring field to bring electrons out into the vacuum again since the laser field is limited by the plasma skin depth.

Consider a electromagnetic wave with electric field $E(x,t) = E_L \sin(\omega_o t - k_o x)$ where E_L is the amplitude of the laser electric field. The reflected wave is also present at the point of reflection, therefore the driving electric field will have double the amplitude $E_d = 2E_o \sin\theta$. The absorption efficiency [67],

$$f = \frac{\eta}{2\pi}\left(\frac{v_{os}^3}{v_L^2\, c\, cos\theta}\right) \tag{2.43}$$

is directly related to the amplitude of the laser field and the incident angle. Here, the parameter $v_L = eE_L/m_e\omega$, E_L is the total laser electric field and ω is the laser frequency while E_o is the electric field normal to the surface. Kato *et. al*. [68] found that η can be estimated by the following equation,

$$\eta \approx \frac{1}{1-\omega^2/\omega_{pe}^2} \tag{2.44}$$

For $I\lambda^2 \sim 10^{16}$ Wcm$^{-2}\mu$m^2 and $L/\lambda = 0.4$, absorption as high as 70% has been observed in simulations [69]. However, at higher intensities, absorption saturates at around 10-15%. This leads into another absorption mechanism at even higher laser intensities known as *J × B heating*.

2.3.4 JxB Heating

This absorption mechanism is due to the oscillating component of the ponderomotive force of the laser. Consider the ponderomotive force Eq 2.10 as derived in Section 2.1.1,

$$\mathbf{F}_{pond} = -\frac{e^2}{4m_e\omega^2}\nabla\mathbf{E}^2 \tag{2.45}$$

and let $E = E_o(x)\ sin(w_o t)$ and the expression becomes,

$$\mathbf{F}_{pond} = -\frac{m}{4}\frac{\partial \mathrm{v}_{os}^2(x)}{\partial x}(1 - cos\ 2\omega t) \tag{2.46}$$

The first term on the RHS, is the usual static ponderomotive force. The second, high frequency term leads to heating in an analogous fashion to the component of a p-polarized electric field parallel to the density gradient. Electrons at the critical surface that are influenced by this force, oscillate at twice the laser frequency along the direction of the laser k vector. The electrons that enter the overdense plasma due to this force are not subject to the restoring force and impart energy into the plasma. This absorption mechanism works for any polarization apart from circular, most efficient for normal incidence and becomes significant at relativistic quiver velocities. As shown in Section 2.1.1, electrons subject to the ponderomotive force will be pushed away from the regions of highest laser intensity. However, with laser intensities greater than 10^{18} W/cm^2, relativistic drift motion, described in Section 2.1.2, will cause electrons to be accelerated in the forward direction. This has recently been verified by Ping *et. al.* [70] that laser with intensity of 8 x 10^{19} W/cm^2 have hot electrons directed in the laser forward direction. 2-D PIC simulations confirms such acceleration mechanisms and have shown that absorption efficiency is about 10-20% [20,66] and found that hot electron temperature scales as,

$$T_{hot} \approx \left(\sqrt{1 + \frac{I\lambda_{\mu m}^2}{1.4 \times 10^{18}}} - 1 \right) 511\ keV \tag{2.47}$$

which has similar form to the relativistic ponderomotive potential of Eq 2.28. It should be noted that absorption efficiency decreases with an increase of plasma density as the electromagnetic field can only penetrate a depth of several skin depths [71].

2.3.5 Hot electron temperature

Empirical scaling such as Beg's scaling [73] described by,

$$T_{hot} = 215 \left(\frac{I\lambda_{\mu m}^2}{10^{18}\ W/cm^2} \right)^{1/3} keV \tag{2.48}$$

is also commonly used to predict hot electron temperature. This scaling has been confirmed by Haines *et. al.* [74] by using a relativistic analytical model, namely,

$$T_{hot} = \left(\sqrt{1 + 1.4 * \left(\frac{I\lambda^2_{\mu m}}{1.4 \times 10^{18}} \right)^{1/2}} - 1 \right) 511\ keV \tag{2.49}$$

Knowing the hot electron distribution characteristics is critical in estimating the hot electron fraction present in the plasma. For a laser with energy E_L and a conversion efficiency to hot electrons η, and using a T_{hot} from an appropriate scaling law then,

$$\frac{E_L \eta}{T_{hot}} = N_{hot} \tag{2.50}$$

will give total number of hot electrons N_{hot}. Then fraction of hot electrons f, is given by

$$f = \frac{N_{hot}}{V} \left(\frac{1}{n_e} \right) \tag{2.51}$$

where V, is the volume of the target and n_e is electron density in the plasma. For example, a laser with energy of 150 J and assuming a 30% conversion efficiency, 45 J is transfered to hot electrons. For a 600 fs laser pulse and a spot size of 5 μm, $I_L =$ 3 x 10^{20} W/cm^2, the Beg's scaling gives the hot electron temperature at around 1 MeV. With a target volume of 100 x 100 x 2.4 μm^3, which estimates hot electron fraction inside the target at around 1%. It should be noted that this is without including hot electrons that have escaped the target or ones in the pre-plasma.

2.4 Radiation Transfer

In short pulse laser produced plasmas, the resulting plasma has two electron distributions, a thermal and a hot electron population which is typically a thousand times more energetic than the thermal. Radiation from the interaction between the two populations can be used to infer T_e the electron thermal temperature, T_h the hot electron temperature, and $f=n_h/n_e$ is the fraction of hot electron density to thermal electron density. Therefore, there is a need to understand the underlying atomic processes that govern the emission spectrum and to fully predict the spectral emission, ionization state, probability of escape, and transport quantities need to be known. The atomic transitions that are used to define a particular ionization state and photon emission will first be presented. Then, a review of radiation transport and method of calculating level populations to predict escaped radiation from the system will be discussed. Finally, approximations used in the calculation of stimulated emission and absorption through the use of an escape factor will be examined.

2.4.1 Radiative transitions

Consider two energy levels (i,j) of bound electrons of an ion, where level j is a more excited state than level i. Electrons can make several types of radiative transitions between these two levels. First, an electrons in an excited state n_i, can decay spontaneously to a lower level n_j and emit a photon, with frequency v, with energy hv that equals the energy difference between the upper and lower states. This process is known as *spontaneous emission* given by

$$n_j^z \rightarrow n_i^z + h\nu \tag{2.52}$$

where. The probability per unit time of this transition happening is defined by Einstein's A_{ij} coefficient. An atom with the electron in the lower level may absorb a photon, with energy hv, by a transition to the upper level. This process is know as *stimulated absorption* represented by,

$$n_i^z + h\nu \rightarrow n_j^z \tag{2.53}$$

The decay from E_j to E_i can occur in the presence of radiation and the probability of the event can be calculated using Einstein's B_{ij}. The inverse process being *stimulated emission* as represented in the following,

$$n_j^z + h\nu' \rightarrow n_i^z + h\nu'' + h\nu''' \tag{2.54}$$

where hv' is the energy of an incoming photon, hv' has energy that equals the energy difference between the upper and lower states, and $hv'''= hv' - hv''$. Its rate is likewise proportional to Einstein absorption probability B_{ij}. In the process of *photoionization* or bound-free absorption is represented by,

$$n_j^z + h\nu \rightarrow n_g^{z+1} + e \tag{2.55}$$

where a photon is absorbed and a bound electron is ejected. The inverse process of a free electron dropping into a bound state with the creation of a photon whose energy equals the sum of the electrons kinetic and binding energy is called *direct radiative recombination* represented by,

$$n_g^{z+1} + e \rightarrow n_i^z + h\nu \tag{2.56}$$

The photoionization and radiative recombination rate is a function of cross section of their respective processes and radiation field intensity over all frequencies.

2.4.2 Collisional processes

The collisional rate C_{ij} includes only inelastic collision processes where an ion interacts with an electron or ion which results in a change in its bound state. The rate is a function of the collisional cross section for an excitation or ionization of an electron in a particular energy level. The cross section, $\sigma_{ij}(v)$, is integrated over a velocity distribution $f(v)$ starting from a threshold velocity v_{th}.

$$n_i C_{ij} = n_i n_e \int_{v_{th}}^{\infty} \sigma_{ij}(v) f(v) v dv \tag{2.57}$$

Collisional processes of interest include:

Collisional ionization,

$$n_i^z + e \rightarrow n_g^{z+1} + e + e \tag{2.58}$$

is when a free electron ionizes a bound electron. The initial ion may be in its ground state or any of its excited states. *Three-body recombination*, described by,

$$n_g^{z+1} + e + e \rightarrow n_i^z + e \tag{2.59}$$

is the inverse of *collisional ionization*. Two free electrons approach an ion; one is captured and the other carries away the extra energy. Rates scale strongly with principle quantum number, and hence recombination into highly excited states is favored. The next two bound-bound processes may be induced by collisions with electrons of with other ions. *Collisional excitation*,

$$n_i^z + e \rightarrow n_j^z + e \tag{2.60}$$

is where a bound electron in a lower state is excited into an upper state. Its inverse process is *collisional dexcitation*,

$$n_j^z + e \rightarrow n_i^z + e \tag{2.61}$$

Dielectronic recombination is an important process with doubly-excited states of the ion.

$$n_g^z + e \rightarrow n_{j,j'}^{z-1} \rightarrow n_j^{z-1} + h\nu \tag{2.62}$$

A collision of an energetic electron with a ground state ion can result in its capture and simultaneous excitation of a bound electron to form a doubly excited state. This intermediate state will either eject an electron (Auger electron) or by radiative decay.

2.4.3 Collisional radiative model

A population kinetics model can be used to determine ionization and level population of a plasma for a given temperature and density. In order to predict the radiative behavior of any atomic species in a plasma, the population distribution over the number of interested states must be known. In this type of model a rate is used to represent a change in the population of a particular level *i* induced through radiation or by collision processes from level *j* either. The rate of change in the population of level *j* from level *i* is represented by $R_{ji,}$ and the depopulation of *i* to level *j*, represented by R_{ij}. By writing an equation for each bound state of an ion n_j, the set will describe the instantaneous bound state population distribution of the plasma. The radiation field is then obtained by solving the radiation transport equation. Furthermore, since this calculation is sequential, namely the populations calculation is solved before the radiation transport calculation, to be able to account for the stimulated radiative processes, the two systems need to be solved self-consistently.

2.4.4 Rate equations

For a system that is in *thermodynamic equilibrium TE*, the principle of *detail balance* requires that the rate of an atomic process is equal to its inverse process of all interested states, in other words,

$$0 = \sum_{j \neq i} [n_j A_{ji} + (n_j B_{ji} - n_i B_{ij}) I(v_{ij})] \tag{2.63}$$

and

$$0 = \sum_{j \neq i} [n_j C_{ji} - n_i C_{ij}] \tag{2.64}$$

where A_{ji}, B_{ji}, and B_{ij} are Einstein coefficients, n is the level population, and $I(v_{ij})$ is the specific intensity of radiation that is relevant to the transition. Collisional processes with rates C_{ji} and C_{ij}, are expected to be in detail balance whenever the velocity distribution is in equilibrium (Maxwellian distribution). In this configuration, the system is characterized by several factors which simplifies the calculation to describe emergent radiation. The velocity distribution of the ion and electron velocities is a Maxwellian and can be described in terms of a single temperature T. Therefore, the bound state population fraction is governed by Boltzman statistics and ionization stage distribution is governed by the Saha relationship. Finally, the radiation field emitted by the system has a Plank distribution.

Plasma in local thermodynamic equilibrium LTE, has population distributions that are described by statistical laws, only that radiation field is no longer Planckian and will depend on local plasma conditions, level populations, and atomic transition probabilities.

In non-LTE plasmas, the detailed balance is non-zero and hence a net rate from these processes. The balance equation is rewritten and expressed as,

$$\frac{dn_i}{dt} = \sum_{j \neq i} [n_j A_{ji} + (n_j B_{ji} - n_i B_{ij}) I(\nu_{ij}) + n_j C_{ji} - n_i C_{ij}] \tag{2.65}$$

and must be solved for every interested level. The calculation of each process, for each ion state, is generally performed with the assistance of a computer and can take several seconds to days depending on the number of the interested transitions.

2.4.5 Transfer of radiation

For the calculation of $I(\nu_{ij})$ in Eq 2.65, escaping radiation must be solved for. Radiation from an emitting body, dE passing though a unit area dS per unit time dt in frequency interval $d\nu$ and solid angle $d\omega$, can be described by the spectral radiation intensity a $I(\boldsymbol{r}, \boldsymbol{n}, \nu, t)$ defined at position $\boldsymbol{r}$ with direction $\boldsymbol{n}$ and with frequency ν and time t and has dimensions of ergs/cm^2/str/Hz/sec.

$$I(\boldsymbol{r},\boldsymbol{n},\nu,t) = \frac{\delta E}{dS\, d\nu\, d\omega\, dt} \tag{2.66}$$

Emissivity, $\eta(r, n, \nu, t)$, is defined as the energy emitted by the volume element in direction $\boldsymbol{n}$ into the solid angle $d\omega$ in a frequency interval $d\nu$ within a time dt. Radiation from the emitting body can be expressed in terms of emissivity with as, $\delta E = \eta(\boldsymbol{r},\boldsymbol{n},\nu,t)\, dS\, ds\, d\omega\, dt$, with dimensions of ergs/cm^3/str/Hz/sec. An extinction coefficient, or opacity, $\chi(\boldsymbol{r}, \boldsymbol{n}, \nu, t)$, with units 1/cm, is defined as the fraction of energy removed from the incident radiation intensity $I(\boldsymbol{r}, \boldsymbol{n}, \nu, t)$ by the volume as, $\delta E = \chi(\boldsymbol{r},\boldsymbol{n},\nu,t)\, I(\boldsymbol{r},\boldsymbol{n},\nu,t)\; dS\, ds\, d\omega\, dt$.

The difference between the amount of energy which exits the volume at $(\boldsymbol{r} + \Delta\boldsymbol{r}, \boldsymbol{t} + \Delta\boldsymbol{t})$ and that of the incident energy entering at $(\boldsymbol{r}, \boldsymbol{t})$ must equal the amount of energy emitted minus the energy absorbed in the volume to give,

$$\left[I(\boldsymbol{r},\boldsymbol{n},\nu,t) - I(\boldsymbol{r}+\Delta\boldsymbol{r},\boldsymbol{n}+\Delta\boldsymbol{n},\nu,t)\right] = \left[\eta(\boldsymbol{r},\boldsymbol{n},\nu,t) - \chi(\boldsymbol{r},\boldsymbol{n},\nu,t) I(\boldsymbol{r},\boldsymbol{n},\nu,t)\right] ds\, dS\, d\nu\, d\omega\, dt \tag{2.67}$$

The change in radiation intensity, expressed in terms of derivatives, becomes the time-dependent equation of transfer

$$\left[\frac{1}{c}\frac{\partial}{\partial t} + \boldsymbol{n}\nabla\right] I(\boldsymbol{r},\boldsymbol{n},\nu,t) = \eta(\boldsymbol{r},\boldsymbol{n},\nu,t) - \chi(\boldsymbol{r},\boldsymbol{n},\nu,t) I(\boldsymbol{r},\boldsymbol{n},\nu,t)\,. \tag{2.68}$$

If the time required for photons to travel a mean free path is short compared to the rate at which other changes occur in the plasma, then it can be assumed that the radiation transport is essentially instantaneous. Therefore, the time dependent term on the LHS of the transfer equation can be ignored. For analysis in one dimension, Eq 2.68 becomes,

$$\frac{\partial I(z,\nu)}{\partial z} = \eta(z,\nu) - \chi(z,\nu) I(z,\nu) \tag{2.69}$$

The quantity optical depth, τ, is defined by,

$$\tau(z,\nu) = \int_{z}^{z_{\max}} \chi(z,\nu)\, dz \tag{2.70}$$

where z_{max} is the surface boundary of the assumed one dimensional volume. The optical depth $\tau(z,v)$ at the point z is therefore the integrated opacity along the line of sight from the point z to the edge of the plasma. A plasma that are described as optically thick has τ » 1, and optically thin is when τ « 1. Now, if $z = 0$ is taken, then $\tau(z,v)=0$ and differentiating Eq 2.68 gives, $dt(z,v) = -c(z,v)dz$. Substituting this equation back into the transfer equation will yield the transfer equation as a function optical depth,

$$\frac{\partial I(z,v)}{\partial \tau(z,v)} = I(z,v) - \frac{\eta(z,v)}{\chi(z,v)} \tag{2.71}$$

The ratio between the total emissivity and opacity is called the source function S. Rewriting the equation assuming no variations in space, Eq 2.71 becomes,

$$\frac{\partial I_v}{\partial \tau_v} = I_v - S_v \tag{2.72}$$

For a finite plasma that has thickness $z = z_2 - z_1$, the integral form of the transfer equation is,

$$I_v(\tau_1) = I_v(\tau_2)e^{(\tau_2-\tau_1)} + \int_{\tau_1}^{\tau_2} S_v(\tau_v)e^{-(\tau_v-\tau_1)}d\tau_v \tag{2.73}$$

The first term of Eq 2.73 is attenuation of external radiation passing though the plasma while the second term represents radiation from the plasma itself.

2.4.6 Einstein relations

To relate emissivity and opacity, used in the transfer equation, to specific atomic transitions, Einstein's coefficients is used. Emissivity, η, is a function of Einstein's spontaneous and stimulated emission coefficients and the population of initial state of the atom which is calculated by the rate equation. The emission coefficient is represented by,

$$\eta = \frac{h\nu_{ji}}{4\pi} n_j A_{ji} \tag{2.74}$$

Likewise, opacity is a function of the population of the initial state and Einstein's stimulated emission and absorption coefficient. The absorption coefficient, χ, at which energy is removed from the radiative field and used to excite bound electrons into upper states is written as,

$$\chi = \frac{h\nu_{ji}}{4\pi}(n_i B_{ij} - n_j B_{ji}) \tag{2.75}$$

Then the connection is complete when these two equations are incorporated into the source function found in Eq 2.71 such that,

$$S = \frac{\eta}{\chi} = \frac{n_j A_{ij}}{n_i B_{ij} - n_j B_{ji}} \tag{2.76}$$

2.4.7 Escape Factor

In collisional radiative models, the calculation for $I(\nu_{ij})$ follows the populations calculation. Physically, the processes cannot be separated. Without knowing $I(\nu_{ij})$ during the level population calculation, approximations are used. At the limit that radiation does not effect level populations, stimulated processes can be neglected.

However, if internal radiation field is sufficiently intense to change the population distribution by reabsorption of self emitted photons, the effect of $I(\nu_{ij})$ will be important. The most common method to approximate the effect of an internal radiation field is with the use of an escape factor Λ, which was first discussed by Biberman and Holstein [75-78]. The escape factor, Λ, is used to represent spontaneous emission, stimulated emission and photoabsorption,

$$n_j A_{ji} \Lambda = n_j A_{ji} + (n_j B_{ji} - n_i B_{ij}) I(\nu_{ij}) \tag{2.77}$$

so that the rate equations to populate excited states Eq 2.65 becomes,

$$\frac{dn_i}{dt} = \sum_{j \neq i} [n_j A_{ji} \Lambda + n_j C_{ji} - n_i C_{ij}] \tag{2.78}$$

This method has been proven to be effective for modeling optically thick plasmas [79]. Also, since Λ is geometry dependent, approximations for planar, cylindrical and spherical plasmas must be used accordingly.

2.4.8 Production of K-alpha from energetic electrons

Hot electrons produced by the various laser absorption mechanisms discussed in Section 2.2, have sufficient energy to collisionally ionize K-shell electrons of neutral atoms and ions in the target. This leaves the atom in an unstable state whereby an electron from the L-shell fills the vacancy and the surplus energy is released through Auger transition or a characteristic photon, known as the K-alpha. The cross-section of K-shell ionization by electron impact can be estimated analytically [80-81] or experimental data [82] can be used. The cross-section peaks at approximately three times ionization energy and for relativistic electrons the cross section does not decrease, but increase again. For copper, relativistic effects become significant when incident electrons are above 1 MeV [83].

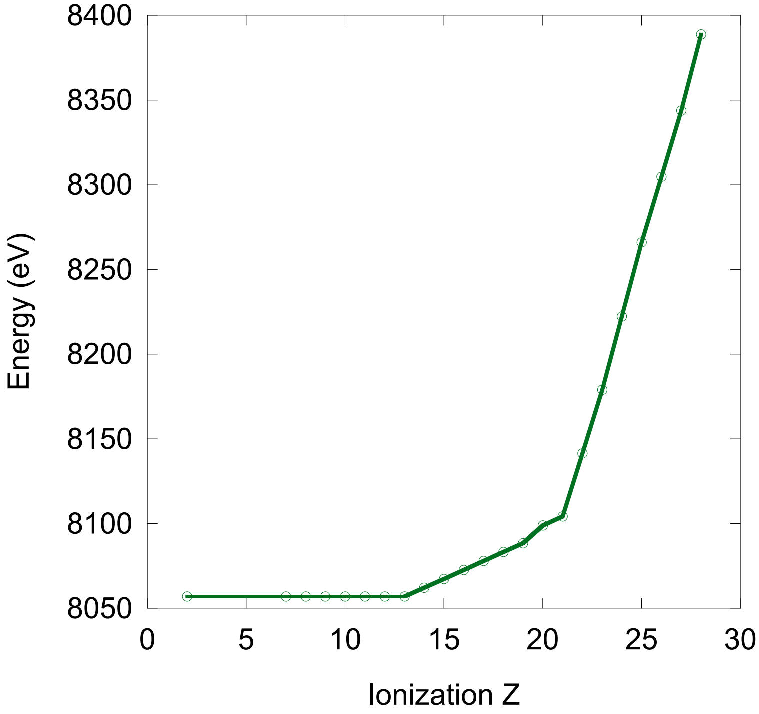

Figure 2.2: K-alpha photon energies for titanium as a function of ionization state of the atom.

The characteristic that is desirable about using K-shell emission as a diagnostic is the fact that the wavelength of the K-alpha is dependent on the ionization of the particular atom. For an ion with some ionization *Z*, screening of the electrons is reduced and therefore increasing the ionization energy of the K-shell electron. Experimental K-alpha photon energies for titanium and copper for ionization states from neutral to Hydrogen-like have been collected by House *et*. *al*. [84] and are are shown in Fig 2.2 and Fig 2.3 respectively. Exact ionization energies are calculated with the aid of a computer model which can generate ionization energies for many electron configurations for any one ionization state.

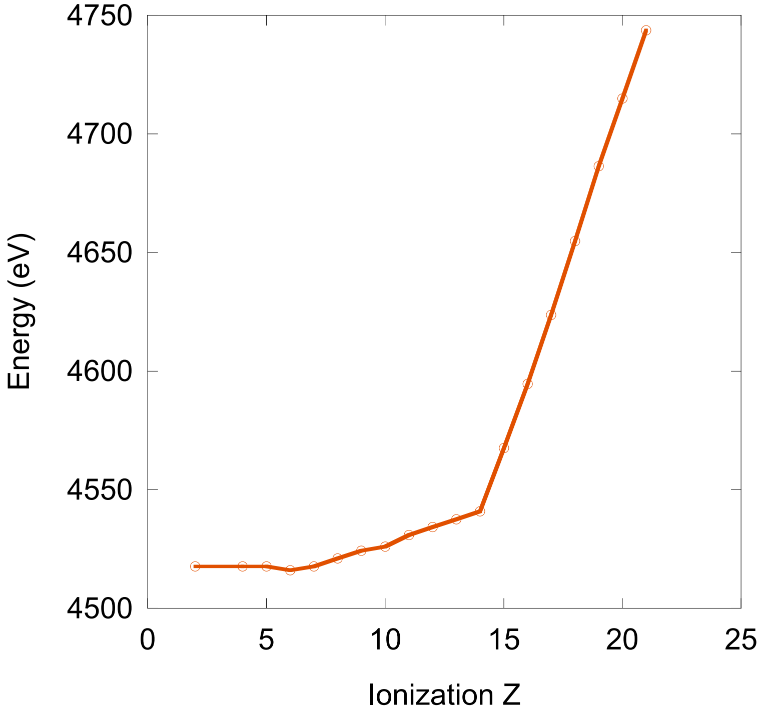

Figure 2.3: K-alpha photon energies for copper as a function of ionization state of the atom.

Chapter 3

High Intensity Short Pulse Lasers and X-ray Diagnostics

This chapter describes current high intensity short pulse laser design and diagnostics used in the experiments described in this thesis. First, the process of Chirped Pulse Amplification used at the Vulcan Laser at the Rutherford Appleton Laboratory and the Titan Laser at Lawrence Livermore National Laboratory is discussed. Then two crystal spectrometers designed to record K-shell x-ray emission is presented. The first is a flat crystal spectrometer. K-shell x-rays are generally weak compared to the background so a high reflectivity crystal is necessary and a mosaic crystal was used for this experiment. The third detector is a monochromatic imager using a quartz crystal with a narrow x-ray bandwidth to provide spatial information about the emitting body. The image plate was used as the recording media for the crystal spectrometer and the imager. It was chosen for convenience, resolution and efficiency.

3.1 High Intensity Short Pulse Lasers

3.1.1 Chirped Pulse Amplification

Strictland and Mourou's concept of *Chirped Pulse Amplification* (CPA) for laser light in 1985 [85], has enabled intensities pushing beyond 10^{21} W/cm^2. The light intensity of traditional lasers without CPA, is limited due to the low damage threshold of the amplifiers and the induced non-linear self-focusing at high fluence levels. To circumvent this problem, either the diameter of the beam or the duration of the pulse must increase. The former requires large amplification optics, which is limited by manufacturing, while the latter, also known as then CPA technique, has been instrumental in pushing laser intensities greater than 10^{21} W/cm^2.

The high intensity chirped pulse starts as a low energy, broad-bandwidth ~100 fs pulse from an oscillator. Then the pulse enters into the stretcher where a chirp is imposed on the pulse using diffraction gratings. At the output of the stretching phase, one end of the broadband spectrum of the incoming pulse leads or lags the other end of the spectrum in time. The spectrum of the pulse is unchanged, however, the duration of the pulse has increased by four orders of magnitude or more and intensity decreases by that same factor. Now, with a longer duration pulse, it is then amplified through conventional discs or rods or through non-linear optics. Compression of the pulse takes place right before a parabola focuses the light to microns in diameter only to be limited by diffraction.

Many current high intensity short pulse lasers use Optical Parametric Amplification (OPA) in the pre-amplification stage with a non-linear crystal after the stretching stage. The entire system is then called a Optical Parametric Chirped Pulse Amplification (OPCPA). With this type of amplifier, a single pass through one or several pumped non-linear crystal(s) replaces a multiple pass or regenerative amplification stage. This type of amplifier is more compact, gains that can be attained are significantly higher than glass amplifiers, and quality of the beam profile is smoother.

3.1.2 100-TW CPA Vulcan Laser

The Vulcan Laser is one of several laser systems of the Central Laser Facility at Rutherford Appleton Laboratory in the UK. The system is an eight beam Nd:glass laser which is comprised of six long pulse (80 ps - 2 ns) and two short pulse beams. One of the short pulse beams, with pulse length between 0.7 - 1.3 ps, is diverted into Target Area West (TAW) and delivers laser intensities up to 5 x 10^{19} W/cm^2 into the interaction chamber.

Fig 3.1 shows the layout of the 100 TW CPA laser system [86-87]. This short pulse beam line consists of four sections: the front end (oscillator and stretcher), the amplifiers, compression, and the interaction chamber.

The oscillator, a Kerr-lens mode-locked (KLM) Tsunami Oscillator, uses a Argon ion laser pumped Ti:Sapphire crystal to produce 5 nJ, 120 fs pulses at 80 MHz with wavelength 1053 nm. Then the pulse goes into a double pass Nd:glass rod preamplifier and then a double pass diffraction grating stretcher positively chirps the femtosecond pulse to 600 ps. The pulse passes through two more Nd:glass rod pre-amplifiers and Vacuum Spatial Filters (VSF), which are composed of two lenses and a pinhole in between for spatial filtering. The final amplification system consists of a double-pass 108 mm aperture disc amplifier followed by a single pass 150 mm aperture disc amplifier to increase the energy to 250 J.

The beam is sent to the target area to be recompressed and focused onto the target. The compressor consists of a pair of single-pass gratings in which the 600 ps pulse is recompressed to about 1 ps. Efficiency of the compressor is 75% which puts the energy on the target of about 75 J. The high energy ultra-short CPA pulse is diverted into the target interaction chamber by a steering mirror immediately passing after the second grating and then focused onto the target by an f/4 off-axis infrared parabolic mirror.

A small amount of leakage light (~1%) from the recompressed CPA beam is fed into a laser diagnostics chain to give information on pulse duration, near field/far field beam profile, pre-pulse and spectral measurement.

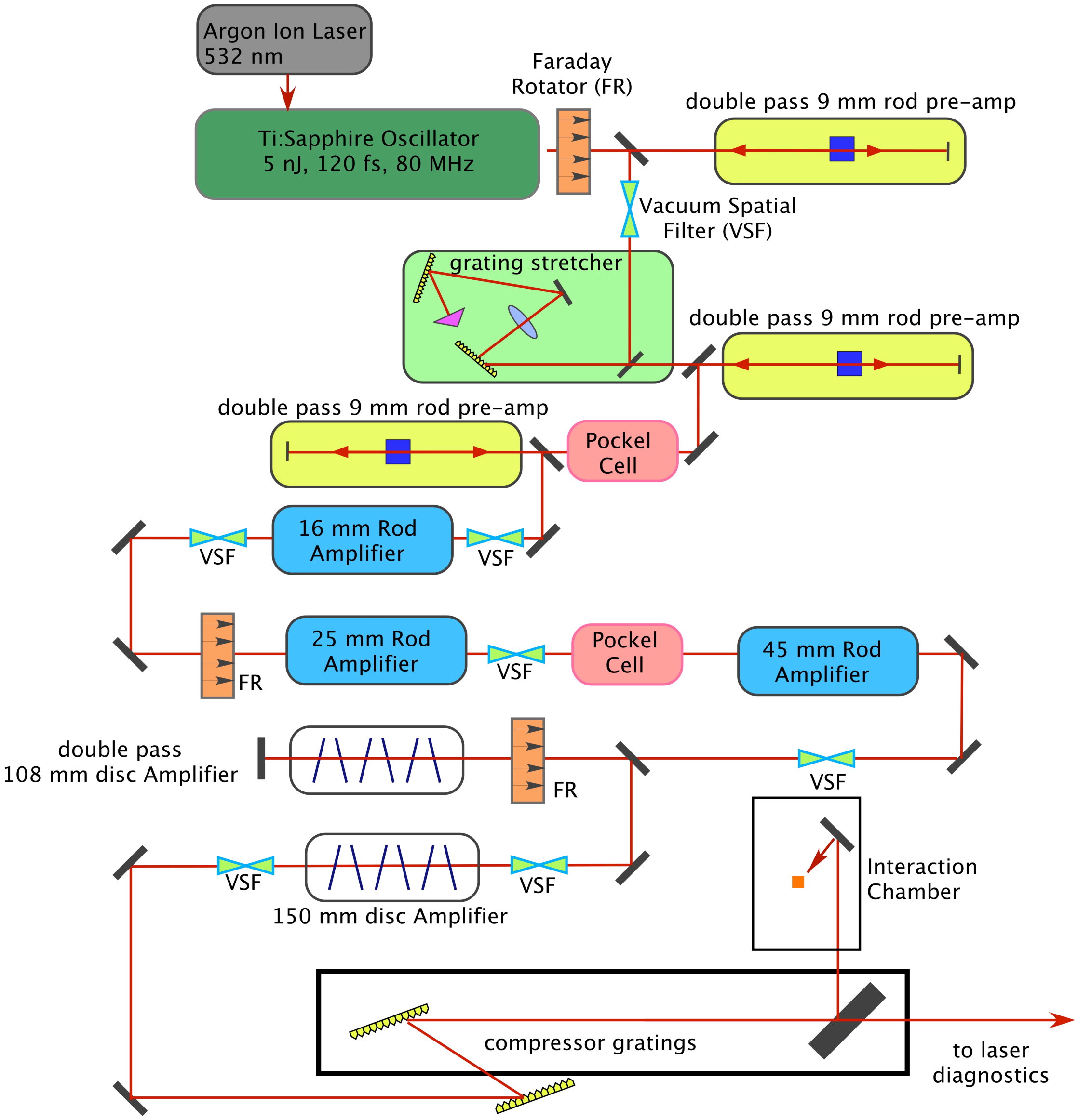

Figure 3.1: A schematic of the CPA laser beam line used in Target Area West.

3.1.3 Titan Laser

The Titan laser, shown in Fig 3.2, was built as an extension to the Janus Laser at the Jupiter Laser Facility at Lawrence Livermore National Laboratory [88]. The laser pulse begins as a femtosecond pulse with wavelength of 1053 nm in a Nd:Glass Time-Bandwidth Products Inc. GLX-200 commercial oscillator. The pulse makes eight passes in an Offner stretcher, which stretches the pulse to 1.6 ns. Pulses are amplified through two stages of OPA using a BBO crystal and then through the Janus amplification chain which consists of 25 and 50 mm rods and 9.4 and 15 cm disks. For the compression stage, a pair of 40 x 80 cm multi-layer dielectric (MLD) gratings re-compresses the pulse to several picoseconds. After compression, the beam reflects off a final 45 degree turning mirror and enters the target chamber, where it is focused by an f/3 off-axis parabola with a focal length of approximately 80 cm. The beam as it enters the chamber is s-polarized.

3.1.4 High intensity short pulse laser limitations

There are a number of variables that affect beam quality and what is covered below include are those that are critical to the success of the experiment. One of the most overlooked specifications of the laser system is the contrast ratio, the ratio between any pre-pulses or the pedestal and the main pulse. Every laser system inevitably has precursor light that can originate from several places along the laser chain.

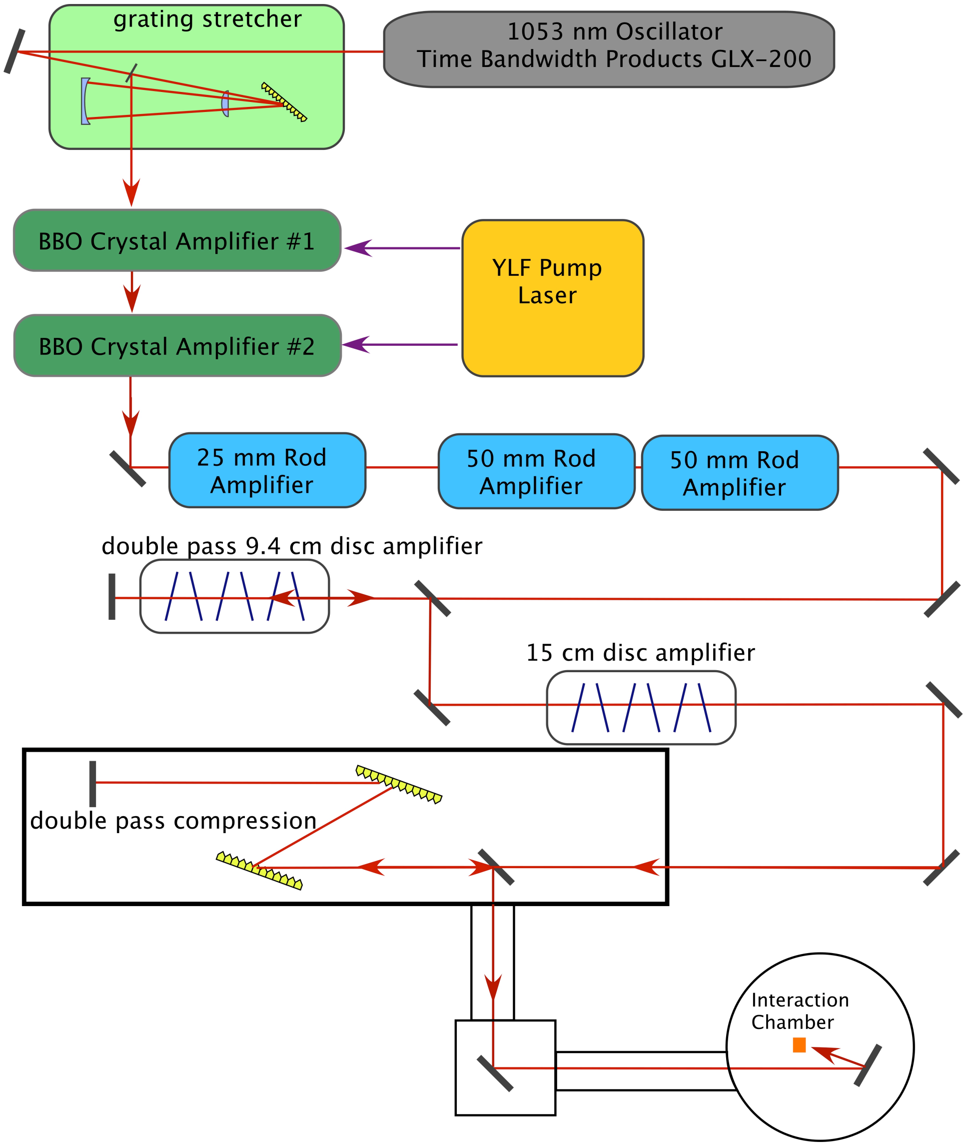

Figure 3.2: A schematic of the CPA arm of the Titan laser.

Amplified Spontaneous Emission (ASE) occurs in crystal amplifiers. The pump for the lasing medium can be microseconds long, so time when the laser pulse is not present, spontaneously emitted photons are amplified and sent through amplifiers further down the laser chain. Also, *parametric fluorescence* from the nonlinear crystals in the OPA can occur since the pump is nanoseconds in length. This undesired light is due to the fact that the pump duration in the amplifiers is longer than the input pulse and spontaneous emission occurs.

Ideally, the stretcher and compressor gratings are perfectly matched, resulting in a complete recompression of the pulse. However, misalignment between gratings can lead to imperfect recompression. This results in a pedestal that the main pulse is superimposed upon. With modern high power laser systems, the contrast ratio, the intensity of the main pulse to the intensity of a pre-pulse or pedestal, is typically on the order of 10^{-7} and improving with new designs and technology.

Gain narrowing in the amplifier crystal can lead to longer pulse than the desired pulse. Gain as a function of wavelength is non-uniform and therefore certain sections of the spectrum will experience more gain. This reduction in bandwidth, when the beam is recompressed, will result in a longer pulse [89].

Uniform pumping of the amplifiers is key to a good spatial profile of the beam. However, with such large amplifying mediums, it is impossible to pump them uniformly. Additionally, since the index of refraction is dependent on temperature, any thermal gradients within the material will degrade spatial quality. During a typical experiment, the laser system is fired several times in a day. The first shot will be fired with completely cold amplifiers, but for subsequent shots, even with hours between shots there is not sufficient time to completely cool amplifiers and beam quality will deteriorate.

3.2 X-ray Reflective Media

Reflective crystal can be used to collect x-rays emitted from the target. Crystals have a natural structure that resembles a multilayer reflector. The planes in the crystal are created by the regular positions of the atoms and are described by a unique Miller indices (*hkl*). The distances between the planes is given by $d = a/(h^2 + h^2 + l^2)^{1/2}$ where $a = (hkl)^{1/3}$.

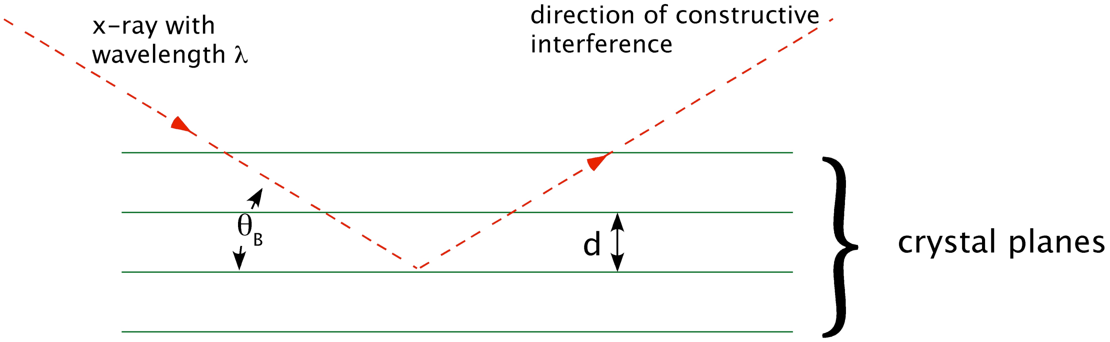

Figure 3.3: Only x-rays that reflect off the crystal planes at the angle specified by the Bragg condition will constructively interfere.

Incoming light, as shown in Fig 3.3, at a particular angle, will reflect off the planes either constructively or destructively interfere. The angle for constructive interference θ_B, off a given crystalline plane *(hkl)*, with plane distance d for a given photon energy is given by Bragg's law, $2d \sin \theta_B = n\lambda$. The integer n gives the order of diffraction.

3.2.1 Spherical Crystals

Spherical crystals are curved crystals that focus light to a point which makes it ideal for imaging. The *rocking curve* is the measure of angular range over which the diffracted monochromatic light is spread spatially due to crystal imperfection. It is expressed as a reflective intensity versus incident angle. The *Darwin width* is the FWHM of peak reflectivity described by [90],

$$\omega_D = \frac{4r_o\left|F\right|d^2}{\pi V} tan\theta_B \tag{3.1}$$

where r_o is the classical electron radius, F is structure factor, d is crystal spacing, and V is the unit cell volume.

3.2.2 Mosaic Crystals

Each plane of a perfect crystal runs parallel to each other. Mosaic crystals are composed of many smaller perfect crystals with adjacent blocks slightly offset in angle. The variation in angle of the crystallite planes is defined by the *mosaic spread* ζ. With a mosaic crystal, there will be a number of smaller crystals at different depths that satisfy the Bragg condition. As shown in Fig 3.4, for a given wavelength a, there are several crystallites at different locations that it will reflect off of, thus distorting the original source. Additionally, there will be a slightly different wavelength b that will be reflected and land on the detector plane at the same location as wavelength a. Since there will be a number of crystallites taking part in reflecting a certain wavelength, reflectivity is higher than non-mosaic crystals. However, resolution, due to overlap of a small interval of wavelengths at the detector plane, is poor compared to a non-mosaic crystal.

With perfect crystals, reflectivity has dependence on the thickness of the crystal. The term *primary extinction* describes how an incident beam can be lose power by successive reflections within the crystal. In mosaic crystals, the planes in the crystallites are too small for primary extinction to be significant. The term *secondary extinction* describes how the incident beam is partially reflected by the crystallites at the surface, that might not have the correct orientation, before reaching lower lying blocks. This again has a incident power loss effect and both extinction mechanisms represents a loss in reflectivity. However, in mosaic crystals this is countered by the fact that there are many crystallites, in the lateral direction and at various depths, participating in the reflection process. Therefore, as thickness increases, so does the reflectivity up to a saturation point. For Highly Oriented Pyrolytic Graphite (HOPG) crystals with $\zeta = 2$ degrees, peak reflectivity is achieved with a crystal thickness greater than 350 μm [91].

Resolution can be estimated by the following equation [92],

$$\Delta s = 2D\, cos(\theta_B) \tag{3.2}$$

where Δs is spatial smearing at the detector plane. The variable D is the combined total of the secondary extinction depth and attenuation thickness due to photoelectric absorption and Compton scattering.

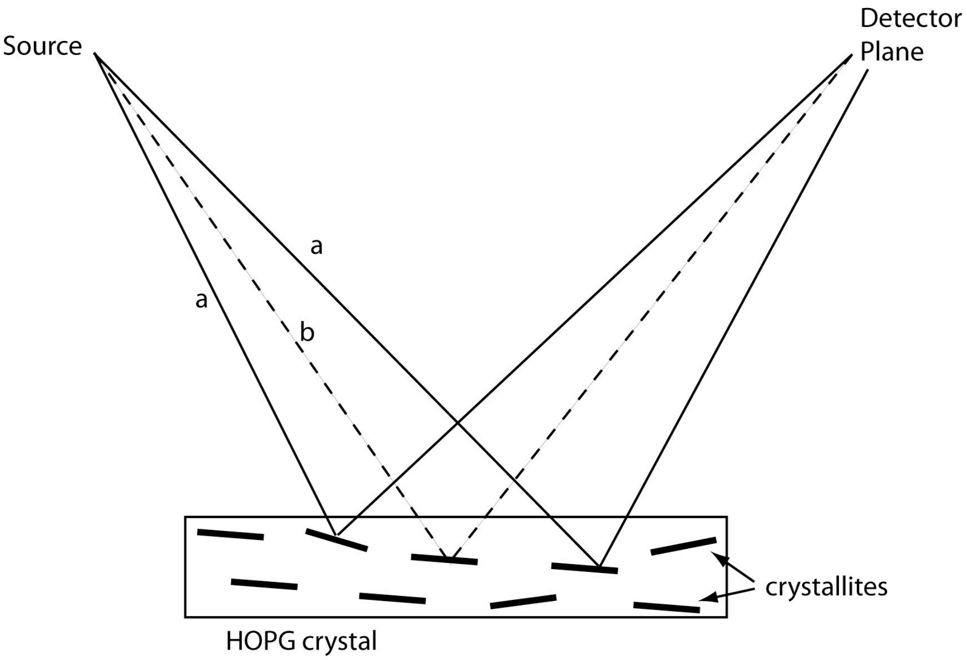

Figure 3.4: Light rays originating from the source are reflected off of independent planes that make up the mosaic crystal. There will be more than one crystallite, at various depths, that reflect light, within a small range wavelengths, to the same point on the detector plane. Also, x-rays of the same wavelength will find crystallites located elsewhere on the crystal that reflect light to a different location on the image plate. This increases reflectivity, but lowers the resolution capability.

3.2.3 Highly Oriented Pyrolytic Graphite

Highly Oriented Pyrolytic Graphite (HOPG) is an artificially manufactured graphite that has a mosaic structure. By using heat treatment at temperatures above 2500 K or by chemical vapour deposition, pyrolytic graphite is made. Then heat treatment with compression at temperatures above 3000 K produces highly oriented pyrolytic graphite. The final graphite mosaic is composed of large blocks, up to 1 mm in length with ζ of about 0.1 degree, and contains small crystallites that are aligned to better than 0.5 degrees [91].

For graphite, the planes of interest for our applications are the *(0,0,2n),* where n is the order number, and a $2d$ spacing of 6.708 Å. Reflectivity of the HOPG crystal has been reported to be ~ 45% at 8keV and peaks at 15 keV [91]. Resolution, defined by $\Delta E/E$, is calculated to be 1.94×10^{-3} using the intrinsic rocking curve for 4 keV x-rays, but has been measured to be 3×10^{-3} by Pak *et. al.* [93].

3.2.4 HOPG Spectrometer Setup

For the two experiments discussed in this report, the same type of HOPG crystal was used, but in different setups. At the experiment performed at Rutherford Appleton Laboratory, a ZYA grade HOPG crystal, manufactured by General Electric Advanced Ceramics (now called Momentive Performance Materials), with a mosaic spread $\gamma = 0.4^{\circ}$, was used. The HOPG crystal spectrometer setup and housing is shown in Fig 3.5. The Bragg angle used to position the crystal was 22 degrees to reflect 4-5 keV x-rays and the distance from the target is 20 cm.

The spectrometer was positioned below the horizontal axis as to not to block the line of sights of other diagnostic. The reflected x-rays off the crystal enters the detector housing through a 1 x 10 cm vertical slit to find the image plate. The image plate, FujiFilm BAS-TR, was wrapped in 5 μm of Al foil to make it light tight and the package was shielded in 6 cm of lead to reduce background. Additionally, there was a 5 x 5 cm^2 lead place between TCC and the image plate (not shown in Fig 3.5) to block direct radiation. Exposed plates were read using the FujiFilm BAS-1800 II with 50 μm scanning resolution, sensitivity of 4000, and dynamic range of 5.

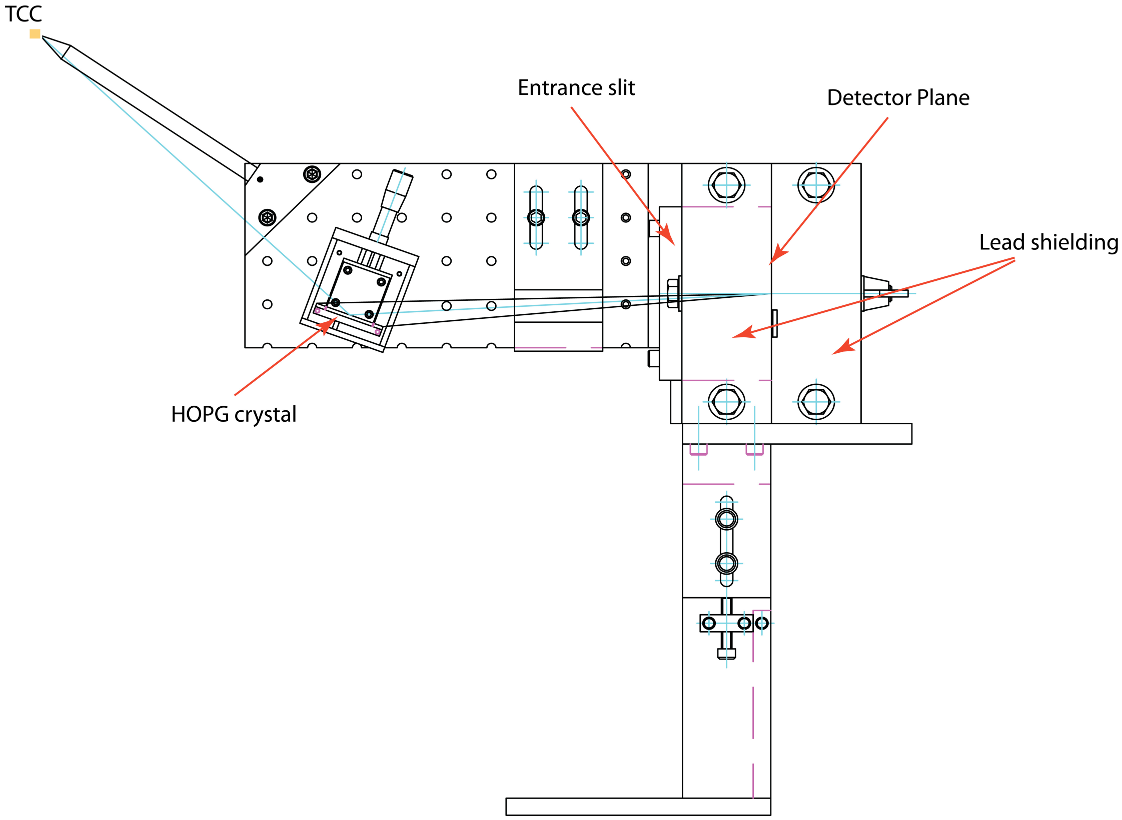

Figure 3.5: Drawing of the HOPG spectrometer used at the Vulcan Laser Facility. The target is located at TCC. X-ray emission is dispersed by the HOPG crystal, passes through the entrance slit to the image plate on the detector plane. The image plate is shielded from surrounding radiation by the lead. The crystal sits on a moveable stage and protected by 15 μm of mylar.

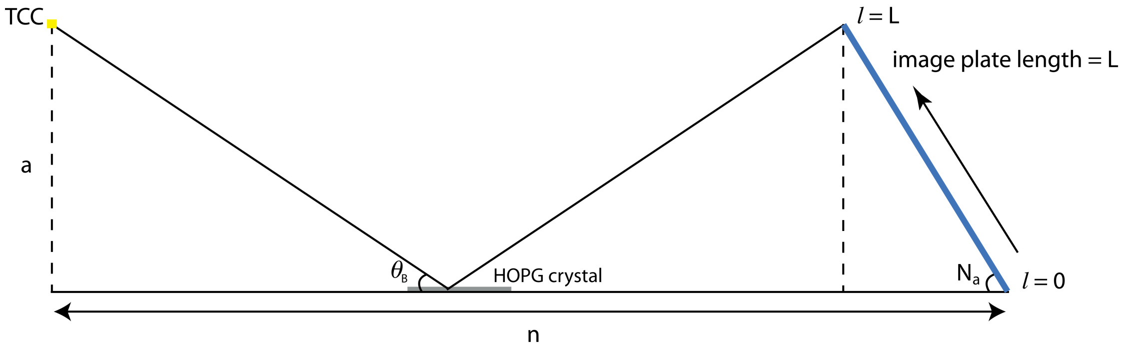

Figure 3.6: Positions of the HOPG crystal relative to TCC and the image plate detector in the spectrometer used at the Vulcan Laser Facility.

The measured spectral resolution of our HOPG crystal was $\Delta E/E = 1.2 \times 10^{-3}$. The dispersion relating the physical position of the line on the image plate to its corresponding wavelength was calculated by using the Bragg equation in first order, n=1. Accounting for the geometry of the spectrometer, as shown in Fig 3.6, a third order analytic dispersion curve given by,

$$\theta_B(l) = tan^{-1}\left(\frac{a + l\ sin(90 - N_a)}{n - l\ cos(90 - N_a)}\right) \tag{3.3}$$

where l is the location on the image plate with reference to the bottom edge of the image plate, $l = 0$. The dispersion relation was found to be 0.025 eV/μm on the image plate. The measured spectrum was then fitted on eight known points given by the theoretical positions of the oxygen-like to the He-like lines.

The HOPG spectrometer used at the Titan Laser experiment, as shown in Fig 3.7, has a slightly different housing, but designed to disperse 8-10 keV x-rays. The spectrometer was positioned 13 cm from TCC and x-rays enter the spectrometer though a 2 x 5 mm tungsten slit (not shown in the figure). The Bragg angle that was used to position the crystal was 12 degrees and a lead piece was positioned such that the detector sees no direct radiation from TCC. The image plate, FujiFilm BAS-MS, was fully enclosed 18 μm of Al foil and shielded with 1.5 cm of lead. Exposed plates were read using the FujiFilm FLA-7000 with 25 μm scanning resolution, sensitivity of 10000, and dynamic range of 5. In this setup, a linear dispersion relation of 0.12 eV/μm was used rather than a non-linear relation used with the previous spectrometer for simplicity. The relation was determined by using three known lines of copper and tungsten in the range of 8 to 10 keV.

3.2.5 K-alpha Imager

The K-alpha imager is set up to monochromatically record spatial information about the origin of K-alpha x-rays. The imager is composed of three components, a spherical SiO_2 crystal, and a FujiFilm BAS-TR image plate as the detector, and a lead block. The setup of the imager is shown in Fig 3.8 where x-rays with an energy of 4.5 keV originating from TCC is reflected off the crystal and redirected to the detector plane. A lead block is placed in a location such that the direct light from TCC does not reach the detector.

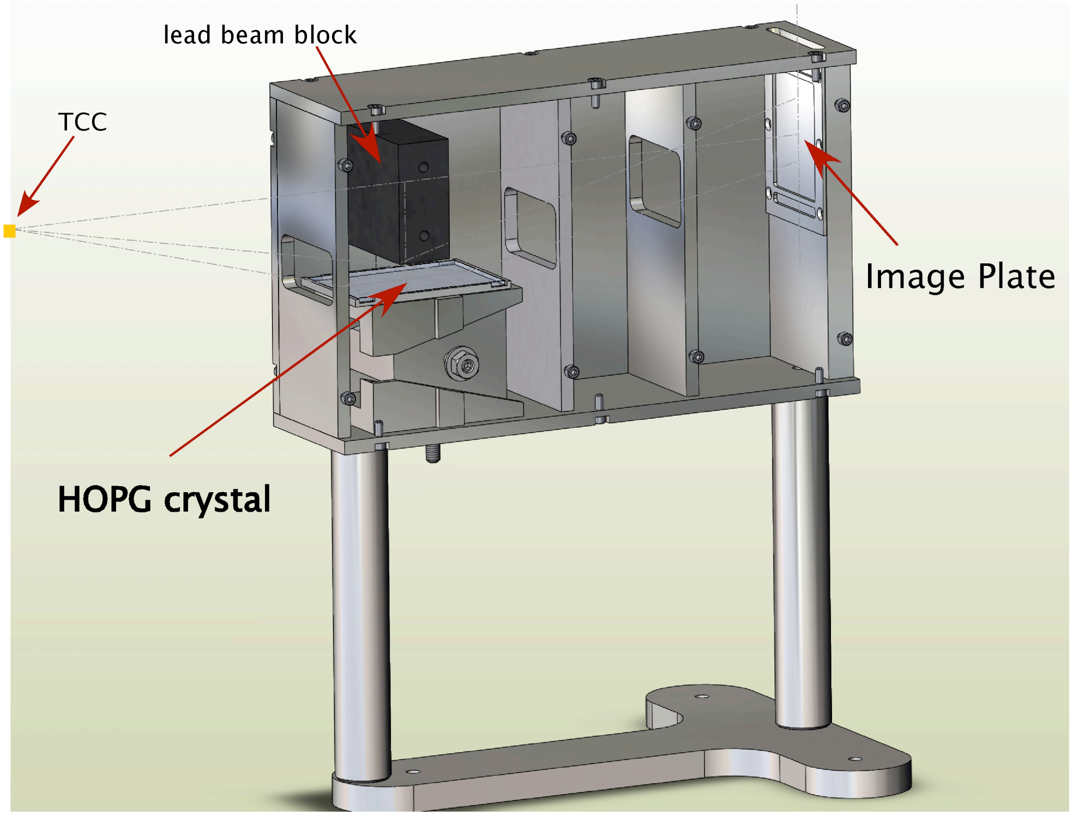

Figure 3.7: Drawing of the HOPG spectrometer used at the Titan Laser at the Jupiter Laser Facility. The target is located at TCC. X-ray emission is dispersed by the HOPG crystal, passes through two aluminum collimators to the image plate. The lead beam block shields the image plate from direct radiation from the target.

The crystal used is a quartz *(203)* crystal with a *2d* spacing of 2.749 Å and a 356 mm radius of curvature from Extar [94]. The rocking curve is $2\theta = 0.05$ degrees, which translates to a bandwidth of is 2.67 eV [95] for this crystal. The resolution of the imager is given by,

$$\sigma = (M+1)(1-\sin\theta)(\frac{D}{M}) \tag{3.4}$$

where D is the diameter of the aperture, M is the magnification, and θ is the rocking curve angle [96]. The magnification was set at 8 due to the constraints of the target chamber setup. The calculated resolution is 20 μm for aperture of 16 mm, however, since the image plate scanner resolution of 50 μm, that will define the imager resolution.

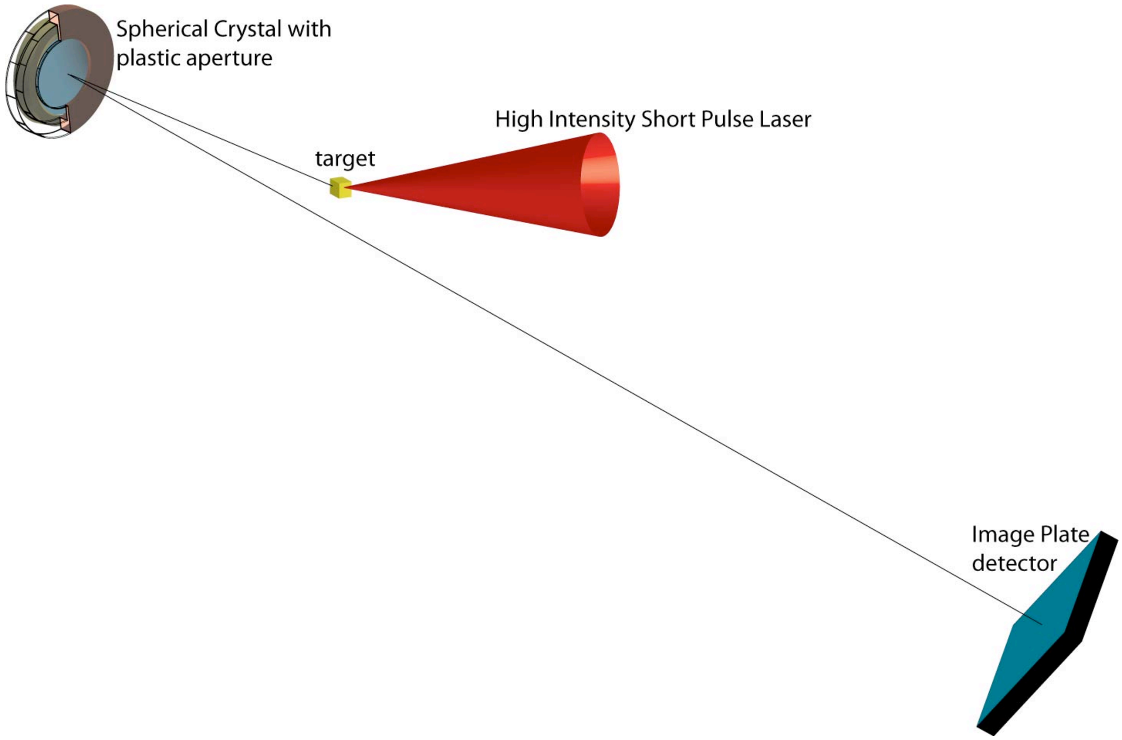

Figure 3.8: Diagram showing the K-alpha imaging system. X-ray emission from the target is reflected and focused by a spherical crystal onto an image plate.

3.2.6 Image Plates

Passive x-ray detectors are generally preferred since they are impervious to the electromagnetic pulse generated by the interaction. Image plates are now commonly used and have numerous advantages over film and other x-ray detectors. The plate can be cut and bent to any geometry, has low noise and high sensitivity, linearity better than 1%, better than 2% error in spatial distortion [97], and five orders of magnitude dynamic range in the FujiFilm BAS-TR plate [93].

Image plate takes advantage of fluorescing materials that react to high energy photons and particles. The compound used in the image plates is $BaFBr_{0.85}I_{0.15}:Eu^{2+}$ made by FujiFilm Inc.

Sheets of tungsten and stainless steel of thickness ~250 μm provide a supportive substrate on which ~150 μm of $BaFI:Eu^{2+}$ powder in an organic binder is applied [98]. A 10 μm mylar overcoat is laid to prevent the powder from damage.

When an x-ray photon is absorbed by the phosphor matrix made of barium, fluorine, and iodine. The energy is used to ionize the erbium from Eu^{2+} to $Eu^{3+.}$ Then photoelectron enters into the conduction band and becomes trapped in a lattice defect temporally. Extraction of the data stored in the image plate requires de-excitation of the electron held in the lattice. The plate is inserted into a reader machine equipped with a laser, with wavelength 658 nm with energy less than 20 mW, and irradiates a small area of the plate to generate photostimulated luminescence (PSL), which is proportional to the number of trapped electrons. During this process, the trapped electron recombines with Eu^{3+} releasing a photon at 400 nm in about 800 ns. A photomultiplier tube collects the blue light and the process is repeated until the entire plate is read. The reading process removes 60-90% of the stored information so plates can be read again if desired [98].

Typically, there are multiple resolution settings on readers manufactured by FujiFilm. The He-Ne laser has a spot size of ~70 um. However, if scanning with a pixel size smaller than 100 um, it must be noted that the laser light will partially erase areas of the plate that have not been read. Therefore, the calibration must be known for each reader pixel size.

Unlike x-ray film or CCD cameras, the recorded data on image plates will degrade over time. The loss of data due to thermal recombination of the trapped electron is known as fading [98]. In practice, reading of each image plate after a set interval of time such that the data has faded from each image plate by the same amount.

Two types of FujiFilm image plates were used in the experiments, the BAS-TR and the BAS-MS. The BAS-TR plate does not have the plastic protective coating to eliminate photon absorption before reaching the sensitive layer. Also this plate has a blue dye mixed in with the phosphor to absorb stray laser light thus reducing the spread of the photostimulated luminescence during reading and therefore increasing the resolution. The BAS-MS plate has a protective plastic coating, but does not have the blue dye. There will be more PSL released by the white colored plate but resolution will be lower than plates with an absorptive blue dye and therefore higher signal sensitivity.

The raw data outputted by FujiFilm reading devices has an imposed logarithmic compression algorithm and must be converted back to a linear scale using the following equation,

$$PSL = \left(\frac{Res}{100}\right)^2 \times \frac{4000}{S} \times 10^{L \times \left(\frac{QL}{G} - \frac{1}{2}\right)} \tag{3.5}$$

where QL is the raw data, L is the dynamic range used in the scan equaling, S is sensitivity, Res is the size of the area of interest on the image plate corresponding to the data, and G is the number of bits used in the data stream.

Chapter 4

Plasma characteristics of tamped titanium foils irradiated at 10^{19} W/cm^2

Characterization of hot dense plasma created by a short pulse laser using spectral and spatial diagnostics will be presented in this chapter. The average ionization state of dense titanium plasma is determined using the spectral shifts of the K-alpha lines emitted from the bulk of the target. Then information about the peak plasma temperatures from the laser heated spot is inferred by measuring the emission from helium-like ions. In addition, the data suggests that the bulk and peak temperature of the target is dependent on the target size and tamper material. Finally, a discussion about how the scattering due to the *Z* of the target material can potentially effect the propagation of the hot electron beam.

4.1 Introduction

Dense titanium plasma has been heated to an electron temperature up to 1300 eV with a 100 TW, high intensity short-pulse laser. The experiments were conducted using titanium foils (5 μm thick) sandwiched between layers of either aluminum (1 or 2 μm thick) or CH plastic (2 μm thick) to prevent the effects of the pre-pulse. Targets of two different sizes, 250 x 250 μm^2 and 1x1 mm^2, were used. Spectral measurements of the titanium inner-shell emission, in the region between 4–5 keV, were taken from the front-side (i.e., the laser illuminated side) of the target. Comparison with collisional radiative and 2-D radiation hydrodynamics codes indicates a peak temperature of $T_{e,peak}$= 1300 eV of solid titanium plasma in ~0.2 μm thin layer. The data show large shifts in the K-alpha emission from open-shell ions suggesting bulk heating of the sample at near solid density. Higher bulk temperatures for aluminum tamped targets ($T_{e,bulk}$ = 100 eV) compared to CH tamped targets ($T_{e,bulk}$ = 40 eV) was observed. The results also show that the peak temperature is also a function of target material (high or low Z).

4.2 Experimental Setup

The experiment was carried out at the Vulcan Laser Facility at the Rutherford Appleton Laboratory (UK) as described in Chapter 3.1.2. Tamped solid foils were irradiated using the chirped pulse amplified (CPA) arm of the Vulcan laser delivering ~85 J of 1.053 μm p-polarized light with a 1.5 ps pulse length on target. The beam was focused down to a 10 μm diameter spot by a f/3 off-axis parabola. Focused intensities were on the order of 10^{19} W/cm^2. The targets (see Fig 4.1) consisted of a 5 μm thick titanium square either sized 1 x 1 mm^2 or 250 x 250 μm^2. The titanium layer was tamped by either 1 or 2 μm Al, or 2 μm CH on the front and the back-side of the target by a sputtering technique. The targets were mounted such that their normal was 30 degrees from the laser axis.

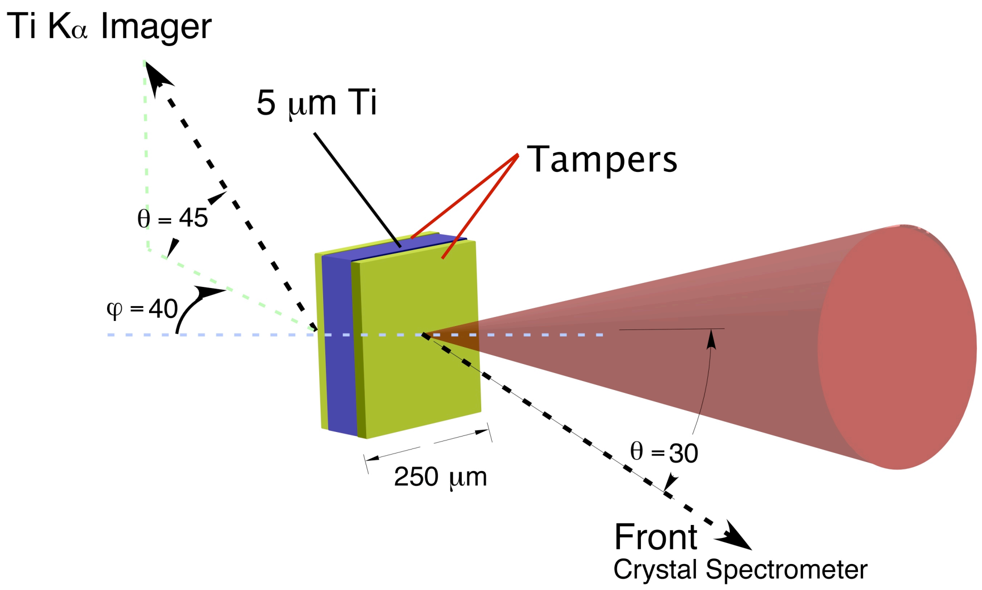

Figure 4.1: Experimental setup showing the target and the diagnostics viewing angles.

Diagnostic instruments included a spectrometer with a HOPG crystal and a crystal imager as described in Section 3.2. The spectrometer viewed the front of the target and 30 degrees below the horizontal plane. The K-alpha imager viewed the back of the target, 40 degrees from the laser axis along the horizontal plane and 45 degrees above the horizontal plane.

4.3 Experimental Results

4.3.1 Pre-Pulse Measurements

The contrast ratio between the pre-pulse and the main pulse was measured to be ~10^7 and the prepulse duration was ~0.5 ns as shown in Fig 4.2. Prepulse measurements were performed with a fast diode coupled to an oscilloscope with 20 GS/s sampling rate. In order to minimize the impact on the target by the prepulse, a selection of protective layers, aluminum and CH plastic of various thicknesses, were tested. The Al density (2.7 g/cc) is about twice the CH density (1.1 g/cc) and it was expected that a similar ablated mass by the pre-pulse as indicated by Key [99] at intensities of 10^{13} W/cm^2. The ablation rate for our pre-pulse level is approximately 10^5 g cm^{-2} s^{-1}. As an input for hydrodynamic simulations, the pre-pulse was modeled as a 0.5 ns long square pulse with an intensity of 10 TW/cm^2 on a 10 μm spot and 1 ps rise and fall times (see Fig 4.2). The 2-D radiation-hydrodynamics code *h2d* [100] was used to simulate the interaction of this pre-pulse on the target, as shown in Fig 4.3. The h2d package is a two dimensional (r-z) radiation hydrodynamics code with a multigroup diffusion treatment of radiation transport, flux limited diffusion modeling of electron conduction and Lagrangian hydrodynamics. In these simulations a flux limiter of 0.05 was applied to the electron conduction term, as appropriate for 1ω illumination. The SESAME [101] equation of state tables were used, and opacities were generated from an in-line average atom atomic physics model which assumes local thermodynamic equilibrium (LTE). In these simulations 30 radiation groups were employed, arranged logarithmically from 5 eV to 10 keV.

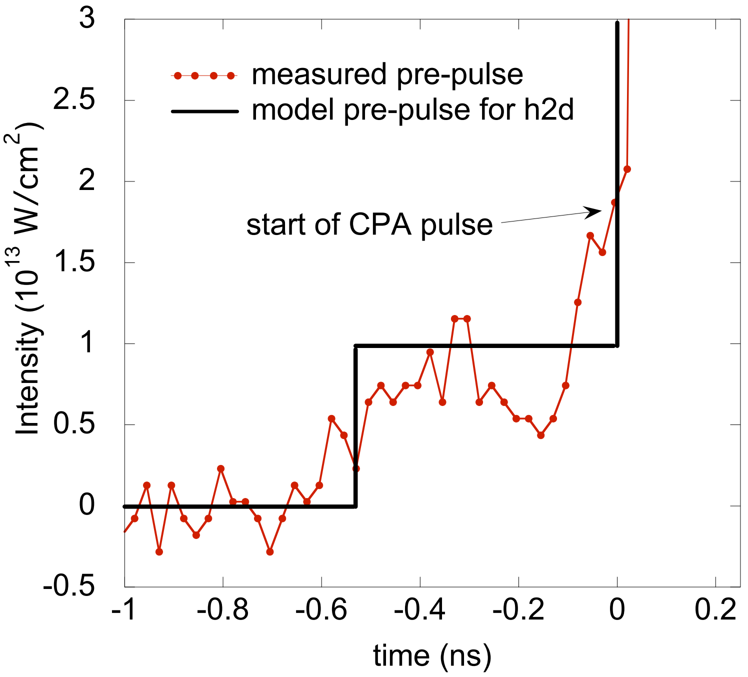

Figure 4.2: Measured laser pre-pulse ahead of the main CPA pulse. The solid line corresponds to the modeled pulse in the h2d simulation.

Simulations show that the 0.5 ns long pre-pulse launches a shock wave into the target, raising the temperature of the titanium layer to about 1-2 eV, but with the Ti layer remaining at near solid (Fig 4.3). In the simulations both the cases of Al and CH tampered foils were considered. The results show that the difference between Al and

CH tampers was minimal, likely being a consequence of impedance mismatching effects as the prepulse driven shock wave crosses the interface between the two materials. Along the axis of the laser peak densities were calculated to be in the order of 7-8 g/cc. In each case the tamper acts to keep the titanium layer at or above the original solid density of 4.5 g/cc.

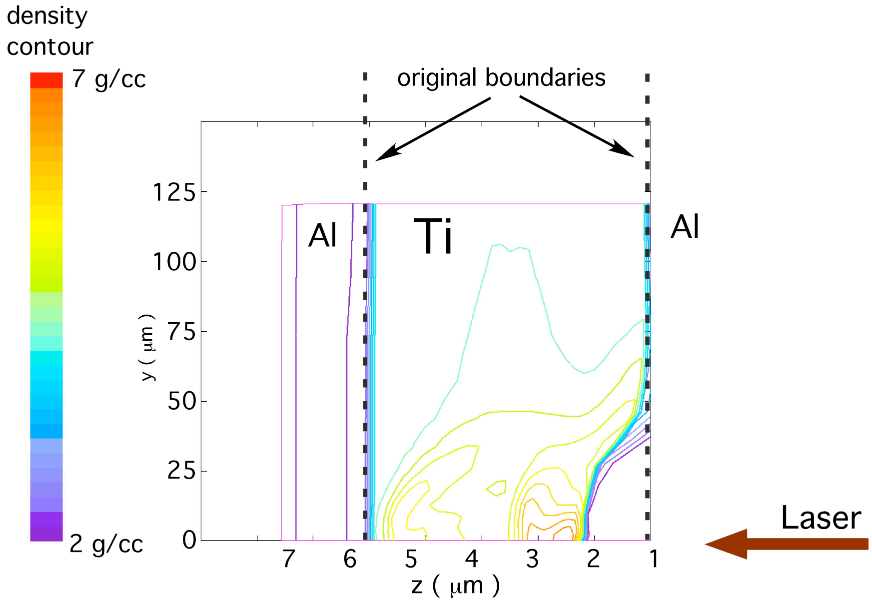

Figure 4.3: Density contours obtained from h2d simulation of the effect of a 0.5 ns long prepulse on the 250 x 250 μm^2 square target tamped with 1 μm Al. The simulation time corresponds to the start of the main laser pulse.

4.3.2 K-alpha Imaging

The K-alpha imager captured spatially resolved 4.5 keV x-rays emitted from the target. The bandwidth of the detector is 2.67 eV which corresponds to K-alpha emitted by a titanium plasma with an average ionization of Z = 0-4 [87]. Therefore, imaging this particular wavelength emission gives hot electron spatial information before significant heating (or ionization) of the target. Fig 4.4 compares the image taken of the 1 x 1 mm^2, 2 μm Al tamper target and 250 x 250 μm^2, 1 μm Al tamper target. The FWHM of intense spot where the laser interacted with the target is 300 μm for the larger target and is 75 μm for the smaller target. Even accounting for a slightly thicker target, the 1 x 1 mm^2 square target has a larger divergence angle than the smaller target. Fig 4.5 compares the two 250 μm^2 targets of different tamper material. The target with the CH tamper has a FWHM of 140 μm.

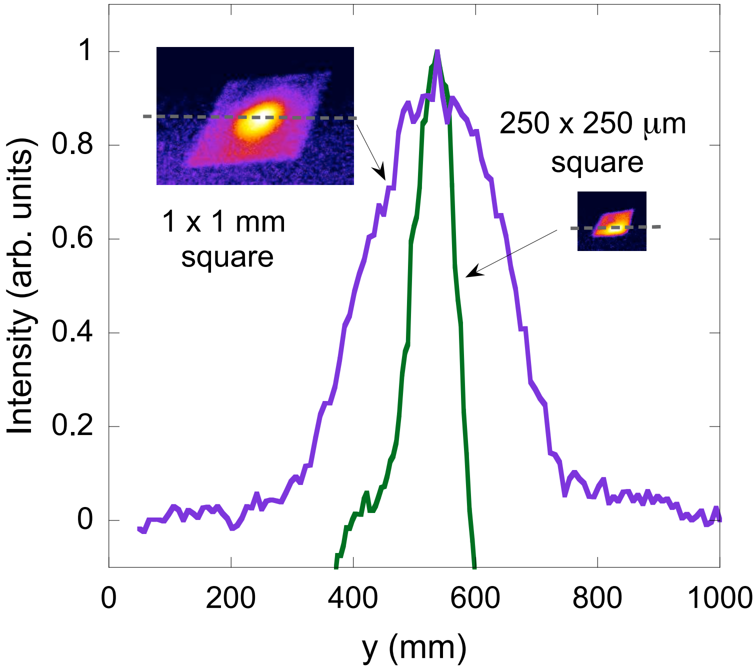

Figure 4.4: Measured spatial distribution of the K-alpha emission from the rear of 250 x 250 μm^2 target with 1 μm Al tamper and 1 x 1 mm^2 with 2 μm Al tamper. The line profiles corresponds to the spatial distribution of the hot spot intensity.

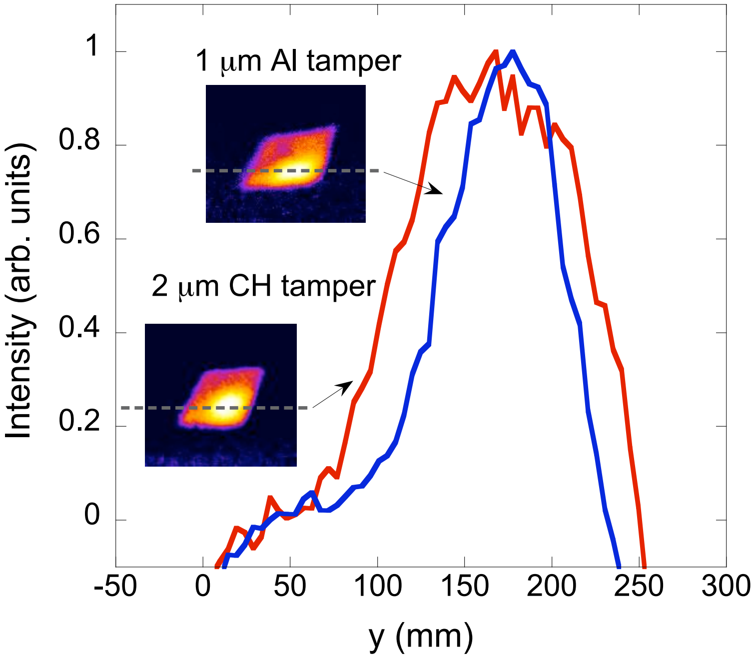

Figure 4.5: Measured spatial distribution of the K-alpha emission from the rear of 250 x 250 μm^2 target with 1 μm Al tamper and 2 μm CH tamper. The line profiles corresponds to the spatial distribution of the hot spot intensity.

It was expected that by using small targets, higher amount of refluxing would occur and therefore show a more uniform spatial distribution of the hot electrons. However, this is not the case and experimentally captured images suggest that heating by hot electrons is non-uniform in the lateral direction regardless of target size or tamper material.

4.3.3 K-Shell Spectroscopy Results

The measured titanium K-shell spectrum from a 250 x 250 μm^2 square target tamped with 1 μm Al is shown in Fig 4.6 and Fig 4.7. Data were background subtracted and corrected for the 5 μm Al filter transmission. Spectral lineouts, averaged over the non-dispersive direction, for both Al and CH tamped cases are shown in Fig 4.7. The absolute position of the cold K-alpha line is then determined by using the He-like line as a reference in conjunction with a marker on the image plate holder (as shown in Fig 4.6). It was estimate the absolute error in the energy position of the K- alpha to be ±2.5 eV. The relative error (error between shots) in position between the lines is estimated from the reference marker to be ±1 eV.

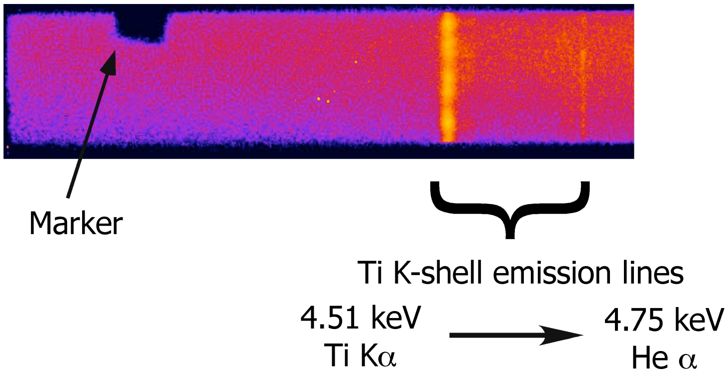

Figure 4.6: Measured signal on the image plate from the 250 x 250 μm^2 square target with 1 μm Al tamper. The reference marker is shown on the left and emission lines on the right.

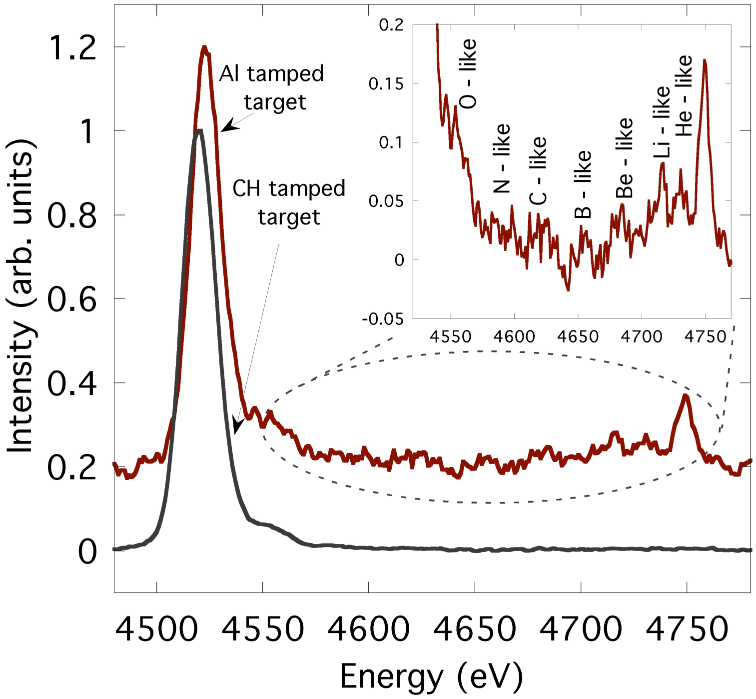

Figure 4.7: Lineout from the exposed image plate of titanium spectra from 4.51 – 4.75 keV of the 1 μm Al tamped target and the 2 μm CH tamped target. Inset shows titanium satellite lines from Oxygen-like to He-like lines.

In high intensity short pulse laser interactions, with intensities higher than 2 x 10^{18} W/cm^2, a large number of relativistic electrons ($N_{hot} > 10^{14}$) are produced [102]. The electron energies can range from few keV to 10's MeV [95]. As the sample increases in temperature, the outer electrons of the titanium atom are progressively stripped and thus increasing the K-shell ionization potential due to a change in the outer shell shielding. The radiation energy of the K-alpha transition emitted from a partially ionized atom is consequentially shifted with respect to that of neutral atom. This change in the x-ray emission has been measured for titanium under the condition of the present experiment, and it is a direct measurement of the ionization state in dense plasmas. Since K-alpha is emitted by the whole target and the measurement is spatially integrated, an average (bulk) value from the most intense line and peak temperature from the highest ionization K-alpha, namely the He-alpha lines can be inferred.

4.4 Effect of target size and tamping material on bulk temperature

Measurements of the cold K-alpha line for the three different types of targets (250 x 250 μm^2 square with 1 μm aluminum tamper, 1 x 1 mm^2 square with 2 μm aluminum tampers, and 250 x 250 μm^2 square with 2 μm CH tampers) were used in the experiment and the wavelength of the cold K-alpha line are shown in Fig 4.8. Smaller shifts in the K-alpha line (~10 eV) was observed when compared to the same line from a large (1 x 1 mm^2) targets. The largest shift of ~16 eV was observed with reduced mass targets (250 x 250 μm^2) and aluminum tampers. However, shifts in K-alpha position were significantly smaller (<10 eV) when a CH tamper was used in reduced mass targets. The collisional radiative code SCRAM [103-104] was used to generate theoretical line-shapes for various bulk electron temperatures and to calculate average ionization state. SCRAM is a collisional radiative model based on hybrid detailed-level and unresolved-transition-array (UTA) data from the FAC code [105]. The model generates rate matrices for a given set of plasma conditions, solves for self-consistent level populations including opacity in the escape factor formalism for a layer of material with fixed thickness, and constructs emission spectra. Two electron populations, one with a bulk thermal temperature of T_e, and the other representing the hot electron temperature T_{hot} = 250 keV with a number density of 1% of the total electron population were used [106]. The code is relatively insensitive to the energy distribution function and the temperature of the hot electrons provided that it is much greater than the ionization energy of the collisional process of interest.

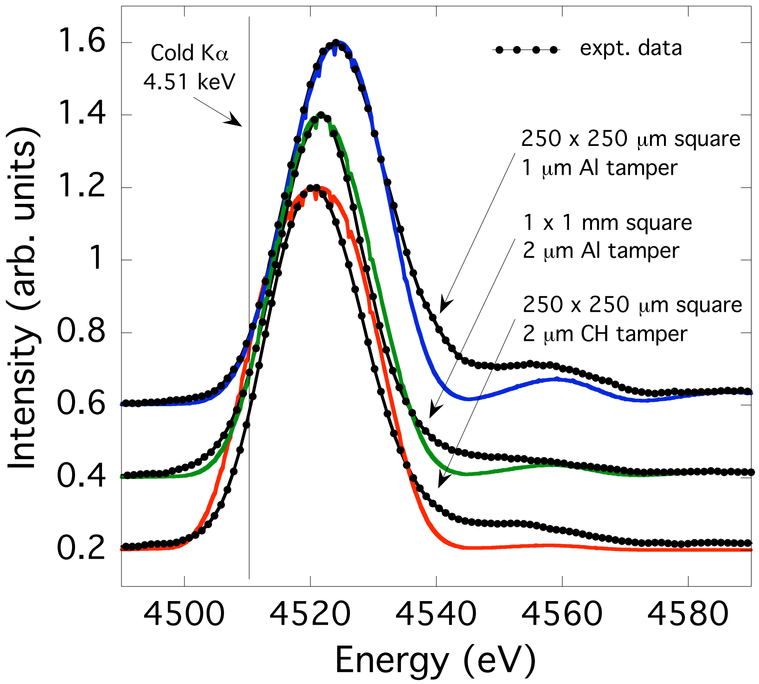

Figure 4.8: Spectral shifts of cold K-alpha measured by the front spectrometer for various types of targets. Solid line is spectral calculation from the collisional radiative code SCRAM.

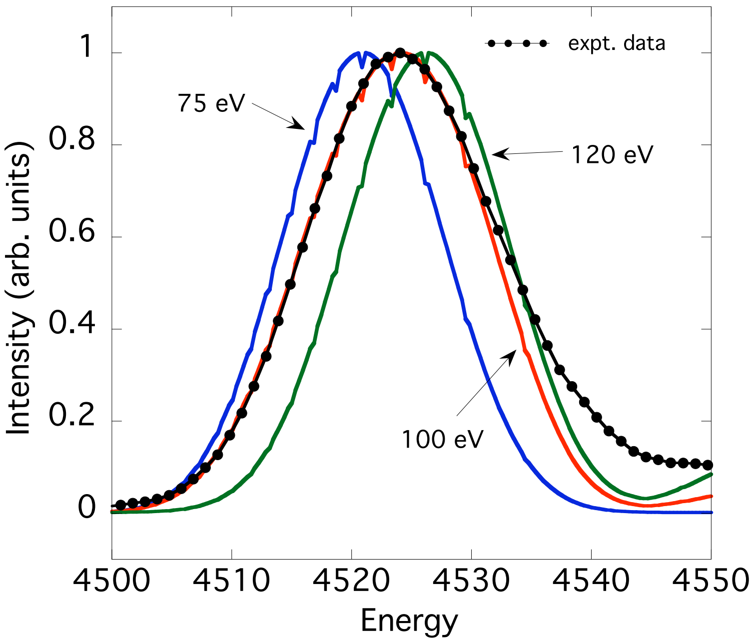

Figure 4.9: Sensitivity analysis showing the effect of ± 2.5 eV error in the absolute energy calibration. The experimental spectrum corresponds to the 250 x 250 μm^2 square target with 1 μm Al tamper. Solid line is spectral calculation from the collisional radiative code SCRAM.

Synthetic spectra generated using the measured instrument response are shown in Fig 4.9. The code was run for various thermal temperatures to produce fits with the experimental data. The results from reduced mass targets with a 1 μm Al tamper, which had the largest shift in K-alpha position, indicated bulk temperatures of ~100 eV. With the larger target, the average bulk temperature slightly decreases to 80 eV, which is expected since the mean energy density should decrease with increasing target size [5]. Analysis shows that the error in the absolute wavelength calibration corresponds to an error in the estimated electron temperature of ±20 eV, as indicated in Fig 4.9. In reduced mass targets, the number of ions is small, ~2 x 10^{15}, and the target is ionized rapidly with a time much smaller than the disassembly time. In contrast to the Al tamped targets, in the case of a CH tamper a significantly lower temperature is observed, of the order of 40 eV.

4.5 Hot Layer Temperature

As shown in Section 4.3.2, the K-alpha image showed a non-uniform spread of hot electrons which it was speculated that heating is localized to a small area several times larger than the laser spot. Also, our spectral measurements show the presence of a significant emission of radiation from highly stripped ions for the case of aluminum tamped targets but not for CH tamped ones (see Fig 4.7). This suggests the presence of a hot ($T_e > 800$ eV) region in the aluminum tamped targets. The intensity ratio between the He–like resonance and the intercombination lines, and the lithium-like satellite is very sensitive to temperature, density and optical thickness of the plasma of interest [107]. The calculated spectra for a range of temperatures, densities, and thicknesses between 0.1 μm to 5 μm was performed with the SCRAM code to extract temperature estimates for the hot plasma region. The best fit for the data from the low-mass target with 1 μm aluminum tamper was obtained with a 0.2 μm thick heated layer of solid titanium at $T_e \sim 1300$ eV as shown in Fig 4.10. Slightly lower hot spot temperatures are obtained with the 1 mm square and 2 μm aluminum tamper. These temperatures are consistent with previous observations of hot layers in short-pulse high-intensity laser plasma interaction with copper planar foils [42]. The temperature error is estimated from Fig 4.11 to be ±300 eV. Targets tamped with 2 μm CH did not show any evidence of Ti He-alpha emission, giving an estimated upper limit on T_e of ~ 500 eV. Thus, both the 'hot spot' and bulk temperatures are reduced by at least a factor of two for CH tampers compared with Al tampers of the same mass. This is presumably due to the difference in hot electron transport in these two materials, namely a difference in resistive effects.

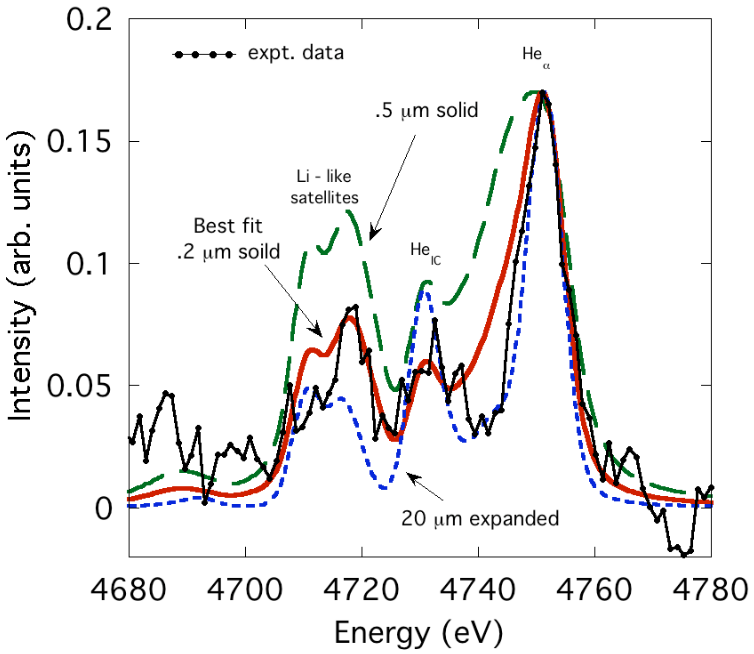

Figure 4.10: The experimental spectrum for the 250 x 250 μm^2 square target with 1 μm Al tamper is compared with SCRAM calculations: (solid red line) best fit assuming Ti at solid density, T_e=1.3 keV in 0.2 μm hot layer; (dotted blue line) simulation assuming the 0.2 μm layer expanded to a density 100 times lower than solid; (dashed green line) simulation assuming a layer thickness of 0.5 μm, The calculated spectra have been convolved with the experimental instrument response.

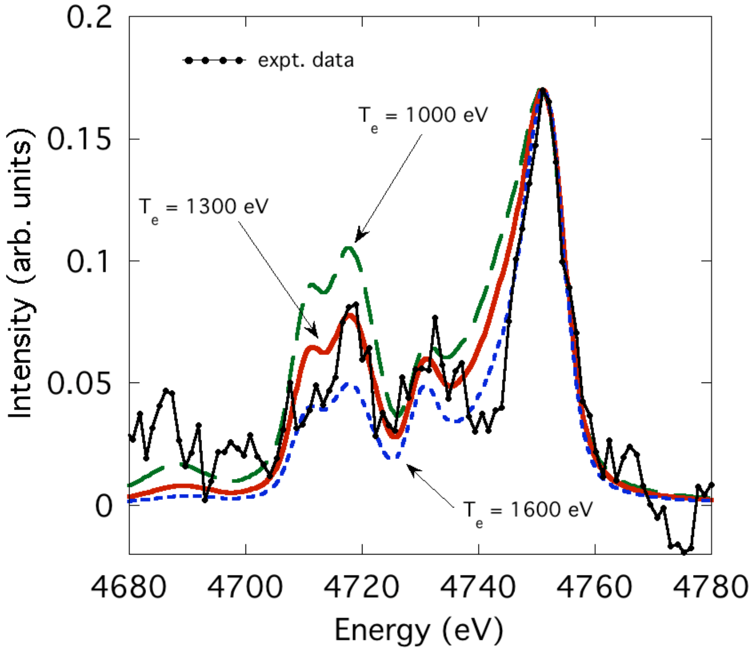

Figure 4.11: Sensitivity analysis showing the differences in line intensity of 0.2 μm thick, solid-density Ti at three different temperatures.

4.6 Discussion

The data suggests significant temperature differences between the Al tampered target and CH tampered target. The physics governing transport through this region is extremely complex. There exist several explanations of electron transport through metals and insulators [108-109]. Particularly, Krasheninnikov *et al.* [108] have discussed in detail growth of electron beam instabilities in insulator targets. One likely explanation for large differences in peak and bulk temperatures has to do with the differences in nuclear charge between Al and CH samples. Low current beams of relativistic electrons lose energy due to interaction with bound and free electrons in the solid and also scatter in angle, predominantly due to screened Coulomb collisions with nuclei of charge Z_A. High-current beams behave very differently because their self generated electric and magnetic fields that can dominate the transport and energy loss. These high current beams that exceed the Alfvén current and must be compensated by a return current in the background thermal plasma. The combination of forward and return currents is unstable to a variety of plasma modes, often referred to as Weibel instabilities [110]. All of these beam instabilities are associated with the beam electrons and have characteristic growth rates on the order of the plasma frequency of the beam species [111].

The PIC simulations and most of the analytic calculations do not include the effect of angular scattering of the beam electrons by the background plasma. At solid densities this scattering rate can be appreciable and increases strongly with nuclear charge Z_A. Davies *et. al.* [112] in their consideration of the transport of high current relativistic electron beams show that an electron beam initially with no transverse velocity will acquire a transverse temperature. In particular, they have shown that the average mean square angular scatter can be expressed as,

$$\langle \Delta\theta^2 \rangle = \left(\frac{Z_A^2 n e^4}{2\pi\varepsilon_o^2} \frac{\gamma m}{p^3} ln\, \Lambda \right) t = v_\perp\, t \tag{4.1}$$

where n and m are the number density and mass of the electrons in the background plasma, respectively and the Lorentz factor is γ and p is the relativistic momentum. Eq. 4.1 is valid for $\Delta\theta << 1$ and it shows that an electron beam initially with no transverse velocity spread will acquire a transverse temperature, that in moderate Z_A plasmas increases approximately linearly with time since the angular scattering is faster than the slowing down of the beam. If the initial electron beam is relativistic and $\beta_\perp$ is the transverse velocity normalized to the speed of light then,

$$\beta_\perp^2 = \langle \Delta\theta^2 \rangle \tag{4.2}$$

Silva et al. [113] have shown that transverse filamentation instability is stabilized by a relatively small transverse temperature in the electron beam. They calculated that for a beam with a longitudinal velocity β_{II}c, the threshold for filamentation instability is

$$\alpha > \gamma \frac{\beta_\perp^2}{\beta_{II}^2} \tag{4.3}$$

where α is the ratio of the density of the beam electrons to the the density of the background electrons. As discussed previously, for the laser irradiance considered here, α ~10-2 (see also Evans [114]).

The importance of the angular scattering is that in moderate Z_A materials it is large enough that within one growth time for the filamentation instability that the electron beam can acquire, through collisions, a transverse temperature that is large enough to stabilize the filamentation. The parameter describing the competition between the two effects is $\gamma_f/v_\perp$ where γ_f the instability growth rate is of order ω_{pb} the plasma frequency for the beam electrons. This is the number of instability growth times before the transverse velocity spread is large enough to stabilize the instability. Taking a beam of 1 MeV electrons we then find $\gamma_f/v_\perp = 14$ for CH and $\gamma_f/v_\perp = 0.5$ for Al. Thus, in CH tamped targets the filamentation instability can grow as seen in the PIC simulations [112], whereas in Al and higher Z_A tamped targets the growth in transverse beam temperature due to scattering stabilizes the filamentation and the stopping is only dependent on the classical collisions and the electric field.

4.7 Summary

A method in using K-shell spectroscopy to diagnose a keV plasma produced by a high intensity short pulse laser has been explored. Using low mass targets with thin 1 μm aluminum tampers, a 100 eV average bulk temperature and peak temperature of 1300 eV at solid density can be reached. Average ionization state of the solid titanium layer is directly measured by the shifts of K-alpha radiation, and bulk temperature inferred from a collisional radiative code. The measurements also indicate significant emission of radiation from highly ionized ions at solid density, suggesting the presence of a hot region, which implies an anomalous stopping in the surface layer.

The hot electron beam traversing through tamping material, with a higher Z such as Al, will scattering with a larger angle than traversing through lower Z materials such as CH. In the Al tamped target, the electron beam can gain a transverse temperature that can stabilized any filamentation, thus permitting the propagation of the hot electron beam in the forward direction. With a CH tamper, any unsuppressed filamentation diffuses the heating ability of the electron beam. This is clearly seen in a significantly lower measured peak and bulk temperature with the CH tamped target. Also, this is corroborated by the data from the K-alpha imager showed that the spot size from the CH tamped target, is larger than the Al tamped target by a factor of two.

4.8 Acknowledgement

Portions of Chapter 4, is a reprint of the material as it appears in: S. N. Chen, G. Gregori, P. K. Patel, H. K. Chung, R. G. Evans, R. R. Freeman, E. G. Saiz, S. H. Glenzer, S. B. Hansen, F. Y. Khattak, J. A. King, A. J. Mackinnon, M. M. Notley, J. R. Pasley, D. Riley, R. B. Stephens, R. L. Weber, S. C. Wilks and F. N. Beg, "Creation of hot dense matter in short-pulse laser-plasma interaction with tamped titanium foils", Physics of Plasmas **14**, 6 (2007). The dissertation author was the primary investigator and author of this paper.

Chapter 5

Plasma characteristics of buried copper irradiated at 10^{20} W/cm^2

This second experiment is an extension of the previous experiment at the Vulcan Laser Facility where temperature gradients in the transverse and longitudinal directions were found even in small targets. For this experiment, target transverse size was reduced further and the fluorescence layer thickness was significantly reduced to minimize the effects of opacity. The recorded K-shell spectra from the interaction was modeled by an atomic code. Furthermore, spectral changes due to hot electrons and opacity were investigated using the atomic code. Finally, time dependence on the emission was studied using a hydrodynamics code coupled with the atomic code.

5.1 Introduction

In this chapter, observations of a rapid decrease in thermal temperature as a function of depth of solid targets irradiated with a short-pulse, ultrahigh-intensity laser will be presented. This phenomenon is investigated using the Titan short pulse laser with intensities greater than 10^{20} W/cm^2 interacting with buried layer targets. The longitudinal temperature profile is determined by measuring K-shell spectra from a 0.4 μm copper tracer layer placed at various depths (i.e. 0-1.5 μm) within the 2.4 μm thick target. It is observed that the line ratios (He like K-shell lines) as a function of temperature require a consideration of at least three parameters to analyze the K-shell spectra: hot electron population, time dependent plasma conditions, and opacity. Here, the study of the effect of these three parameters on measured spectra using the atomic model FLYCHK is presented.

5.2 Experimental Setup

The experiment was carried out on the Titan Laser at the Jupiter Laser Facility at Lawrence Livermore National Laboratory. Targets used in the experiment were 100 x 100 μm^2 squares with a total thickness of 2.4 μm. The targets were composed of a 0.4 μm layer of copper sandwiched between a layer of silver on the front and aluminum on the back. The position of the copper layer was systematically varied in depth from 0-1.5 μm (see Fig. 5.1) by increasing the thickness of silver layer. The layered targets were created by sputtering the metal onto a soap covered glass slide. Then squares laser cut by Resonetics and released from the glass slide using water.

The targets were mounted onto a 15 μm carbon fiber and aligned to 30 degrees from the laser axis. The silver side of the target was irradiated by the chirped pulse amplified (CPA) arm of the Titan laser delivering 140 J of 1.053 μm s-polarized light in 500 fs. The beam was focused down to a 10 μm diameter spot by a f/3 off-axis parabola to give a peak focused intensity of 3 x 10^{20} W/cm^2. The pre-pulse was measured to be a 2 ns pedestal at approximately 10^{13} W/cm^2 using a fast photodiode.

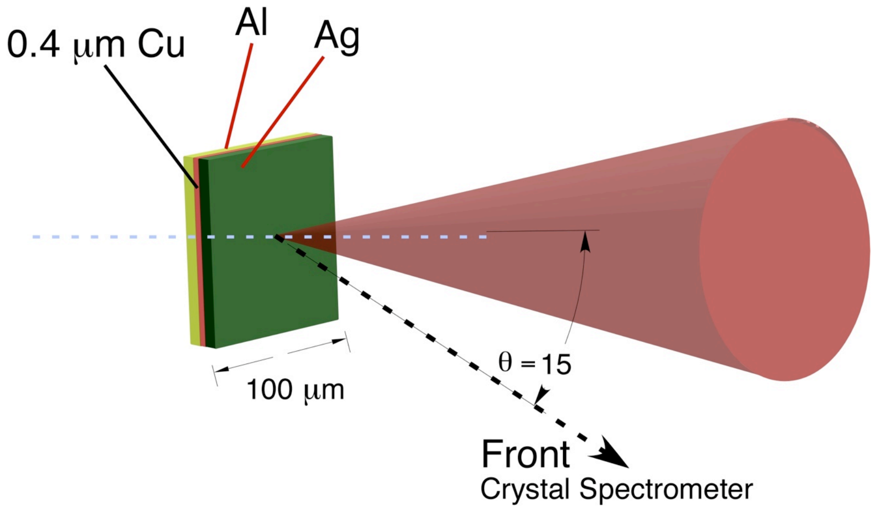

Figure 5.1: The diagram shows the configuration of the buried layer target. The silver side of the target was irradiated with the short pulse laser. The HOPG spectrometer viewed the interaction from the front side.

Copper K-shell spectra were measured with a Highly Oriented Pyrolytic Graphite (HOPG) crystal spectrometer and recorded on a FujiFilm MS image plate. The HOPG spectrometer captured x-rays between 8 keV and 12 keV and viewing angle to target normal was 66 degrees. The spectral resolution of the HOPG spectrometer was measured to be $E/\Delta E = 200$.

5.3 Pre-Pulse simulations

Simulations using the hydrodynamics code HYADES was performed to estimate effects of the measured pre-pulse on a buried layer target. The HYADES code [115] is a one dimensional radiation and Lagrangian hydrodynamics code. A flux limiter of 0.05 was employed to the electron conduction term for 1ω illumination. Multi-group diffusion using 50 frequency groups ranging from 10 eV - 20 keV was used and the ionization model used was the average ion model in LTE. Laser for pre-pulse was absorbed by 90% inverse bremsstrahlung and 10% by resonance absorption. The SESAME [101] equation of state tables were used and opacities were generated from an in-line average-atom atomic physics package model which assumes LTE.

The code was run in planar geometry and the target specifications was 1 μm Ag on the front, 0.4 μm of Cu, and 1 μm of Al on the back side. Using the experimental pre-pulse duration of 2 ns with a boxcar temporal profile, and energy level of 20 mJ as a reference point, two other simulations were also performed using laser energies of 5 mJ and 100 mJ. From the simulation results of the density profile of the target at 2 ns, as shown in Fig 5.2, it was verified that 1 μm of Ag was sufficient to keep the copper layer at or above solid density at the end of the pre-pulse with energy less than 100 mJ. HYADES simulations were also done with the layered target with 0.5 μm Ag on the front, 0.4 μm of Cu, and 1.5 μm of Al on the back side (see Fig 5.3). Laser conditions were identical to the previous set of simulations. With a 5 mJ pre-pulse, the result at 2 ns has the copper layer remaining at or above solid density. However, with laser energy above 20 mJ, it is evident that 0.5 μm of Ag was not enough to prevent the copper layer at solid density.

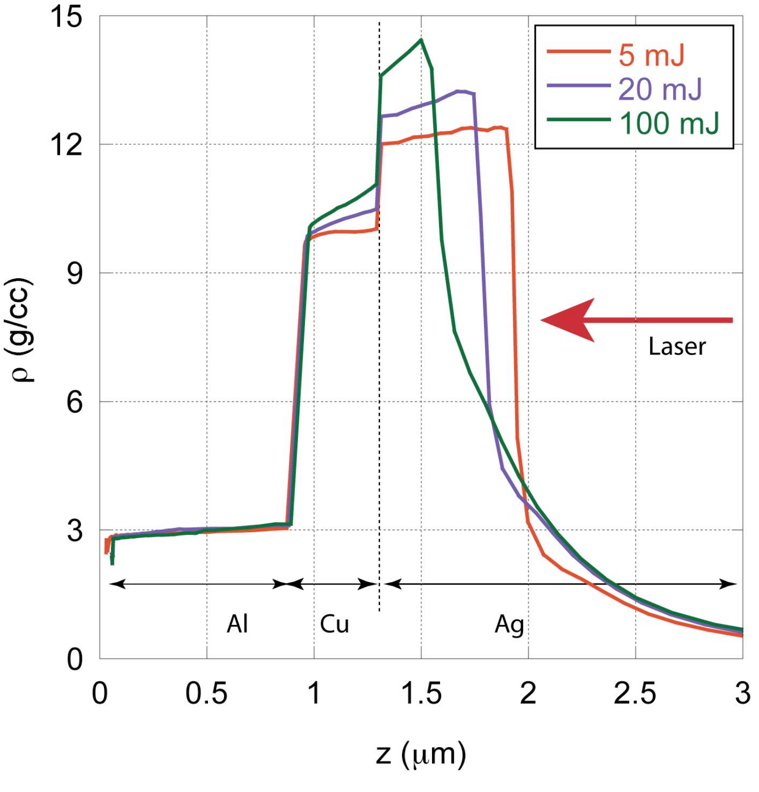

Figure 5.2: HYADES simulation results of a target 1 μm Ag, 0.4 μm Cu, and 1 μm Al irradiated with a 2 ns pulse at 5 mJ, 20 mJ, and 100 mJ.

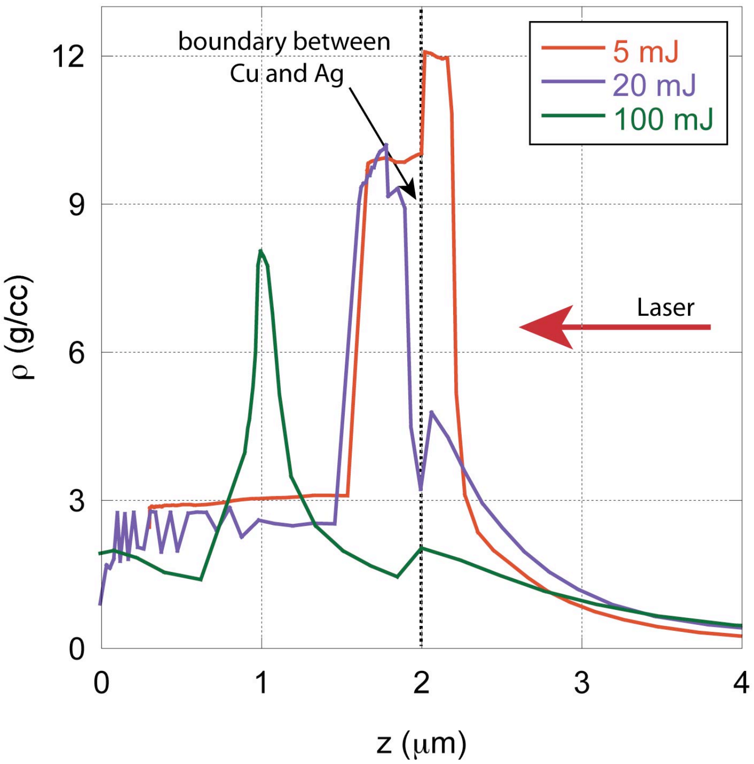

Figure 5.3: HYADES simulation results of a target 0.5 μm Ag, 0.4 μm Cu, and 1.5 μm Al irradiated with a 2 ns pulse at 5 mJ, 20 mJ, and 100 mJ.

5.3 Experimental Results

Figure 5.4 and Fig 5.5 shows the measured copper K-shell spectra from the targets with a copper buried layer at the depth of 0, 0.5, 0.75, 1.0 and 1.5 μm. With no silver layer in front (silver curve), the peak near neutral K-alpha (8.047 keV) is broadened and slightly shifted due to K-alpha from various ionization states present in the plasma. Individual K-alpha lines from O-like to He-like ions can be clearly identified.

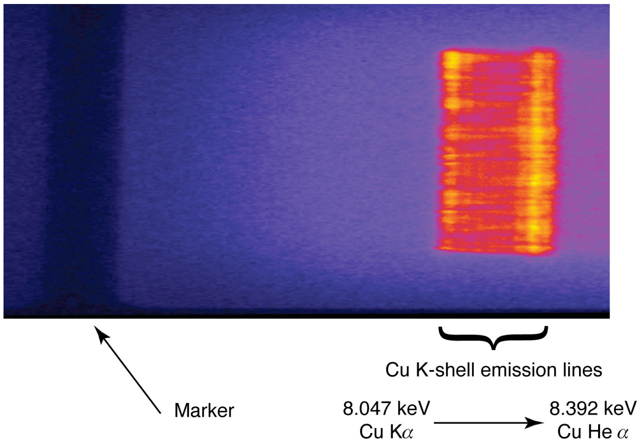

Figure 5.4: Measured signal on the image plate from a 100 x 100 μm^2 square target with copper buried at 0.75 μm. The reference marker is shown on the left and emission lines on the right.

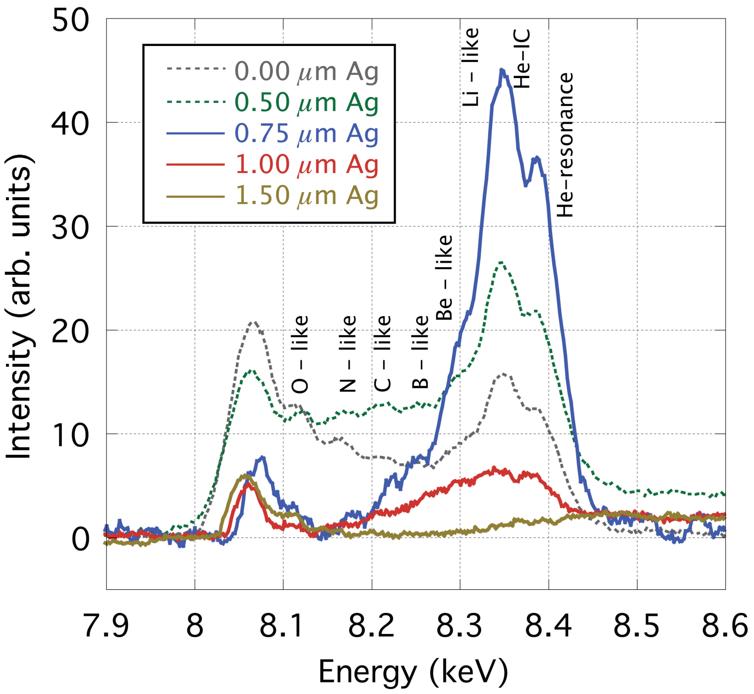

Figure 5.5: Lineouts taken from exposed image plate of copper spectra from the series of five targets. Spectra are identified by the thickness of the silver layer to reflect the location of the 0.4 μm copper fluorescence layer in the target. The silver layer was varied to understand the extent of longitudinal non-uniformity of temperature.

The two dominant features between 8.3 keV and 8.4 keV consist of He-like resonance ($^1S_0$ - $^1P_1$ 8.392 keV), intercombination ($^1S_0$ - $^3P_1$ 8.347 keV) lines as well as several Li-like satellites. The dispersion relating the physical position of the line on the image plate to its corresponding wavelength has an accuracy of ± 10 eV. Two progressions in the five spectra can be followed, the K-alpha line near 8.047 keV and the lines around He-alpha. Starting from the spectra from the target with no Ag tamper, the copper is exposed to the laser and is ablated by the prepulse.

The cold K-alpha is quite intense and lines from ionization stages up to He-like are observed. Next with a 0.5 μm Ag tamper, the pre-pulse presumably has released some copper into the plume. Nonetheless, the dominant lines start to shift from lower ionization states to higher ionization states. With a 0.75 μm tamper, the 1-D HYADES radiation hydrodynamics simulations of the pre-pulse indicate that it is likely that the the copper layer stays intact. The cold K-alpha drops further, a factor of 3 from the case with no tamper. Then, as the copper layer moves from 0.75 - 1 μm in depth, the intensity of the He-alpha drops by a factor of seven and there is a constant amount of cold K-alpha. Furthermore, at 1.5 μm, there is no measurable He-alpha emission. The progression of He-alpha as the copper moves from 0.75 to 1.5 μm is consistent with previous observations of a temperature gradient along the laser axis inside a solid target. [42-44] Another feature worth noting is the ratio between the He-like resonance and peak on the lower energy side, it is constant in the cases with no tamper to 0.75 μm of silver, presumably indicating that the plasma emitting these lines is under similar conditions.

5.4 Atomic Modeling and Discussion

The measured spectra contains lines from ionization states from a neutral to He-like atom as shown in Fig 5.5. Therefore, the spectrum cannot be modeled using a single temperature and density. There are two discrete clusters of lines in the spectra from the copper layer buried 0.75 μm in the target, that is, the one 8.047 keV and the other 8.4 keV. It is safe to assume that the plasma conditions that produced those lines are vastly different and therefore, can be modeled separately. Modeling of the cold cluster around 8.047 keV is fairly straightforward as it is only produced in the presence of hot electrons. Temperature of the plasma that produces these lines can be found by following the techniques of modeling shifted K-alpha outlined in the by Gregori *et. al.* [33]. Modeling of the cluster around 8.4 keV, which is comprised of Beryllium to Helium – like lines is more difficult as it can be produced by a thermal plasma, induced by hot electrons or a combination of both.

In the following analysis, the measured He-alpha data from the copper fluorescence layer fluorescenceburied at 0.75 μm is used and is first compared with calculated spectra of a 0.4 μm thick copper plasma specified by a single density and thermal temperature. Then, the effect of a presence of hot electrons in the collisional radiative calculation is studied. Finally, temporal behavior is considered by performing simulations with an expanding, cooling plasma and integrating emission over time.

5.4.1 The collisional radiative code FLYCHK

FLYCHK [116] is a collisional radiative atomic code, based on the FLY code [117], that was created to be fast and simple to use. Its primary function is to calculate average ionization and radiative properties for a given plasma temperature and density. The code can accommodate a variety of different plasma situations such as coronal, LTE, non-LTE in steady state or time dependent. Unique to this atomic code is that multiple electron distributions can be used as well as mixture plasmas and external energy sources can be applied. Detailed population distributions are obtained by solving multi-level rate equations with collisional and radiative processes. For K-shell spectroscopy, the original FLY and HULLAC [118] atomic data is used for Li-like, He-like, and H-like ions.

FLYCHK uses atomic levels that are represented by their principal quantum number, also referred to as the superconfiguration scheme [118]. Ground state energy levels are computed from ionization potentials from both empirical and calculated data [119-120]; and excited levels of the outermost bound electron is calculated using a hydrogenic approximation with relativistic corrections. Autoionizing inner-shell excited levels are also included in the hydrogenic approximation.

The atomic transition rates are based on previously published analytic descriptions which allow much faster computations, but sacrificing some accuracy. The collisional excitation cross-sections and inner-shell excitation processes are based on oscillator strength for the allowed transitions [121]. Also, the semi-empirical formula of Burgess and Chidichimo [122] is used for collisional ionization. The absorption oscillator strength and photoionization cross-sections are computed for hydrogenic levels by using Hartree–Fock–Slater wave functions [124-125]. Autoionization rates are calculated by perturbation theory in the Dirac– Hartree–Slater approach [126-127]. Dielectronic recombination processes are included via electron capture processes, whose rates are determined by detailed balance with autoionization rates.

5.4.2 K-shell spectra modeling

The following calculations assumed the plasma is non-LTE and in steady state. Plasma temperature and density is user specified with the option of adding a second electron distribution. Then, intensity of emission lines is found using the classical transfer equation and finally, the experimental instrumental function is imposed onto the calculated spectra.

In order to determine the best fit, the line ratio of the He-like resonance line to the next peak at 8.35 keV, is used. With mass density assumed at solid, n_e = 8.89 g/cc, thickness of 0.4 μm, the inferred temperature of the plasma is about 2100 eV as shown in Fig 5.6. This is consistent with earlier studies [42]. Additional simulations also showed that the best agreement between experimental data and modeling was with setting the density of the emitting plasma at or greater than solid.

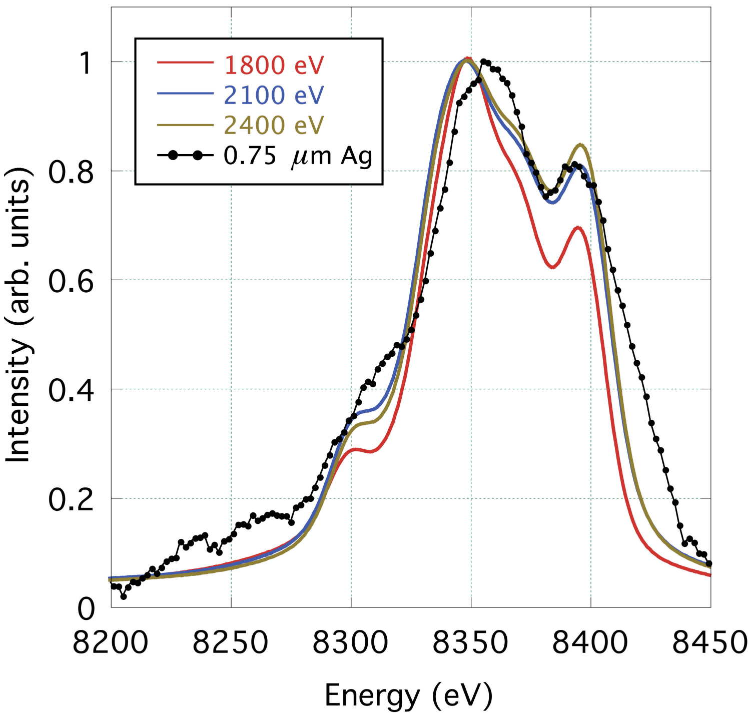

Figure 5.6: Sensitivity analysis showing the effect of ± 300 eV variation in thermal temperature has on the spectra. The experimental spectrum corresponds to the target with copper buried at 0.75 μm from the surface.

5.4.2 Effect of Hot Electron Population

A second electron population was added to the model to simulate the effects of a hot electron population on the thermal plasma. The temperature of the hot electrons is estimated using *Beg scaling* [73], which is commonly used to estimate hot electron temperature for a given laser intensity and wavelength. The laser intensity used was 3×10^{20} W/cm^2 and 1.054 μm light, the scaling would predict $T_{hot} \sim 1$ MeV. This temperature is also confirmed experimentally by Macphee et al. [106] with similar laser parameters. This also agrees well with the Haines's analytical model [74]. The hot electron distribution is described as a second Maxwellian distribution in FLYCHK, however, the shape of distribution has been shown by Hansen et. al. [51] to have minimal impact on spectra. This leaves hot electron number to potentially affect the production of K-shell lines.

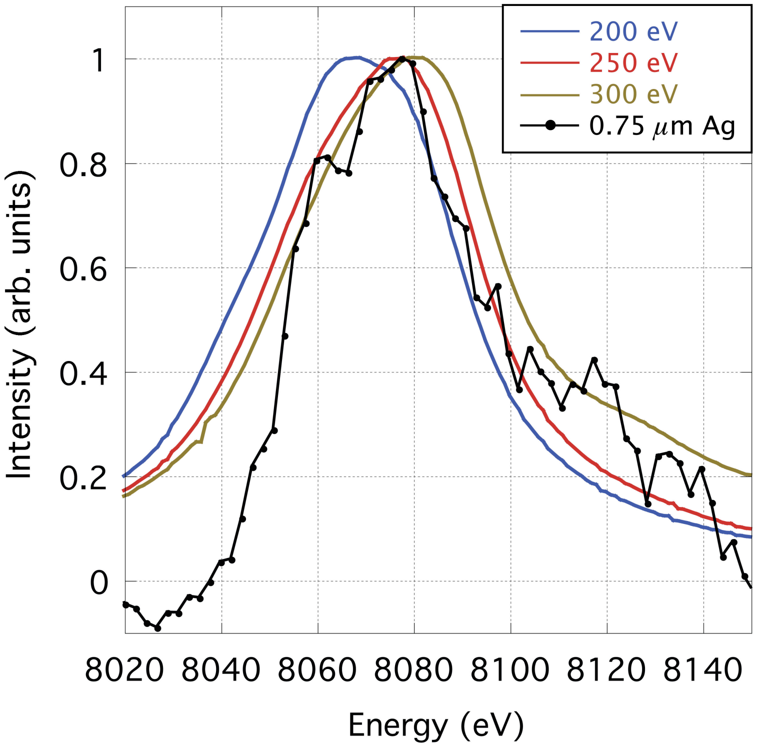

Figure 5.7: Sensitivity analysis showing the effect of ± 50 eV variation in thermal temperature has on the "Cold" K-alpha line. The experimental spectrum corresponds to the target with copper buried at 0.75 μm from the surface.

The presence of the cold K-alpha line indicates the existence of hot electrons inside the target and the shifting of the line has been used to determine background electron temperature [43]. The analysis of the cold K-alpha line is straight forward as it is only produced by the hot electron population. Using a non-perturbative fraction of hot electrons and density at solid, the shifting of the cold K-alpha line was modeled with FLYCHK as shown in Fig 5.7. This provides a lower estimate of the plasma of 250 eV.

A set of preliminary simulations was performed to study the effect of hot electron fraction, $f = n_{hot}/n_e$, on a 800 eV thermal plasma with solid density for the analysis of the He-like lines. The hot electron fraction was varied from 0-10% and its effect on the He-alpha line emission is illustrated in Fig 5.8. A copper plasma with temperature of 1 keV has average ionization reaching the Li-like and He-like states.

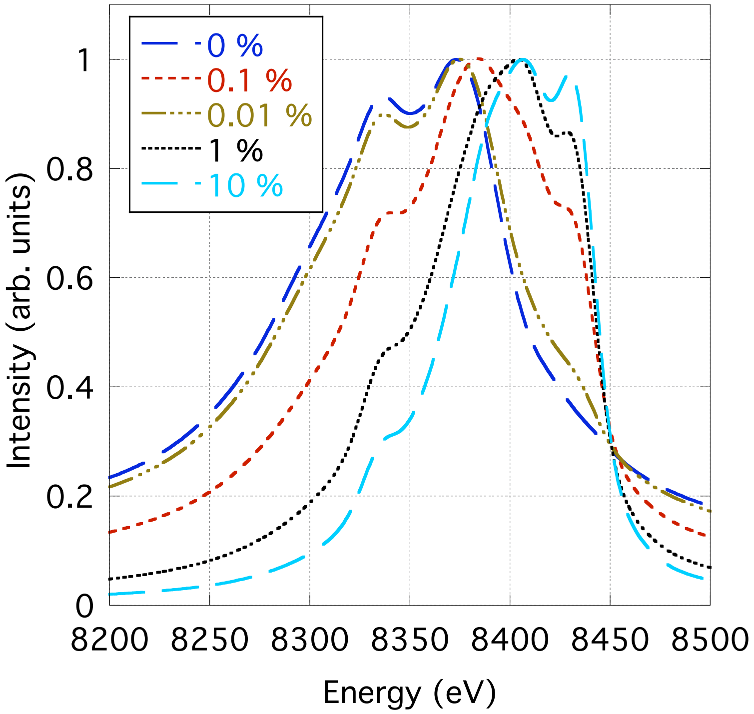

Figure 5.8: A series of curves shows how the specific fraction of hot electrons affects the He-alpha lines in a 1 keV, solid density plasma.

The addition of highly energetic electrons increases excitation and ionization rates and pushes the ionization balance to higher ionization states. In this example this shifts more of the emission from Li-like to He-like ion stages. At a hot electron fraction of 0.01% the effect is rather negligible, but by 0.1% the emission profile is already significantly modified. As shown from these simulations, it can be concluded that the hot electrons cannot be ignored in the collisional-radiative calculation.

The fact that the specific hot electron fraction has the ability to change line ratios in the K-shell spectra considerably complicates the modeling of the measured data. Therefore, a series of simulations were performed to determine a thermal temperature and a hot electron fraction that would produce a best fit to the data. It should also be noted that hot electron fractions above 1% will effectively alter the average ionization state of the plasma. Therefore, only small perturbation ($f < 0.01$) of hot electrons are considered here in this study. The result of this set of simulations is shown in Fig 5.9. The upper bound for the hot electron fraction was set at 1% where a thermal temperature of 1000 eV would produce the desired He-alpha line ratios. The lower bound is the case with no hot electrons as discussed in the previous section. Thermal temperature range from 1 - 2 keV, for a given hot electron fraction and hence it shows an uncertainty in temperature determination by a factor of two when considering a reasonable range of hot electron distributions in the spectral calculation.

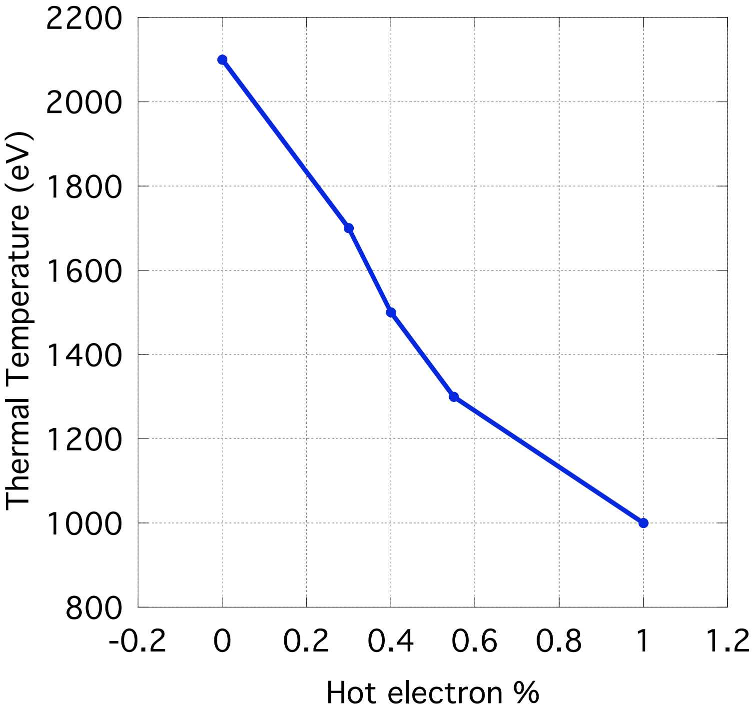

Figure 5.9: This curve illustrates the relationship between hot electron fraction and thermal temperature that would produce a best fit to the experimentally measured He-like lines.

5.4.3 Effect of Opacity

The He-like resonance line is optically thick and subject to absorption before escaping the plasma. Opacity has a two-fold effect on generating spectra, attenuation of observed radiation intensity and self-absorption of photons, which leads to an increase in excited states. Therefore, in modeling optically thick lines, the size of the plasma in the calculation of optical depth, cannot be ignored in the spectral calculation.

In the single-zone atomic code FLYCHK, self-absorption is described by the escape factor included in the population distribution calculation as well as spectral calculations. The escape factor formulism is an approximate way of accounting for reabsorption of photons in a uniform plasma of a finite size by reducing the spontaneous decay rate in the population distribution calculation. Several simulations were performed to illustrate the effect of length in a copper plasma, with thermal temperatures at 2.1 keV and density at solid with thicknesses of 0.4 and 0.04 μm. Opacity, being a function of lower state populations, is largely undisturbed by self-absorption. On the other hand, emissivity is affected by the increase of upper state population by the self-absorption.

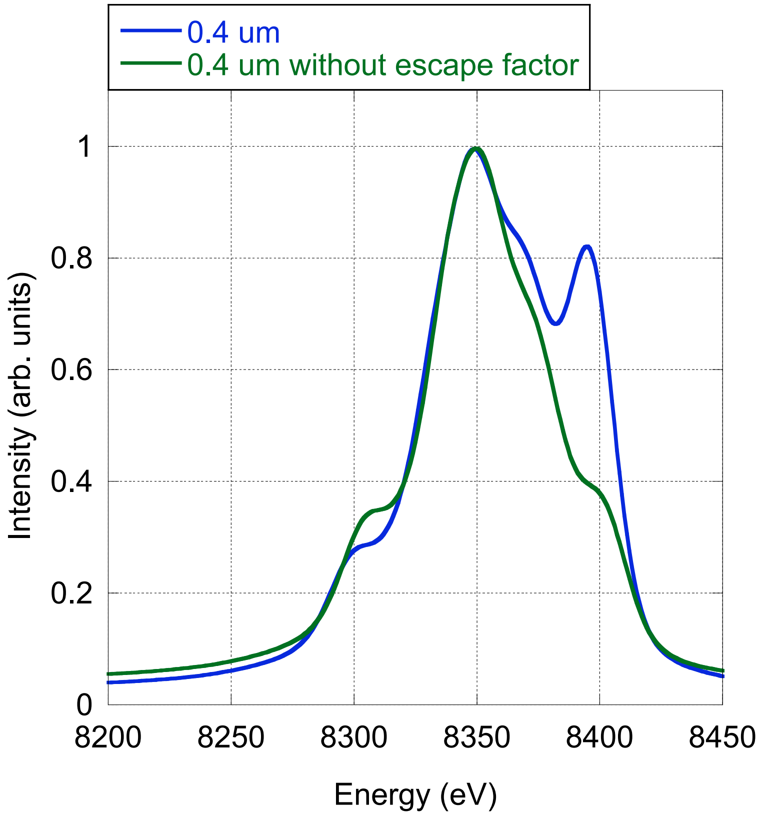

Figure 5.10: A comparison where the escape factor treatment in the code FLYCHK is turned “off.”

Accordingly, as shown in Fig 5.10, the resulting spectra without the escape factor formulism has significantly different line ratios than the simulation with the self absorption treatment. Since the escape factor used in the spectral calculation has dependence on length, the size of the plasma becomes an additional variable in the calculation of spectra. With the escape factor formulism in place, the effect of plasma size is shown in Fig 5.11. The spectra from the thinner plasma has a more intense resonance line compared to the He-like intercombination and Li-like K-alpha lines. Consequently, for a thinner plasma, a lower thermal temperature in the simulation can be used to produce He-alpha satellite line ratios similar to experimentally collected data.

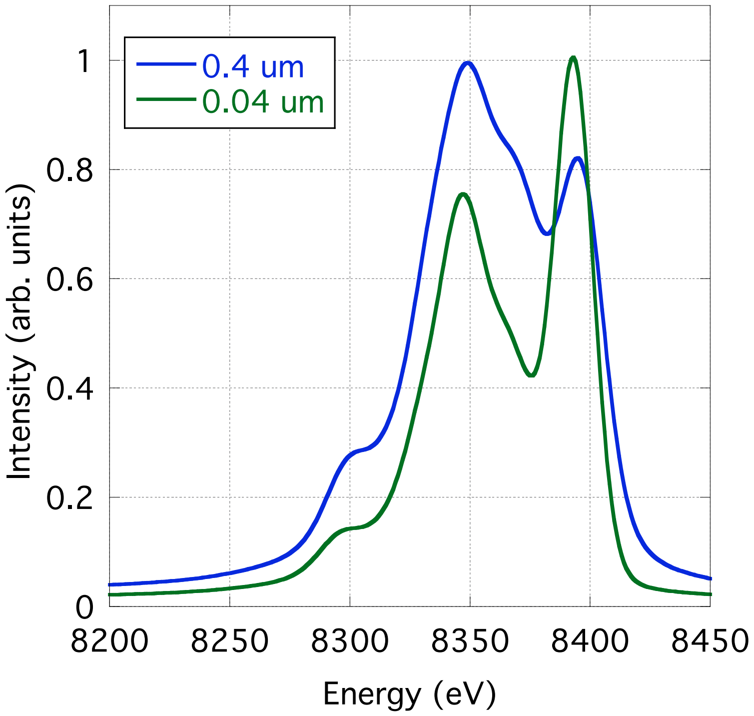

Figure 5.11: A comparison the effect of differing thicknesses of plasma, 0.4 and 0.04 μm with the escape factor formulism.

For multiple zone representations of optically thick plasmas, such as those commonly used in hydrodynamic codes, a different problem arises. Population kinetics codes are typically used as a post processor where emissivitiy and opacity are calculated for an individual zone. A ray tracing technique is then used to add emissivity and opacity along the line of sight and calculate the observed intensity at the plasma boundary. When a 0-d code such as FLYCHK is used, then emission and absorption of radiation field between zones are not accounted for in the collisional-radiative rate equations. This approximation is only valid if the absorption primarily takes place in the same zone, and that adjacent zones are optically thin.

With a multi zone problem, radiation from each zone needs to be transported to the boundary of the target which is represented by the first term. For example, emission from the first zone at the back of the target needs to be transported through *N-1* plasma zones of differing materials and temperatures. The last zone in the front of the target will not needed to be transported through any plasma, so for that particular zone, the first term is zero. The resulting discrete transfer equation of Eq 2.73 is represented as,

$$I_\nu = \sum_{i=1}^{N-1} S_{\nu,i}(1 - e^{\Delta\tau_i})e^{\sum_{j=1}^{N-i}\Delta\tau_j} + S_{\nu,N}(1 - e^{\Delta\tau_N}) \tag{5.1}$$

where N is the total number of zones used to represent the plasma, S_ν is the source function as a function of frequency, τ is optical depth, and I_ν is the intensity of the radiation, as a function of frequency, traveling through the plasma.

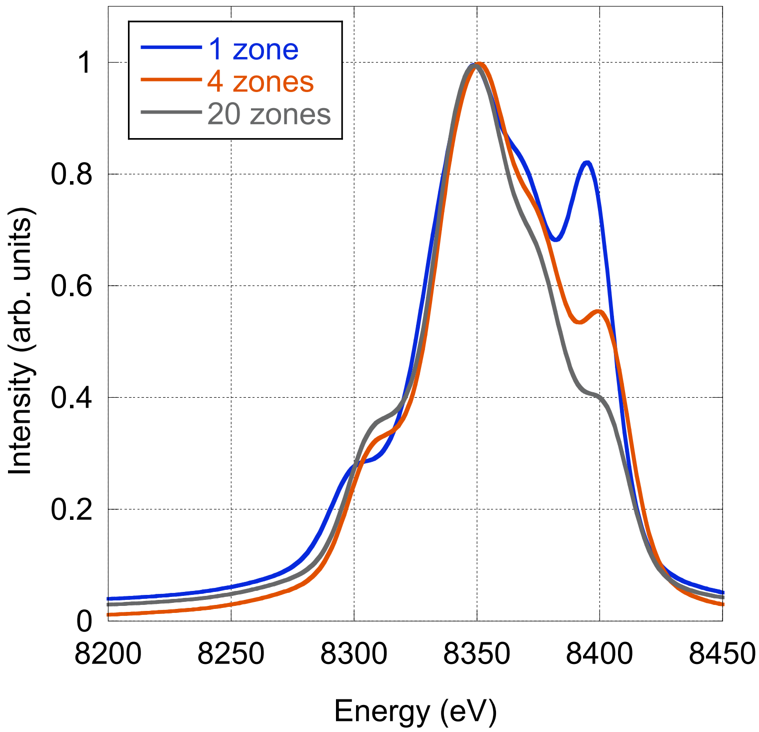

Figure 5.12: Simulations were performed using a multiple zone representation of a finite size plasma and performing ray-tracing to bring the radiation emitted to the surface. Every zone has a thermal temperature of 2100 eV at solid density. For an optically thick plasma, using several smaller zones will decrease the amount of self absorption without zone coupling resulting erroneously the optically thin spectra.

Fig 5.12 shows how the number of zones used to represent a 0.4 μm thick copper plasma at 2100 eV at solid density affects the emission profile. As mentioned previously, the He-resonance line is optically thick at these temperatures and using more, but thinner zones, the spectra is very different and gives erroneously the optically thin result. When the total thickness of 0.4 μm is modeled with 20 zones, for example, the self-pumping of the resonance lines in each zone is lower because the zone length is 20 times smaller. The photon escaping each zone is not absorbed in the adjacent zones since there is no account of zone coupling. In one zone case, however, the self-pumping is computed with the entire thickness of 0.4 μm and hence the emission is higher as shown in the Fig 5.12. Again, depending on the thickness of the zones chosen to represent the plasma while considering the interplay of line ratios, this causes a problem in unique determination of plasma conditions. This result strongly suggests that the zone coupling scheme is required to correctly predict the K-shell spectra from short-pulse laser experiments.

5.4.4 Effect of plasma temporal evolution

Modeling of K-shell spectra up to now has taken the assumption that ionization state, temperature, density, and hot electron population are all constant in time. However, it is known that as the plasma expands and cools, the emission originates from a range of temperatures and densities. To investigate how emission is affected by cooling, hydrodynamic simulations are performed by giving the layered target an initial temperature and density and letting it evolve in time.

A simulation of the layered target was carried out using the 1-D hydrodynamics code HYADES [119]. Multi-group diffusion was used with 50 radiation groups from 10 eV - 50 keV, opacities were generated from an in-line average atomic physics model which assumes LTE. Temperature, density, and length information of the copper layer every 500 fs were then used in a FLYCHK simulation. Average ionization was recalculated in FLYCHK and spectra were calculated independently for every time step and integrated in time.

An initial temperature of 2300 eV and solid density in all layers produced spectra that comes closest to the measured data, but does not fit as well as the steady state case. The temperature and density information from the HYADES simulation is shown in Fig 5.13 and spectral calculation from several points in time are shown in Fig 5.14a. The temperature drops very quickly such that emission becomes predominantly Li-like and contribution to the integrated spectra lasts for about 15 ps. Fig 5.14b shows the difference in He-like line ratios of time-integrated calculations compared with steady state spectra. Initial temperature of 2300 eV is 200 eV higher than what was predicted by the steady state simulation of 2100 eV.

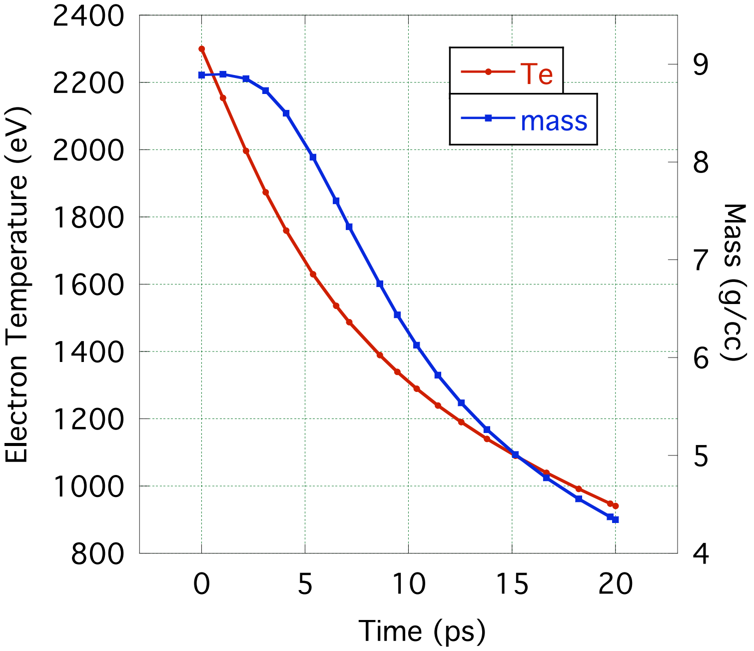

Figure 5.13: Temperature and density of the copper layer. Initial temperature of the entire target was 2300 eV and solid density, and let to decay over a period of 20 ps in the hydrodynamics code HYADES.

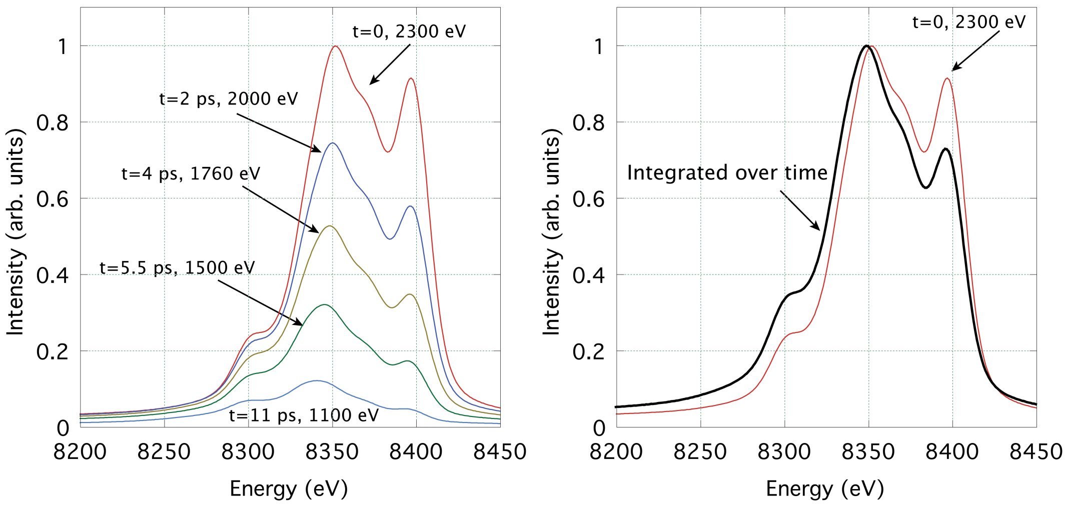

(a)

(b)

Figure 5.14: (a) shows resulting spectra from a cooling plasma with initial temperature of 2300 eV and solid density. Spectra is then integrated in time and compared to the t = 0 case in **(b)**.

Next, hot electrons were factored into the simulation with an initial temperature at solid density of 1300 eV of the target. The temperature and density information from the HYADES simulation is shown in Fig 5.15. A constant hot electron population of 1% and temperature of 1 MeV was used for the each time step of the simulation. Spectra from several time steps over 4 ps are shown in Fig 5.16a and again normalized to the $t = 0$ case. As the plasma starts to expand, temperature and density begins to drop and the spectra show more lines from lower ionization states. In the integrated spectra shown in Fig 5.16b a slight broadening effect due to lines from lower ionization states which is produced in the presence of hot electrons. This implies that a temporally evolving plasma could be a likely scenario for the observation of K-alpha lines from numerous ionization states evident in the data set.

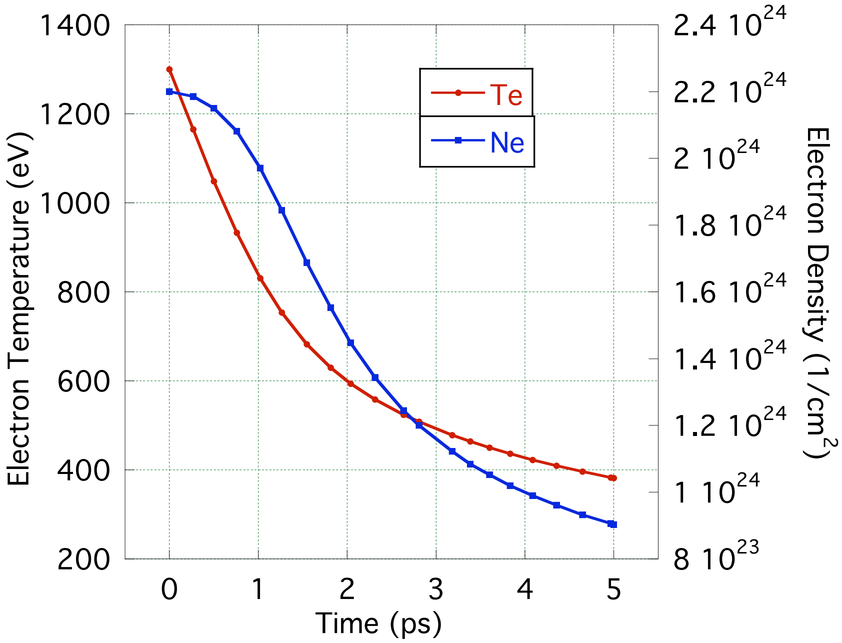

Figure 5.15: Temperature and density of the copper layer. Initial temperature of the entire target was 1300 eV and solid density, and let to decay over a period of 5 ps in the hydrodynamics code HYADES.

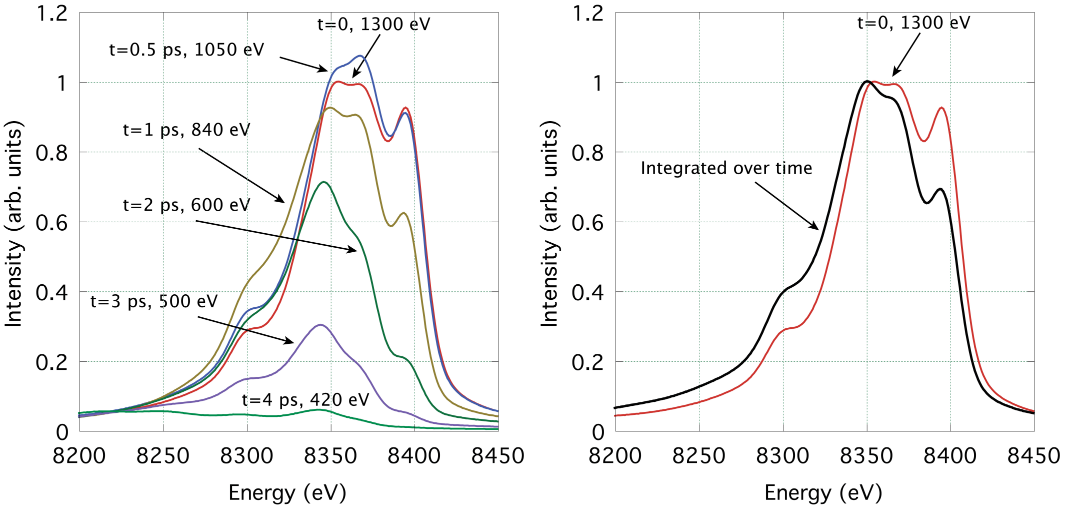

(a)

(b)

Figure 5.16: The initial temperature of the plasma is set at 1300 eV with solid density, only with this iteration, 1% hot electrons was factored into the spectral calculation. The resulting spectra are shown in **(a)** and spectra integrated in time is shown in **(b)**.

5.5 Summary

Copper K-shell emission spectra emitted from various depths in a solid target irradiated by a short pulse laser have been studied. There are two trends that can easily be identified from the measured spectra of the copper layer. At the front of the target, cold K-alpha is very intense compared to emission from higher ionization states. This starts to shift as the flour layer is moved deeper into the target. With the fluorescence layerfluorescence layer at 0.75 μm into the target, He-alpha dominates the spectra. Furthermore, at even deeper positions, the cold K-alpha line becomes constant and there is a steady drop in He-alpha line.

The atomic model FLYCHK has been used to study He-alpha spectra affected by various common assumptions when modeling short pulse laser produced plasmas. First, the He-alpha data is fitted to spectra from copper plasma with a set of thermal electron temperature and density. It has been found that the thermal temperature at the surface of the target had to be approximately 2.1 keV at solid density. It has been clearly demonstrated that three modeling parameters, hot electron fraction, plasma size, and temporal evolution, need to be considered as free parameters in the modeling of He-like lines. Adding a second electron distribution, depending on the exact fraction can lead to the lower temperature plasma and emission spectra that would otherwise be from a high temperature plasma without hot electrons. Without factoring in hot electrons we could be overestimating the thermal temperature by a factor of 2. The effect of plasma size on self absorption is another parameter that can affect the spectra, but its overall effect can be reduced by experimental means. When factoring in time dependence a higher initial plasma temperature is required such that the time integrated spectrum provides a best fit to the data. However, one notes that there are still temporal events such as the temporal profile of the laser pulse and hence of the electron source, and relaxation of the hot electron distribution, which will further influence the time-dependent emission profiles. We also demonstrated that a spectral calculation without a proper treatment of radiative transport, especially for self-absorption can give a misleading result for optically thick lines. Caution is warranted when one extends a single-zone code into multi-zone problem and uses a ray tracing technique to composite spectra.

4.8 Acknowledgement

Portions of Chapter 5, is a reprint of the material that has been submitted for publication: S. N. Chen, P. K. Patel, H. -K. Chung, A. J. Kemp, S. Le Pape, B. R. Maddox, S. C. Wilks, R. B. Stephens, F. N. Beg, "X-ray Spectroscopy of Buried Layer Foils Irradiated at 10^{20} W/cm^{2}", (Physics of Plasmas 2009, accepted). The dissertation author was the primary investigator and author of this paper.

Chapter 6

Conclusion and Future Work

Short pulse laser matter interactions are of great interest in the field of high energy density physics. Laboratory generation of hot dense matter at keV temperatures near solid density is necessary for the understanding of radiation and particle transport processes and benchmarking of computer models in astrophysics, inertial confinement fusion (ICF), and fast ignition (FI) research. The created plasma from a short pulse laser solid interaction exists for only several tens of picoseconds with nonuniform temperature and density. Furthermore, to fully understand the complex interaction between the laser, the solid, and what is measured, multiple computer models are relied upon to describe the event.

Two experiments have been conducted specifically designed to study temperature of a solid irradiated by a short pulse laser with intensities greater than 10^{19} W/cm^2. In the first experiment, K-shell spectra from an irradiated target was analyzed to extract temperature and density of the created plasma. With spectroscopic modeling of measured data using the collisional radiative code SCRAM, it was found that there exists a large temperature gradient in the interior of the resulting plasma. The front surface of the solid target achieved temperatures greater than 1 keV at near solid densities while the rest of the target reached temperatures of 100 eV. The data also suggested that bulk and peak temperature are highly dependent on the transverse size and tamping material. However, it can be concluded the observed shifting of the K-alpha line, up to a B-like ion, is a reliable and robust diagnostic of the bulk temperature of the target when hot electron fraction is less than 10% for copper targets. Additionally, K-alpha imaging showed non-uniform spread of hot electrons in a cold target, regardless of target size, in the lateral direction. With gradients in all directions, exact density and temperature of the plasma is difficult to estimate due to the limitations of the diagnostics. Furthermore, additional complexity arises from assumptions must be made in the analysis of the He-like lines since they can be produced both thermally and induced by hot electrons. These limitations prompted further investigation which motivates a second experiment.

In the second experiment, targets dimensions were reduced to minimize lateral gradients and possible opacity issues. K-shell spectra was again recorded and the analysis was performed using the collisional radiative code FLYCHK. The focus of the analysis was on the He-like lines since it is optically thick and which is often used in determining peak temperature. First, it was found using a collisional radiative code code that, a hot electron population must be included in the spectral calculation. The uncertainty in the hot electrons population can results in a peak temperature error of a factor of two. Second, the 1-D hydrodynamics code HYADES and FLYCHK was integrated to study the effects of temporal evolution of a cooling plasma on K-shell emission with two electron temperatures. It was assumed that the plasma was instantaneously heated to a peak temperature, spectral emission is integrated from then on, and no further heating is added. It was then shown that considering time dependence will raise estimates of peak temperature because of the integration of emission from colder plasma in late time. Third, the sensitivity of He-like lines on optical depth was studied. The spectral calculation of optically thick lines includes an approximation for self absorption and therefore rendering the size of the plasma an important parameter. Also in this study, it was shown that the effect of an incorrect escape factor approximation when a plasma is represent with multiple zones since the zone size is arbitrarily set.

6.1 Possible future experiments and modeling

Two possible paths can be taken, although not mutually exclusive, on how to proceed further: either experimental methods are improved to create single temperature density plasmas for ease in comparison to models or find self consistent ways to model a multiple temperature and density plasma evolving in time.

To discuss the first route, there are a number of laser and target designs to constrain external factors to achieve a single temperature and density plasma. First, the contrast ratio of the short pulse can be increased so target deformation due to the pre-pulse can be minimized. Also, the laser pulse length can be shortened to reduced heating time, thus reducing temporal uncertainty, and the beam can be defocused to increase the uniformity of the illumination on the target. Lateral dimensions of the target can be reduced only to be limited by the pointing accuracy of the laser.

Additionally, the buried layer can be thinned to reduce opacity effects. However, this depends on the signal to noise ratio of the diagnostics. The fluorescence layer layer should be a higher Z material such that the K-shell lines of interest is only produced from the interaction with hot electrons.

The ability to resolve the resonance lines and satellite lines of K-alpha lines which would significantly constrain parameters in the modeling. This can be achieved through the use of either a different type of crystal spectrometer or a thinned HOPG crystal. This again limited to the achieved signal to noise ratio.

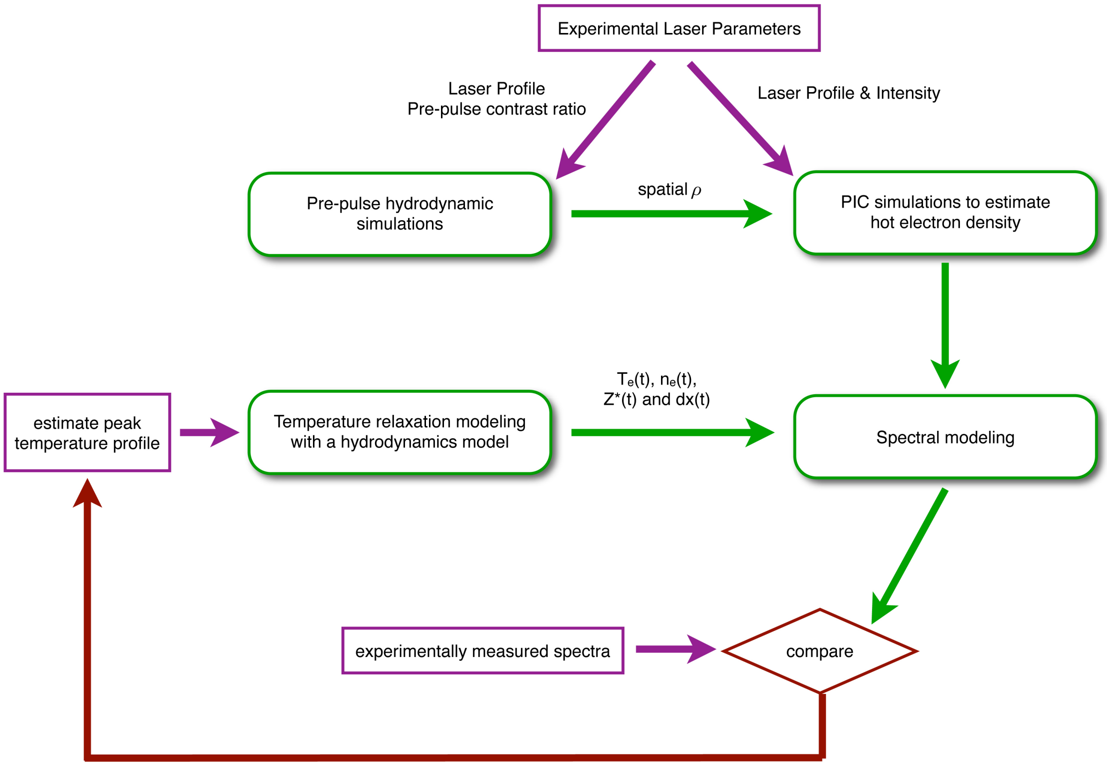

Figure 6.1: Modeling procedure integrating hydrodynamic, PIC, and atomic codes to reproduce experimental data.

Of the later route, the flowchart in Fig 6.1 outlines a possible modeling strategy that integrates three types of codes to model the short pulse laser produced plasma. Experimental laser parameters such as spatial profile and pre-pulse information can be used in a hydrodynamics code to estimate target conditions prior to the main pulse. That information can then be used in a Particle in Cell (PIC) model, along with laser intensity, to model laser absorption into hot electrons and estimate hot electron population inside the target as a function of time . The code would provide information about hot electron creation, escape, energy lose in the target, and recirculation. With detailed hot electron characteristics, spectral modeling in time, coupled with a hydrodynamics code, can be performed much like the modeling system used in Chapter 6. It should be noted that there are still other factors such as electron transport, the effect of fields on hot electrons, etc., should also eventually be included in the model.

The problem of possible opacity errors, as pointed out in Chapter 6, when modeling optically thick lines with the use of multi-zone representations, must be resolved. One possible solution to calculate self absorption over multiple cells is the use of techniques described by MacFarland *et. al.* [128]. Other spectral analysis techniques, such as χ^2 tests, can be used to approximate the range of plasma temperatures .

Finally other diagnostics can be employed to give an indication as to whether our treatment of the laser plasma interaction is accurate. Streak cameras can be used to time resolve K-shell spectra will greatly enhance time dependent modeling of spectra. Absolute yield of K-shell photons can be measured using a calibrated Single - Hit CCD camera system. The use of other parts of K-shell spectra such as K-beta, He-beta, He-gamma, etc., can be used as density diagnostic and temperature verification. Nonetheless, any further investigations will inevitably reveal what further information, either acquired experimentally, code based, or analytically is needed. Then coupled with other plasma diagnostics that measure radiation or particles emitted, a better picture of short pulse laser produced plasmas can be assembled.

REFERENCES

[1] F. N. Beg, M. S. Wei, E. L. Clark, A. E. Dangor, R. G. Evans, P. Gibbon, A. Gopal, K. L. Lancaster, K. W. D. Ledingham, P. McKenna, P. A. Norreys, M. Tatarakis, M. Zepf and K. Krushelnick, Physics of Plasmas **11**, 2806 (2004).

[2] H. S. Park, D. M. Chambers, H. K. Chung, R. J. Clarke, R. Eagleton, E. Giraldez, T. Goldsack, R. Heathcote, N. Izumi, M. H. Key, J. A. King, J. A. Koch, O. L. Landen, A. Nikroo, P. K. Patel, D. F. Price, B. A. Remington, H. F. Robey, R. A. Snavely, D. A. Steinman, R. B. Stephens, C. Stoeckl, M. Storm, M. Tabak, W. Theobald, R. P. J. Town, J. E. Wickersham and B. B. Zhang, Physics of Plasmas **13** (5) (2006).

[3] M. Zepf, E. L. Clark, F. N. Beg, R. J. Clarke, A. E. Dangor, A. Gopal, K. Krushelnick, P. A. Norreys, M. Tatarakis, U.Wagner, and M. S.Wei, Physical Review Letters **90** (6), 064801 (2003).

[4] E. L. Clark, K. Krushelnick, J. R. Davies, M. Zepf, M. Tatarakis, F. N. Beg, A. Machacek, P. A. Norreys, M. I. K. Santala, I. Watts and A. E. Dangor, Physical Review Letters **84** (4), 670-673 (2000).

[5] R. A. Snavely, M. H. Key, S. P. Hatchett, T. E. Cowan, M. Roth, T. W. Phillips, M. A. Stoyer, E. A. Henry, T. C. Sangster, M. S. Singh, S. C. Wilks, A. MacKinnon, A. Offenberger, D. M. Pennington, K. Yasuike, A. B. Langdon, B. F. Lasinski, J. Johnson, M. D. Perry and E. M. Campbell, Physical Review Letters **85** (14), 2945-2948 (2000).

[6] A. A. Andreev and J. Limpouch, Journal of Plasma Physics **62**, 179-193 (1999).

[7] U. Wagner, M. Tatarakis, A. Gopal, F. N. Beg, E. L. Clark, A. E. Dangor, R. G. Evans, M. G. Haines, S. P. D. Mangles, P. A. Norreys, M. S. Wei, M. Zepf and K. Krushelnick, Physical Review E **70** (2), 235201 (2004).

[8] M. Tatarakis, A. Gopal, I. Watts, F. N. Beg, A. E. Dangor, K. Krushelnick, U. Wagner, P. A. Norreys, E. L. Clark, M. Zepf, and R. G. Evans, Physics of Plasmas **9**, 2244 (2002).

[9] K. L. Lancaster, S. Karsch, H. Habara, F. N. Beg, E. L. Clark, R. Freeman, M. H. Key, J. A. King, R. Kodama, K. Krushelnick, K. W. D. Ledingham, P. McKenna, C. D. Murphy, P. A. Norreys, R. Stephens, C. Stoeckl, Y. Toyama, M. S. Wei and M. Zepf, Physics of Plasmas **11** (7), 3404-3408 (2004).

[10] P. McKenna, K. W. D. Ledingham, T. McCanny, R. P. Singhal, I. Spencer, M. I. K. Santala, F. N. Beg, K. Krushelnick, M. Tatarakis, M. S. Wei, E. L. Clark, R. J. Clarke, K. L. Lancaster, P. A. Norreys, K. Spohr, R. Chapman and M. Zepf, Physical Review Letters **91** (7) (2003).

[11] M. H. R. Hutchinson, Spectrochimica Acta Part B: Atomic Spectroscopy **58**, 115 (2003)

[12] M. Borghesi, P. Audebert, S. V. Bulanov, T. Cowan, J. Fuchs, J. C. Gauthier, A. J. MacKinnon, P. K. Patel, G. Pretzler, L. Romagnani, A. Schiavi, T. Toncian and O. Willi, Laser and Particle Beams **23**, 291-295 (2005).

[13] Frontiers in High Energy Density Physics The X-Games of Contemporary Science, Committee on High Energy Density Physics, National Academies Press, National Academy of Science Washington DC (2003).

[14] M. H. Key, Physics of Plasmas **14**, 055502 (2007).

[15] J. D. Lindl, Inertial Confinement Fusion (Springer-Verlag, New York, 1998).

[16] J. D. Lawson, Proceedings of the Physical Society **B70** , 6 (1957).

[17] E. R. Harrison, Physical Review Letters **11** (12), 535-& (1963).

[18] C. Maisonnier, Nuovo Cimento **42**, 332-40 (1966).

[19] M. Tabak, J. Hammer, M. E. Glinsky, W. L. Kruer, S. C. Wilks, J. Woodworth, E. M. Campbell, M. D. Perry and R. J. Mason, Physics of Plasmas **1** (5), 1626-1634 (1994).

[20] S. Hatchett, M. Tabak, R. Turner, and R. Stephens, presentation given at Anomalous Absorption Conference, Ocean City, MD (May 2000).

[21] G. Malka and J. L. Miquel, Physical Review Letters **77** (1), 75-78 (1996).

[22] C. K. Li and R. D. Petrasso, Physical Review E **70**, 067401 2004

[23] S. Atzeni, A. Schiavi, C. Bellei, Physics of Plasmas **14**, 052702 (2007)

[24] R. Kodama, P. A. Norreys, K. Mima, A. E. Dangor, R. G. Evans, H. Fujita, Y. Kitagawa, K. Krushelnick, T. Miyakoshi, N. Miyanaga, T. Norimatsu, S. J. Rose, T. Shozaki, K. Shigemori, A. Sunahara, M. Tampo, K. A. Tanaka, Y. Toyama, Y. Yamanaka and M. Zepf, Nature **412** (6849), 798 (2001).

[25] M. Roth, T. E. Cowan, M. H. Key et al., Physical Review Letters **86**, 436 (2001).

[26] A. Mackinnon, presented at 9th International Fast Ignition Workshop, Cambridge, MA, November 2006 http://fsc.lle.rochester.edu.

[27] P. K. Patel, A. J. MacKinnon, M. H. Key et al., Physical Review Letters **91**, 125004 (2003).

[28] S. C. Wilks and W. L. Kruer, IEEE Journal of Quantum Electronics **33** (11), 1954 (1997).

[29] H. Chen, P. K. Patel, D. F. Price, B. K. Young, P. T. Springer, R. Berry, R. Booth, C. Bruns, and D. Nelson, Review of Scientific Instruments **74**, 1551 (2003).

[30] B. A. Remington, R. P. Drake, D. D. Ryutov, Review of Modern Physics **78**, 755 (2006).

[31] S. J. Moon, S. C. Wilks, R. I. Klein, B. A. Remington, D. D. Ryutov, A. J. McKinnon, P. K. Patel, and A. Spikovsky, Astrophysical and Space Science **298**, 293 (2005).

[32] R. R. Freeman, D. Batani, S. Baton, M. Key and R. Stephens, Fusion Science & Technology **49**, 297 (2006).

[33] G. Gregori, S. B. Hansen, R. Clarke, R. Heathcote, M. H. Key, J. King, R. I. Klein, N. Izumi, A. J. Mackinnon, S. J. Moon, H. S. Park, J. Pasley, N. Patel, P. K. Patel, B. A. Remington, D. D. Ryutov, R. Shepherd, R. A. Snavely, S. C. Wilks, B. B. Zhang, S. H. Glenzer, Contributions to Plasma Physics **45** (3-4), 284 (2005).

[34] A. Saemann, K. Eidmann, I. E. Golovkin, R. C. Mancini, E Andersson, E. Forster, K. Witte, Physical Review Letters **82**, 4843 (1999).

[35] C. Y. Chien, J. S. Coe, G. Mourou, J. C. Kieffer, M. Chaker, Y. Beaudoin, O Peyrusse, D. Gilles, Optics Letters **18**, 1535 (1993).

[36] Z. Jiang, J. C. Kieffer, J. P. Matte, M. Chaker, O Peyrusse, D. Gilles, G. Korn, A Maksimchuk, S. Coe, G. Mourou, Physics of Plasmas **2**, 1702 (1995).

[37] K. B. Wharton, S. P. Hatchett, S. C. Wilks, M. H. Key, J. D. Moody, V. Yanovsky, A. A. Offenberger, B. A. Hammel, M. D. Perry, C. Joshi, Physical Review Letters **81**, 822 (1998).

[38] E. Martinolli, D. Batani, E. Perelli-Cippo, F. Scianitti, M. Koeing, J. J. Santos, F. Amiranoff, S. D. Baton, T. Hall, M. Key, A. Mackinnon, R. Snavely, R. Freeman, C. Andersen, J. King, R. Stephens, M. R. Le Gloahec, C. Rousseaux, T. E. Cowan, Laser and Particle Beams **20** (2), 171-175 (2002).

[39] K. Eidmann, U, Andiel, F. Pisani, P. Hakel, R. C. Mancini, G. C. Junkel-Vives, J Abdallah, K Witte, Journal of Quantitative Spectroscopy and Radiative Transfer **81**, 133 (2003)

[40] H. Nishimura, T. Kawamura, R. Matsui, Y. Ochi, S. Okihara, S. Sakabe, F. Koike, T. Johzaki, H. Nagatomo, K. Mima, I. Uschmann and E. Forster, Journal of Quantitative Spectroscopy and Radiative Transfer **81**, 327 (2003).

[41] J. A. Koch, Y. Aglitskiy, C. Brown, R. Freeman, S. Hatchett, G. Holland, M. Key, A. MacKinnon, J. Seely, R. Snavely, and R. Stephens, Review of Scientific Instruments **74**, 2130 (2003).

[42] W. Theobald, K. Akli, R. Clarke, J. A. Delettrez, R. R. Freeman, S. Glenzer, J. Green, G. Gregori, R. Heathcote, N. Izumi, J. A. King, J. A. Koch, J. Kuba, K. Lancaster, A. J. MacKinnon, M. Key, C. Mileham, J. Myatt, D. Neely, P. A. Norreys, H. S. Park, J. Pasley, P. Patel, S. P. Regan, H. Sawada, R. Shepherd, R. Snavely, R. B. Stephens, C. Stoeckl, M. Storm, B. Zhang and T. C. Sangster, Physics of Plasmas **13** (4), 11 (2006).

[43] S. N. Chen, G. Gregori, P. K. Patel, H. K. Chung, R. G. Evans, R. R. Freeman, E. G. Saiz, S. H. Glenzer, S. B. Hansen, F. Y. Khattak, J. A. King, A. J. Mackinnon, M. M. Notley, J. R. Pasley, D. Riley, R. B. Stephens, R. L. Weber, S. C. Wilks and F. N. Beg, Physics of Plasmas **14** (10), 6 (2007).

[44] K. U. Akli, S. B. Hansen, A. J. Kemp, R. R. Freeman, F. N. Beg, D. C. Clark, S. D. Chen, D. Hey, S. P. Hatchett, K. Highbarger, E. Giraldez, J. S. Green, G. Gregori, K. L. Lancaster, T. Ma, A. J. MacKinnon, P. Norreys, N. Patel, J. Pasley, C. Shearer, R. B. Stephens, C. Stoeckl, M. Storm, W. Theobald, L. D. Van Woerkom, R. Weber and M. H. Key, Physical Review Letters **100** (16), 4 (2008).

[45] R. B. Stephens, R. A. Snavely, Y. Aglitskiy, F. Amiranoff, C. Andersen, D. Batani, S. D. Baton, T. Cowan, R. R. Freeman, T. Hall, S. P. Hatchett, J. M. Hill, M. H. Key, J. A. King, J. A. Koch, M. Koenig, A. J. MacKinnon, K. L. Lancaster, E. Martinolli, P. Norreys, E. Perelli-Cippo, M. Rabec Le Gloahec, C. Rousseaux, J. J. Santos, and F. Scianitti, Physical Review E **69**, 066414 (2004)

[46] J. Myatt, W. Theobald, J. A. Delettrez, C. Stoeckl, M. Storm, T. C. Sangster, A. V. Maximov, R. W. Short, Physics of Plasmas **14**, 056301 (2007).

[47] A. J. Mackinnon, Y. Sentoku, P. K. Patel, D. W. Price, S. Hatchett, M. H. Key, C. Andersen, R. Snavely, R. R. Freeman, Physical Review Letters **88**, 215006 (2002).

[48] H. Chen, S. C. Wilks, Laser and Particle Beams **23**, 411 (2005).

[49] A. Sengebusch, S. H. Glenzer, A. L. Kritcher, H. Reinholz and G. Ropke, Contributions to Plasma Physics **47** (4-5), 309 (2007).

[50] D.J. Hoarty, S.F. James, H. Davies, C.R.D. Brown, J.W.O. Harris, C.C. Smith, S.J. Davidson, E. Kerswill, B.J.B. Crowley and S.J. Rose, High Energy Density Physics **3**, 115 (2007).

[51] S. B. Hansen and A. S. Shlyaptseva, Physical Review E **70** (3) (2004).

[52] J. Abdallah Jr., A. Ya. Faenov, T. A. Pikuz, M. D. Wilke, G.A. Kyrala, R. E. H. Clark, Journal of Quantitative Spectroscopy and Radiative Transfer **62**, 1-11 (1999).

[53] J. Abdallah Jr., G. C. Junkel-Vives, A. Ya. Faenov, I. Yu. Skobelev, T. A. Pikuz, A. I. Magunov, F. Blasco, C. Bonte, F. Dorchies, T. Caillaud, C. Salin, C. Stenz, Journal of Quantitative Spectroscopy and Radiative Transfer **81** (2003).

[54] H. Chen, R. Shepherd, H. K. Chung, A. Kemp, S. B. Hansen, S. C. Wilks, Y. Ping, K. Widmann, K. B. Fournier, G. Dyer, A. Faenov, T. Pikuz and P. Beiersdorfer, Physical Review E **76** (5) (2007).

[55] M. S. Wei, A. Solodov, J. Pasley, R. B. Stephens, D. Welch and F. N. Beg, Physics of Plasmas **15**, 08310 (2008).

[56] P. Gibbon, E. Förster, Plasma Physics and Controlled Fusion **38**, 769-793 (1996).

[57] J. Meyer-ter-Vehn, A Pukhov, and Z. M. Sheng, Relativistic Laser Plasma Interactions, in: Atoms, Solids, and Plasmas in Super-Intense laser Fields (editors: D. Batani, C. J. Joachain, S. Martelucci, and A. N. Chester), Kluwer Academic/Plenum Publishers, New York (2001).

[58] A. B. Langdon, Physical Review Letters **44**, 575 (1980)

[59] W. L. Kruer, The Physics of Laser Plasma Interactions. Addison-Wesley, New York (1988).

[60] W. Rozmus and V. T. Tikhonchuk, Physical Review A **42** (12), 7401 (1990).

[61] G. J. Pert, Physical Review E **51**, 4778 - 4789 (1995).

[62] J. P. Friedberg, R. W. Mitchell, R. L. Morse and L. I. Rudsinski, Physics Letters **28**, 795 (1972).

[63] D. W. Forslund, J. M. Kindel, and K. Lee, Physical Review Letters **39**, 284 (1977).

[64] K. Estabrook and W. L. Kruer, Physical Review Letters **40**, 42 (1978).

[65] D. D. Meyerhofer, H. Chen, J. A. Delettrez, B. Soom, S. Uchida, and B. Yaakobi, Physics of Fluids B **5**, 2584 (1993).

[66] J. Zheng, K. A. Tanaka, T. Sato, T. Yabuuchi, T. Kurahashi, Y. Kitagawa, R. Kodama, T. Norimatsu, and T.Yamanaka, Physical Review Letters **92**, 165001 (2004).

[67] F. Brunel, Physical Review Letters, **59**, 52 (1987).

[68] S. Kato, B. Bhattacharyya, A. Nishiguchi and K. Mima, Physics of Fluids B-Plasma Physics **5** (2), 564-570 (1993).

[69] P. Gibbon, A. R. Bell, Physical Review Letters **68**, 1535 - 1538 (1992).

[70] Y. Ping, R. Shepherd, B. F. Lasinski, M. Tabak, H. Chen, H. K. Chung, K. B. Fournier, S. B. Hansen, A. Kemp, D. A. Liedahl, K. Widmann, S. C. Wilks, W. Rozmus, and M. Sherlock, Physical Review Letters **100**, 085004 (2008).

[71] J. Denavit, Physical Review Letters **69**, 3052 - 3055 (1992).

[72] S. C. Wilks, W. L. Kruer, M. Tabak and A. B. Langdon, Physical Review Letters **69** (9), 1383 (1992).

[73] F. N. Beg, A. R. Bell, A. E. Dangor, C. N. Danson, A. P. Fews, M. E. Glinsky, B. A. Hammel, P. Lee, P. A. Norreys, and M. Tatarakis, Physics of Plasmas **4**, 447 (1997).

[74] M. G. Haines, M. S. Wei, F. N. Beg, and R. B. Stephens, Physical Review Letters **102** (4), 045008 (2009).

[75] T. Holstein, Physical Review 72, 1212 (1947).

[76] T. Holstein, Physical Review 83, 1159 (1951).

[77] L. M. Biberman, Comp. Rend. Acad Sci. URSS **27**, 920 (1940), (in English)

[78] L. M. Biberman, ZH. Eksp. I Teor. Fiz **17**, 416 (1947), (English Trans. ORNL-Tr-681)

[79] G. J. Phillips, J. S. Wark, F. M. Kerr, S. J. Rose and R. W. Lee, High Energy Density Physics **4** (1-2), 18 (2008)

[80] W. Lotz, Z. Phys. **216**, 241 (1968).

[81] W. Lotz, Z. Phys. **220**, 266 (1969).

[82] C. Homberger, Journal of Physics B: Atomic, Molecular, and Optical Physics **31**, 3693 (1998),

[83] M. A. R. Patoary, M. Alfaz Udin, A. K. F. Haque, A. K. Basak, M. R. Taluder, K. R. Karim, B. C. Saha, International Journal of Quantum Chemistry **108** (6), 1023 (2008).

[84] L. L House, The Astrophysical Journal Supplement Series **18** (155), 21 1969

[85] D. Strickland, G. Mourou, Optical Communications **56**, 219-221 (1985).

[86] C. N. Danson, R. Allott, G. Booth, J. Collier, C. B. Edwards, P. S. Flintoff, S. J. Hawkes, M. H. R. Hutchinson, C. Hernandez-Gomez, J. Leach, D. Neely, P. Norreys, M. Notley, D. A. Pepler, I. N. Ross, J. A. Walczak, T. B. Winstone, Laser and Particle Beams **17**, 341 (1999).

[87] C. N. Danson, P. A. Brummitt, R. J. Clarke, I. Collier, B. Fell, A. J. Frackiewicz, S. Hawkes, C. Hernandez-Gomez, P. Holligan, M. H. R. Hutchinson, A. Kidd, W. J. Lester, I. O. Musgrave, D. Neely, D. R. Neville, P. A. Norreys, D. A. Pepler, C. Reason, W. Shaikh, T. B. Winstone, R. W. W. Wyatt, B. E. Wyborn, Laser And Particle Beams **23** (1), 87–93 (2005).

[88] B. C. Stuart, J. D. Bonlie, J. A. Britten, J. A. Caird, R. Cross, C. A. Ebbers, M. J. Eckart, A. C. Erlandson, W. A. Molander, A. Ng, P. K. Patel, D. F. Price, Technical report no. UCRL-CONF-221530, Lawrence Livermore National Laboratory (2006).

[89] I. N. Ross, P. Matousek, M. Towrie, A. J. Langley, J. L. Collier, C. N. Danson, C. Hernandez-Gomez, D. Neely and K. Osvay, Laser and Particle Beams 17 (2), 331-340 (1999).

[90] W. H. Zachariasen, Theory of X-ray Diffraction in Crystals, John Wiley and Sons, Inc., New York (1945)

[91] A. K. Freund, A. Munkholm, S. Brennan, Proceeding of SPIE **2856**, 68 (1996).

[92] H. Legall, H. Stiel, P. Nickles, A. A. Bjeoumikhov, N. Langhoff, M. Haschke, V. A. Arkadiev, R. Wedell, Proceedings SPIE **5918**, 591802 (2005).

[93] A. Pak, G. Gregori, J. Knight, K. Campbell, D. Price, B. Hammel, O. L. Landen, and S. H. Glenzer, Review of Scientific Instruments **75**, 3747 (2004).

[94] J.A. Koch, Y. Aglitskiy, C. Brown, T. Cowan, R. Freeman, S. Hatchett, G. Holland, M. Key, A. MacKinnon, J. Seely, R. Snavely and R. Rtephens, Review of Scientific Instruments **74**, 2130 (2003).

[95] J. A. King, K. Akli, R. A. Snavely, B. Zhang, M. H. Key, C. D. Chen, M. Chen, S. P. Hatchett, J. A. Koch, A. J. MacKinnon, P. K. Patel, T. Phillips, R. P. J. Town, R. R. Freeman, M. Borghesi, L. Romagnani, M. Zepf, T. Cowan, R. Stephens, K. L. Lancaster, C. D. Murphy, P. Norreys, and C. Stoeckl, Review of Scientific Instruments **76**, 076102 (2005).

[96] J. A. Koch, O. L. Landen, T. W. Barbee, Jr., P. Celliers, L. B. DaSilva, S. G. Glendenning, B. A. Hammel, D. H. Kalantar, C. Brown, J. Seely, G. R. Bennett, W. Hsing, Applied Optics **37**, 1784 (1998).

[97] Image Plates as Detectors for X-Ray diffraction by Shigeru Munekawa and Joseph D. Ferrara

[98] S. G. Gales, C. D. Bentley, Review of Scientific Instruments **75** (10), 4001-4003 (2004).

[99] M.H. Key, W. T. Toner, T. J. Goldsack, J. D. Kilkenny, S. A. Veats, P. F. Cunningham, C. L. S. Lewis, Physics of Fluids **26**, 7 (1983).

[100] h2d is a commercial product of Cascade Applied Sciences Incorporated, 6325 Trevarton Drive, Longmont, CO 80503 (Electronic mail: larsen@casinc.com).

[101] See National Technical Information Service Document No. DE94011699, "SESAME database" by J. D. Johnson, Los Alamos National Laboratory report # LA-UR-94-1451, 1994. Copies may be ordered from the National Technical Information Service, Springfield VA 22161.

[102] F. N. Beg, M. S. Wei, E. L. Clark, A. E. Dangor, R. G. Evans, P. Gibbon, A. Gopal, K. L. Lancaster, K. W. D. Ledingham, P. McKenna, P. A. Norreys, M. Tatarakis, M. Zepf, K. Krushelnick, Physics of Plasmas **5**, 2806 (2004).

[103] S. B. Hansen, PhD thesis University of Nevada, Reno (2003).

[104] S. B. Hansen, J. Bauche, C. Bauche-Arnoult, and M. F. Gu, High Energy Density Physics **3**, 109 (2007).

[105] M. F. Gu, Astrophysics Journal **590**, 1131 (2003).

[106] A. G. MacPhee, K. U. Akli, F. N. Beg, C. D. Chen, H. Chen, R. Clarke, D. S. Hey, R. R. Freeman, A. J. Kemp, M. H. Key, J. A. King, S. Le Pape, A. Link, T. Y. Ma, H. Nakamura, D. T. Offermann, V. M. Ovchinnikov, P. K. Patel, T. W. Phillips, R. B. Stephens, R. Town, Y. Y. Tsui, M. S. Wei, L. D. Van Woerkom, and A. J. Mackinnon, Review of Scientific Instruments **79**, 10F302-1-5 (2008).

[107] S. H. Glenzer, K. B. Fournier, C. Decker, B. A. Hammel, R. W. Lee, L. Lours,

B. J. MacGowan and A. L. Osterheld, Physical Review E **62** (2), 2728-2738 (2000).

[108] J. Fuchs, T. E. Cowan, P. Audebert, H. Ruhl, L. Gremillet, A. Kemp, M. Allen, A. Blazevic, J.-C. Gauthier, M. Geissel, M. Hegelich, S. Karsch, P. Parks, M. Roth, Y. Sentoku, R. Stephens, and E. M. Campbell, Physical Review Letters **91**, 255002-1-4 (2003).

[109] S. I. Krasheninnikov, A. V. Kim, B. K. Frolov and R. Stephens, Physics of Plasmas **12**, 073105 (2005).

[110] E. S. Weibel, Physical Review Letters **2**, 83 (1959).

[111] M. Honda, J. Meyer-ter-Vehn, A. Pukov, Physics of Plasmas **7**, 1302 (2000).

[112] J. R. Davies, A. R. Bell, M. G. Haines, S. M. Guerin, Physical Review E **56**, 7193 (1997).

[113] L. O. Silva, R. A. Fonseca, J. W. Tonge, W. B. Mori, J. M. Dawson, Physics of Plasmas **9**, 2458 (2002).

[114] R. G. Evans, High Energy Density Physics **2**, 35 (2006).

[115] HYADES is a commercial product of Cascade Applied Sciences Incorporated, 6325 Trevarton Drive, Longmont, CO 80503 (Electronic mail: larsen@casinc.com)

[116] H. -K Chung, M. H. Chen, W. L. Morgan, Y. Ralchenko, R. W. Lee, High Energy Density Physics **1**, 3 (2005).

[117] R. W. Lee, J. T. Larsen, Journal of Quantitative Spectroscopy and Radiative Transfer **56**, 535 (1996).

[118] A. Barshalom, Physical Review A **40**, 3183 (1989).

[119] R.L. Kelly, J. Phys. Chem. Ref. Data Suppl. **16,** 1 (1987).

[120] J.H. Scofield, Technical report no. UCID-16848, Lawrence Livermore National Laboratory (1975).

[121] H. Van Regemorter, Ap J **136** (1962) 906.

[122] A. Burgess, M. C. Chidichimo, Mon. Not. R. Astron. Soc. **203**, 1268 (1983).

[123] H. Kramers, Philos. Mag. **46** (1923) 836.

[124] J. H. Scofield, Physical Review A **40** (1989) 3054.

[125] E. B. Saloman, J. H. Hubbell, J. H. Scofield, At. Data. Nucl. Data Tables **38**, 1 (1988).

[126] M. Chen, E. Laiman, B. Crasemann, M. Aoyagi, H. Mark, Physical Review **19**, 2253 (1979).

[127] S. Perkins, D. Cullen, M. Chen, J. Hubbel, J. Rathkopf, J.H. Scofield, Technical report no. UCRL-50400 V.30, Lawrence Livermore National Laboratory (1991).

[128] J. J. MacFarlane, UWFDM-937, Univ. of Wisconsin Fusion Technology Institute Report (1993).